

CSDL-T-1250

**A VEHICLE HEALTH MONITORING SYSTEM
FOR THE SPACE SHUTTLE REACTION
CONTROL SYSTEM DURING REENTRY**

by

Anthony David Rosello

May 1995

**Master of Science Thesis
Massachusetts Institute of Technology**

(NASA-CR-188370) A VEHICLE HEALTH
MONITORING SYSTEM FOR THE SPACE
SHUTTLE REACTION CONTROL SYSTEM
DURING REENTRY M.S. Thesis -
Massachusetts Inst. of Technology
(Draper (Charles Stark) Lab.)
120 p

N95-29447

Unclass

63/16 0051500



The Charles Stark Draper Laboratory, Inc.
555 Technology Square, Cambridge, Massachusetts 02139-3563

~ ~

**A Vehicle Health Monitoring System
for the Space Shuttle Reaction Control System
During Reentry**

by

Anthony David Rosello

B.S., Engineering Science,
United States Air Force Academy
(1993)

SUBMITTED TO THE DEPARTMENT OF AERONAUTICS AND
ASTRONAUTICS IN PARTIAL FULFILLMENT OF THE
REQUIREMENTS FOR THE DEGREE OF

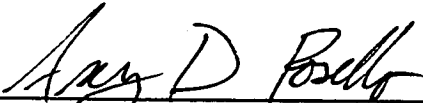
MASTER OF SCIENCE

at the

MASSACHUSETTS INSTITUTE OF TECHNOLOGY
May, 1995

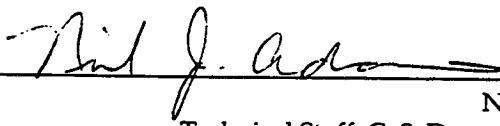
© Anthony David Rosello, 1995 All rights reserved.

Signature of Author



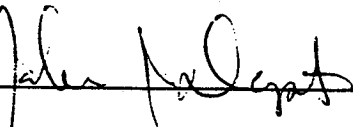
Department of Aeronautics and Astronautics
May, 1995

Certified by



Neil J. Adams
Technical Staff, C. S. Draper Laboratory
Technical Supervisor

Certified by



John J. Deyst
Professor of Aeronautics and Astronautics
Thesis Supervisor

Accepted by

Professor Harold Y. Wachman
Chairman Departmental Graduate Committee

101

A Vehicle Health Monitoring System for the
Space Shuttle Reaction Control System During Reentry

by

Anthony David Rosello

B.S., Engineering Science,
United States Air Force Academy
(1993)

Submitted to the Department of Aeronautics and
Astronautics on May 12, 1995 in partial fulfillment of the
requirements for the degree of Master of Science

Abstract

A general two tier framework for Vehicle Health Monitoring of Guidance Navigation and Control (GN&C) system actuators, effectors, and propulsion devices is presented. In this context, a top level monitor that estimates jet thrust is designed for the Space Shuttle Reaction Control System (RCS) during the reentry phase of flight. Issues of importance for the use of estimation technologies in Vehicle Health Monitoring are investigated and quantified for the Shuttle RCS demonstration application. These issues include rate of convergence, robustness to unmodeled dynamics, sensor quality, sensor data rates, and information recording objectives. Closed loop simulations indicate that a Kalman filter design is sensitive to modeling error and robust estimators may reduce this sensitivity. Jet plume interaction with the aerodynamic flowfield is shown to be a significant effect adversely impacting the ability to accurately estimate thrust.

Thesis Supervisor:
John J. Deyst

Technical Supervisor:
Neil J. Adams

PRECEDING PAGE BLANK NOT FILMED

Acknowledgments

There are several people that have helped me get where I am now. In this space I want to express my most sincere thanks to:

The Charles Stark Draper Laboratory for making my graduate education possible,

everyone in E41 who was always willing to take the time to answer any one of my several questions. I would especially like to thank Brent Appleby for his patient explanations of estimation theory and Dave Hanson for his careful proofreading of my thesis,

Prof. Deyst for being my advisor at MIT and his insightful review of my thesis,

Neil Adams for having me as a student, the meticulous reading of my thesis and teaching me more than just engineering, he is a great supervisor and mentor,

everyone at 13 Bigelow especially Scott Wallace, Kent Engebretson and Jason Schott for all of the enlightening discussions, dinners, and debates, they all have been a great part of my MIT experience,

and, my parents for their ceaseless support of all my endeavors.

Finally, I want to express the most sincere gratitude to my wife, Stacy, for all of her love, patience, and understanding.

This thesis was prepared at the Charles Stark Draper Laboratory, Inc., under NASA contract NAS9-18426.

Publication of this thesis does not constitute approval by Draper or the sponsoring agency of the findings or conclusions contained herein. It is published for the exchange and stimulation of ideas.

I hereby assign copyright of this thesis to the Charles Stark Draper Laboratory, Inc., Cambridge, Massachusetts.



Permission is hereby granted by the Charles Stark Draper Laboratory, Inc., to the Massachusetts Institute of Technology to reproduce any or all of this thesis.

Table of Contents

1.0 Introduction.....	13
2.0 Space Shuttle Flight Control Effectors.....	19
2.1 Space Shuttle RCS	19
2.1.1 Propellant Storage and Feed.....	20
2.1.2 Thruster Design and Layout.....	22
2.1.4 RCS RM System	23
2.1.3 RCS Sensor Data	25
2.1.5 Typical RCS Failures.....	27
2.2 Space Shuttle Aerosurfaces.....	28
2.2.1 Elevons.....	29
2.2.2 Rudder	30
2.2.3 Speedbrake	31
2.2.4 Bodyflap	32
3.0 Space Shuttle Reentry Vehicle Control and Dynamics	33
3.1 Reentry Overview	33
3.2 Entry Simulation Model	34
3.3 Entry Flight Control System	35
3.4 Space Shuttle Aerodynamic Reentry Model	38
3.4.1 Coordinate Frames.....	38
3.4.2 Equations of Motion	40
3.4.4 Simplified Aerodynamics Model.....	43
3.5 Aerosurface Actuator Models	47
3.6 RCS Effector Models	48
3.6.1 Plume Interaction	48
3.6.2 Impingement.....	50
3.6.3 Increased Atmospheric Pressure	52
3.6.4 Transient Effects	52
3.7 Sensor Models.....	53
3.8 Example Maneuvers	54

4.0 Kalman Filter Based VHM Estimator Theory and Design.....	57
4.1 Kalman Filter Development and Background	60
4.2 Model Formulation for Linear Estimation	64
4.2.1 Filter State Space Structure	64
4.2.2 Process Noise	67
4.2.3 Measurement Noise	69
4.3 Implementation of Kalman Filter for Thrust Estimation	70
5.0 Kalman Filter Analysis.....	73
5.1 Open Loop Analysis	73
5.1.1 Effect of Δt	73
5.1.2 Impact of Rate Sensor Precision.....	74
5.1.3 Effect of Firing Length.....	75
5.1.4 Same Pod Multiple Jet Firings.....	76
5.2 Closed Loop Simulation Analysis	79
5.2.1 Simulation Structure	79
5.2.2 Kalman Filter Nominal Performance Analysis.....	80
5.2.3 Kalman Filter and Modeling Error	83
5.2.3.1 Effect of Aerosurface Dynamics	83
5.2.3.2 Effect of Thrust Scaling	87
5.2.3.3 Aerodynamic Uncertainties.....	89
5.2.3.4 Plume Interaction Uncertainties	91
6.0 Robust Estimator Design	93
6.1 H_2 and H_∞ Optimal Estimators.....	93
6.1.1 Continuous Kalman Filter.....	93
6.1.2 Minimax Estimator	94
6.1.3 Structure for Robust Estimation.....	95
6.1.4 General Minimax Estimator Design	97
6.2 Problem Formulation and Estimator Design	102
6.2.1 Structure	102
6.3 Comparison of Performance.....	105
7.0 Conclusion	111
7.1 Summary of Results	112

7.2 Recommendations for Future Work.....	113
Appendix A: Relationship of Jet Thrust to Angular Acceleration	116
Appendix B: Reentry Model Parameters	118
Appendix C: Incorporating Parametric Uncertainty and Spectral Factorization	119
C.1 Incorporating Parametric Uncertainty into the Δ -block	119
C.2 Spectral Factorization	120
References	121

List of Figures

1.0-1: Overview of VHM Architecture for Shuttle RCS	14
2.1-1: Location of RCS Pods	19
2.1-2: Plumbing of Forward and Rear RCS Pods.....	21
2.1-3: Rear RCS Pod.....	23
2.1-4: RCS Sensor Locations	26
2.2-1: Location and Direction of Shuttle Aerosurface Deflections	29
2.2-2: Maximum Simultaneous Aileron and Elevator Deflection	31
2.2-3: Speedbrake and Rudder Deflection	31
2.2-4: Maximum Simultaneous Rudder and Speedbrake Deflection.....	32
3.1-1: Shuttle Reentry Profile and Thesis Models	34
3.2-1: Block Diagram of Reentry Simulation	34
3.3-1: Overview of Entry Flight Control	35
3.3-2: Block Diagram of Entry Flight Control System	36
3.3-3: Model of Roll Controller used in SIMULINK Simulation	36
3.3-4: Model of Pitch Controller used in SIMULINK Simulation	37
3.3-5: Model of Yaw Controller used in SIMULINK Simulation	37
3.4-1: Body Axis Frame.....	39
3.4-2: Rotation from Body to Stability Axis Frame	39
3.4-3: Stability Axis Frame	39
3.4-4: Block Diagram of Simplified Aerodynamic Model	46
3.5-1: Modeled Elevon Step Response Including High Frequency Noise.....	48
3.6-1: Angular Acceleration Comparison for Down Firing Jets	50
3.6-2: Angular Acceleration Comparison for Side Firing Jets	51
3.6-3: Angular Acceleration Comparison for Up Firing Jets	51
3.6-4: Altitude Scaling Factor	52
3.6-5: Primary Thruster Chamber Pressure, Typical 80 ms pulse	53
3.6-6: Time Response of Thrust Model to 80 ms Pulse	54
3.8-1: Response to 40° Bank Command	55
3.8-2: Response to 3° α Command	56
4.0-1: Overview of VHM System	57
4.0-2: Qualitative Relationships of Sensor Precision, Measurement Rate and Error.....	58
4.0-3: Relationship of Convergence Time and Mission Average Thrust Estimation Error	59

4.1-1: Kalman Filter Recursive Loop	64
4.2-2: Angular Acceleration due to Euler Coupling	68
4.3-1: Kalman Filter Loop for Thrust Estimation	72
5.1-1: Estimation Error for Different Time Steps, 80 ms Firing (IMU sensor)	74
5.1-2: Estimation Error for Different Sensors for a Minimum Impulse Firing	75
5.1-3: Steady State Thrust Estimation Error, Step Input to Side Firing Jet.....	76
5.1-4: Effect of Firing Length on Estimation Error.....	76
5.1-5: Estimation of Side (32) and Up (36) Jets Firing Simultaneously	78
5.1-6: Estimation of Two Side Firing Jets Using Two States	78
5.1-7: Estimation of Two Side Firing Jets Using One State.....	79
5.2-1: Block Diagram of Closed Loop Simulation.....	80
5.2-2: Kalman Filter Monitor Response For Nominal Bank Command	81
5.2-3: Response to a Degraded Jet Thrust	82
5.2-4: Effect of Aerosurface Dynamics	85
5.2-5: Effect of Aerosurface Dynamics w/ Delay Added	86
5.2-6: Timing Relationship of Aerosurface Deflection and Jet Firings	87
5.2-7: Effect of Thrust on Estimator Response	89
5.2-8: Effect of Incorrect Aerodynamic Model	91
5.2-9: Effect of 33% Error in Plume Interaction Term	92
6.1-1: General Transfer Function Representation	96
6.1-2: Closed Loop Block Diagram.....	96
6.1-3: General Transfer Function Representation	97
6.1-4: Modified Robust Performance Problem	100
6.2-1: Inputs and Outputs of Simple RCS Model.....	104
6.2-2: Weights for Robust Design.....	105
6.3-1: Singular Values of Nominal and Perturbed Models from Jet Force to Rates	107
6.3-2: Frequency Responses from δF to \hat{F}	108
6.3-3: Frequency Responses from δF to e	109
6.3-4: Time Responses of Estimation Error	110
A-1 : Geometric Relation of Vectors	117

List of Tables

2.1-1: Summary of Typical RCS Failures.....	28
2.2-1: Maximum Aerosurface Deflections and Rates	30
3.4-1: Summary of Reentry Models	46
4.2-1: Rate Sensors and Measurement Noise.....	70
5.2-1: Output from VHM for Nominal Simulation.....	81
5.2-2: Output from VHM for Degraded Thruster Firing	82
5.2-3: Output from VHM for Simulation w/ Aerosurface Dynamics	85
5.2-4: Output from VHM for Simulation w/ Delay Added.....	86
5.2-5: Output from VHM for Simulation w/ Thrust Model	89
5.2-6: Output from VHM for Simulation w/ Incorrect Aerodynamic Model	91
5.2-7: Output from VHM for Simulation w/ 33% Error in Jet Plume Interaction Term	92

1.0 Introduction

A primary objective for the development of future aerospace vehicles is the significant reduction of life cycle costs. To achieve this objective, more vehicle autonomy will be required with less emphasis on ground operations and maintenance. Vehicle Health Management is a key technology that will help aerospace systems meet these higher expectations, particularly in reduction of operations cost. Vehicle Health Management systems, which include Vehicle Health Monitoring algorithms, will allow the autonomous observation of vehicle subsystems while in their normal operating environment. Vehicle Health Management systems include all components needed to characterize system performance including: sensors, data pathways, processors, and monitoring algorithms. Figure (1.0-1) illustrates the relationship between the management and monitoring systems. For the remainder of the text, VHM will refer to Vehicle Health Monitoring. The information provided by a VHM system can be used to identify off nominal performance, and possibly reconfigure to correct for degraded or failed performance. Off-line, the recorded VHM data may subsequently be used to warn of impending failure, better schedule and perform preventive maintenance, and detect problems that would otherwise remain unnoticed, until a later flight.

The VHM system envisioned here will be designed to monitor performance of Guidance, Navigation, and Control (GN&C) system actuators, effectors, and propulsion devices using a two tier hierarchy. The top level, or global monitor, will determine whether the actuator or effector produced the expected result by monitoring the vehicle's dynamic response to known inputs. The top level of the monitor will be a dynamics based estimation algorithm which will identify off-nominal sensor or effector performance. After a particular sensor or effector has been identified, the lower level, or local, monitoring system isolates the problem further. The lower level, possibly an expert based system, fuzzy logic or learning system, will fuse the general information from the global level and conduct a search of finer granularity for the component causing the problem.

The VHM system will function during all phases of vehicle operation and store its data in-flight. Information recorded during vehicle operation

can then be "played back" to: review performance, troubleshoot problems during maintenance, and avoid unnecessary hardware 'pulls' and replacement.

The goal of this research is to develop and evaluate a model based estimator for use as the global monitor in a VHM system. To demonstrate this concept and investigate the issues of monitor architecture, a global monitor will be developed for the Space Shuttle Orbiter Reaction Control System (RCS). The algorithm should be able to identify off-nominal performance of the thrusters to an accuracy of 10% of the nominal thrust level. Figure (1.0-1) shows an overview of this VHM structure.

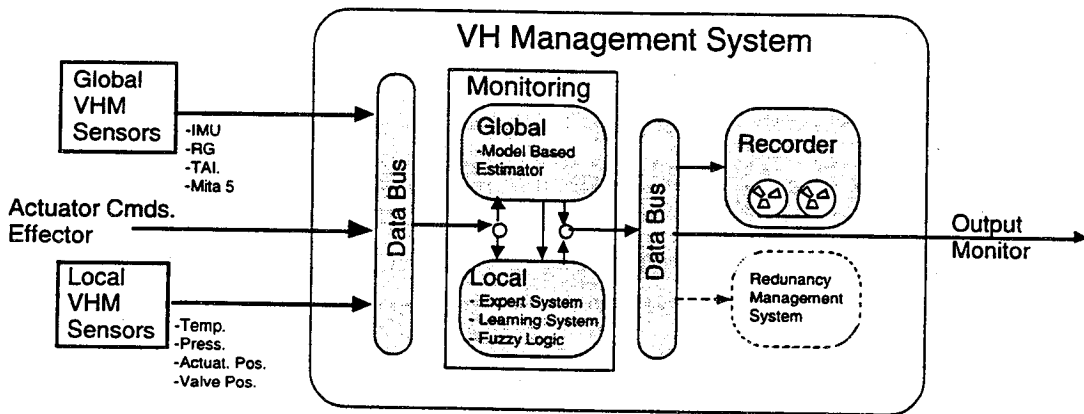


Figure 1.0-1: Overview of VHM Architecture for Shuttle RCS

The Space Shuttle RCS consists of forty-four bi-propellant jets that provide attitude control and limited three-axis maneuvering capability during all phases of Shuttle flight. In addition to the RCS, attitude control is provided by a set of aerosurfaces while in the atmosphere. These surfaces include right and left elevons, a speedbrake (i.e., split rudder), and bodyflap.

The RCS is especially well suited to VHM because it is a complex system requiring a high degree of reliability that has been prone to several in-flight problems throughout its history. For example, a jet failure occurred during the recent preparation of the Space Shuttle Discovery for its mission to rendezvous with the Russian Mir Space Station. During ground testing, a manifold pressure suddenly dropped. The problem was attributed to two leaking jets, R3A and R3R [Spacelink]. On another recent flight, a vernier jet was mistakenly deselected by the flight software due to a failed temperature

sensor. Because the vernier jets have limited redundancy, none of the vernier jets were available for use. This hampered the mission during operations with a Synthetic Aperture Radar payload, which required the Vernier Reaction Control System (VRCS) thrusters for precise earth pointing. Throughout the Shuttle program, there have been over 100 in-flight anomalies of the RCS [Anomaly]. These include not only jet failures, but also failures of the helium regulators, propellant valves, temperature and pressure sensors, electrical heaters, and injectors.

Current in-flight observation of the RCS amounts to a binary decision, failed or not failed. If the redundancy management software indicates problem with a jet for three cycles, that jet is no longer used and replaced with a jet firing in a similar direction [FSSR-RM]. A VHM system would add the capability to identify off-nominal performance in the RCS, and aid in the troubleshooting and subsequent replacement of the thruster post-flight.

Although the monitor will operate during all phases of flight, it will be designed specifically for the reentry phase. The reentry phase is the most difficult portion of flight for the estimation problem because of the large aerodynamic uncertainties present. If an acceptable solution to the estimation problem is found for reentry, then the results can be extrapolated to the other phases of flight. In addition, reentry provides a portion of flight with substantial RCS activity and large changes in rate.

The jets are the sole attitude effectors for the initial part of re-entry. As the vehicle loses altitude, falling into the increasingly dense atmosphere, dynamic pressure increases. When the dynamic pressure reaches 10 psf. the aerosurfaces are activated and augment the jets until there is sufficient dynamic pressure to control the attitude with the aerosurfaces alone. Each body axis is controlled independently. Aft RCS pods provide pitch and roll control to dynamic pressures of 10 and 40 psf., respectively. Thermal constraints cause a large portion of the re-entry to be flown at a high angle of attack. At such high angles of attack, the rudder is blanketed by the vehicle's wings rendering it largely ineffective for yaw control. The rudder does not become effective until the angle of attack is reduced to about 10°, at approximately 50,000 ft. Until that time, rudder control is largely augmented with RCS thrusters.

Estimation theory provides the foundation for the design of the global level monitor. The first model based estimator, was developed by Norbert Wiener at MIT after World War II [Wiener]. The equivalent state space domain estimator, the Kalman filter, was then introduced approximately three decades ago [Kalman]. Since its introduction, the Kalman filter has been employed extensively in aerospace engineering in areas including target tracking and vehicle GN & C.

Since the advent of the Kalman filter, estimation theory has taken several different directions. The Kalman filter framework has seen the development of many extensions and improvements. Among these are filters that provide increased numerical stability, solve various smoothing problems, and remove some of the restrictions of the Kalman filter [Gelb].

In [Deyst], a fault detection technique for the Shuttle reaction control jets during the on-orbit phase of flight was proposed. An Extended Kalman filter provides state error residuals to a generalized likelihood ratio test. This test determines if a failure occurred, and if so, which jet was failed. They were concerned with two types of failures, hard (a jet failed on or off) and soft (jet leaks). The fundamental concern in [Deyst] was to determine whether the jets were failed or not failed. In contrast, this study is concerned with measuring the thrust level produced, and determining if there is degraded performance.

More recent advancements in estimation include H_{∞}/μ linear optimal robust estimation. These estimators are founded in control theory based on the small gain theorem and are robust to a general class of noise and plant model uncertainties. A filter for continuous-time, linear, time-invariant systems at steady state was developed by [Appleby]. This filter minimizes the error for the worst case disturbance and also takes into account the structure of the uncertainty to reduce conservatism. More recently in [Mangoubi], finite horizon, time-varying, discrete-time (and continuous-time), robust estimators with arbitrary initial conditions defined over a finite or infinite horizon have been derived.

Chapter 2 provides background on the Shuttle RCS and Aerosurfaces, the two systems that provide rotational control during reentry. The various components comprising the RCS are introduced and the general operation of

the RCS is explained. In addition, common failures of the RCS are described. The location and operation of the aerosurfaces are also presented.

Chapter 3 outlines the Orbiter reentry vehicle dynamics, simulation model, and flight control representation. The rotational vehicle dynamics are developed along with models of the aerosurfaces, RCS thrusters and sensors. All of these models are combined together to make the entry simulation used for testing and providing realistic input to the estimation algorithm.

Chapter 4 presents the issues associated with the design of a global monitor and follows the development of a Kalman filter based estimation algorithm. A discrete Kalman filter is derived and an estimator is implemented for thrust estimation. Also discussed in this chapter is the method for incorporating the filter outputs into the VHM system.

In Chapter 5, the Kalman filter designed in Chapter 4 is analyzed. First, open loop simulations are performed to examine the estimation error for different types of jet firings and error dynamics. The filter is then tested in a closed loop simulation of higher fidelity with two benchmark maneuvers. The robustness of the Kalman Filter design to various errors and noise sources is investigated.

In Chapter 6, a cursory investigation is made into the applicability of robust filters for the VHM estimation problem. An overview is given of the minimax and the generalized minimax estimator. A robust minimax estimator is shown to be significantly less sensitive to aerodynamic parametric plant modeling uncertainty.

2.0 Space Shuttle Flight Control Effectors

2.1 Space Shuttle RCS

The Space Shuttle Reaction Control System (RCS) provides thrust for attitude control and limited translational maneuvering during all phases of flight, from ascent through reentry.

Three separate pods, one forward and two aft, make up the RCS. The forward pod is located in the forward nose section. The aft systems (right and left) are located in the combined RCS / Orbital Maneuvering System (OMS) pods. Figure (2.1-1) shows the location of the pods on the orbiter.

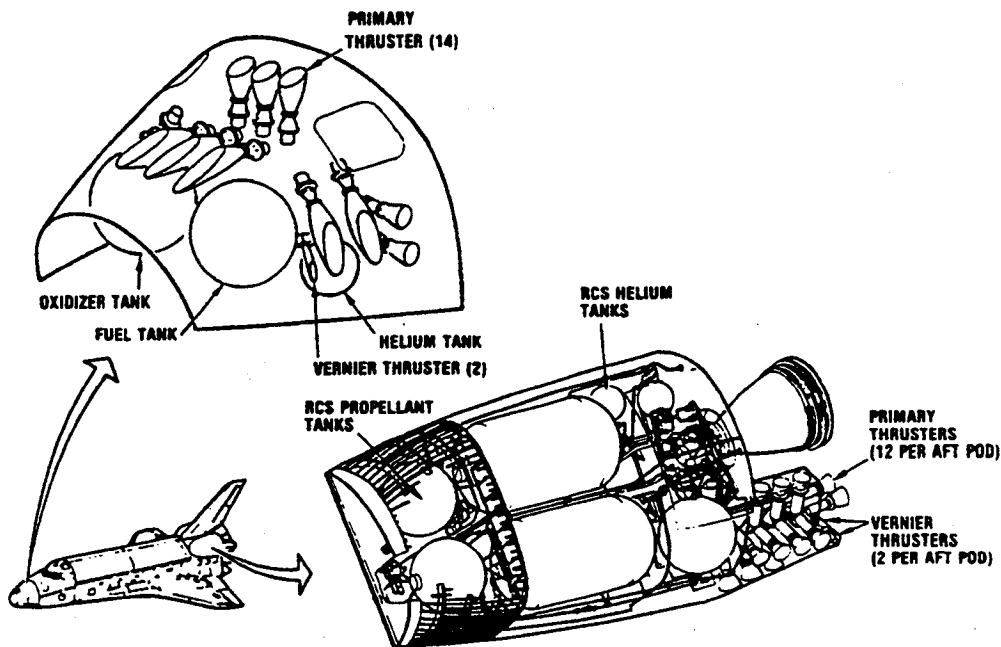


Figure 2.1-1: Location of RCS Pods

Each RCS is composed of high pressure helium tanks, pressure regulation and relief components, propellant tanks, manifolds (to distribute the propellants to the jets), isolation valves, thrusters, and an electrical heating system. In the RCS, there are a total of 44 thrusters. Thirty-eight of the jets are primary jets,

providing nominally 870 lb. thrust in a vacuum. These thirty-eight jets are redundant, providing attitude control and limited three axis translational maneuvering for the Shuttle. There are also six smaller thrusters, the vernier jets. The vernier jets provide only 25 lb. of thrust and are used for fine pointing attitude control. The vernier thrusters have very limited redundancy.

2.1.1 Propellant Storage and Feed

Two helium tanks provide high pressure gaseous helium to the oxidizer and fuel tanks in each RCS. The high pressure helium provides the necessary energy to force the propellants through the plumbing to the thrusters. Figure (2.1-2) illustrates the plumbing of the forward and rear pods.

Several isolation valves are interspersed throughout the RCS to separate the various components. The first of these valves are the four helium isolation valves in each RCS pod (2 fuel, 2 oxidizer) between the helium and propellant tanks. There are two valves for each tank corresponding to the two redundant helium regulators. The valves for each tank are in parallel and serve to isolate the helium and propellant tanks.

Below each of the helium isolation valves is a helium regulator. These regulators step down the helium pressure from about 3000 psi. to 256 psi. for delivery to the propellant tanks [SODB]. After the regulators, the helium lines in all the RCS pods rejoin and enter the Quad Check Valves. These valves are used to prevent the propellant from flowing back upstream into the helium supply.

At the output of the quad check valve is plumbing to prevent over pressurization of the propellant tanks. These devices consist of pressure relief valves, a burst disc, and a manually operated isolation valve.

The propellant tanks are located down line of the pressure relief components. There are two propellant tanks in each pod, one fuel and one oxidizer. The oxidizer is nitrogen tetroxide and the fuel is monomethyl hydrazine. These two liquid compounds are hypergolic, meaning they combust when they come in contact with each other. In the propellant tanks, the gaseous helium and liquid propellants coexist as a random, ever-changing mixture because there is nothing separating the two. As a result, each propellant tank contains an acquisition device that operates on the surface tension properties of

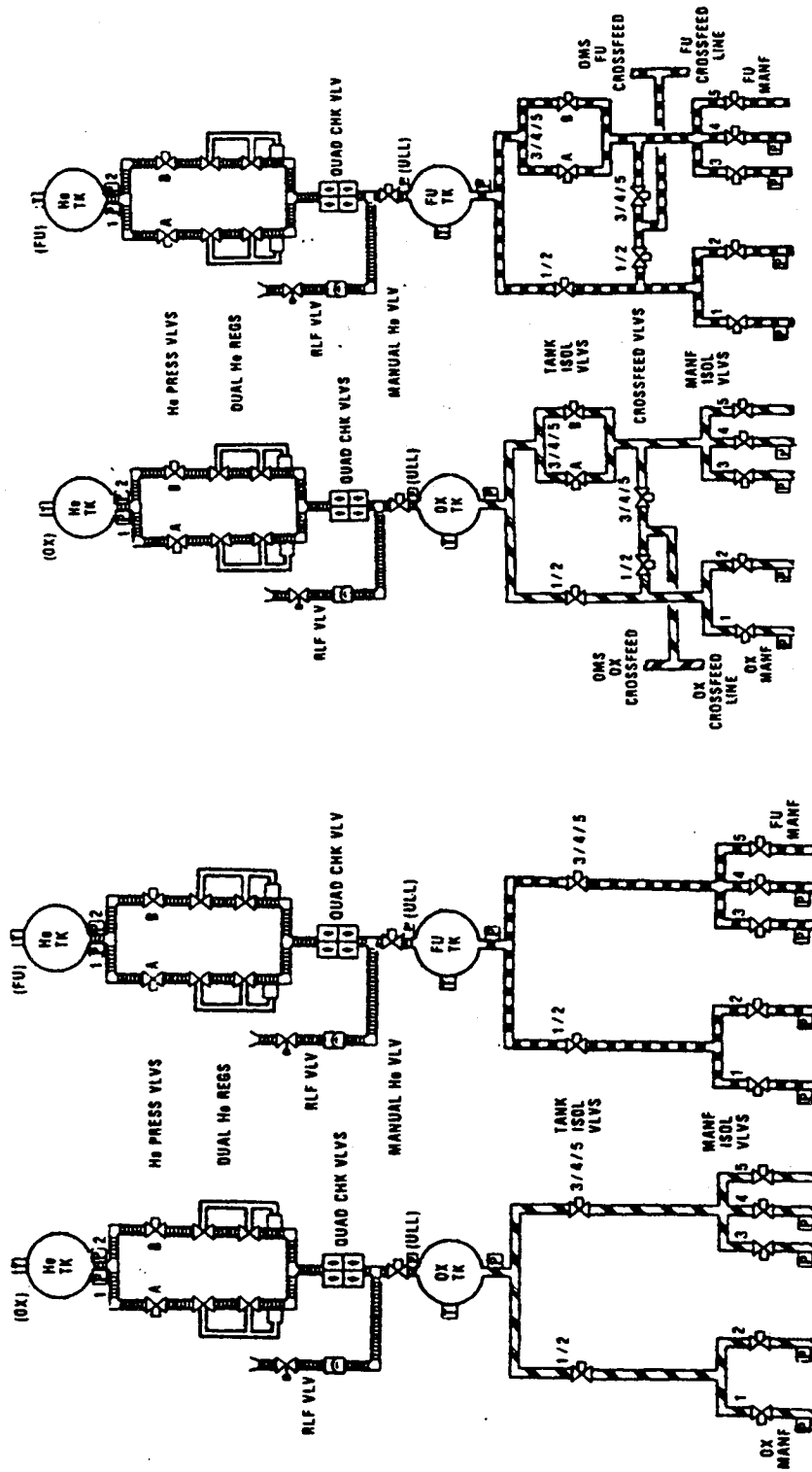


Figure 2.1-2: Plumbing of Forward and Rear RCS Pods

the liquid propellant to ensure propellant is expelled from the tank over a wide range of accelerations and orientations.

The acquisition devices in the forward RCS pod are designed for primarily low gravity environments while the acquisition devices in the rear pods are designed to operate in both high and low gravity environments [Spacelink]. From the tanks, the propellants are supplied to the individual thrusters through a system of valves and manifolds.

The primary manifolds (1/2/3) on the forward RCS pod supply four primary jets. Manifold four supplies only two primary jets. The vernier manifold (5) supplies the two forward vernier RCS jets.

Each of the primary manifolds (1/2/3/4) in the rear RCS pods, supply three primary jets. The vernier manifold (5) supplies two vernier jets in each rear pod.

Several isolation valves separate the propellant tanks from the manifolds and the crossfeed lines. The crossfeed lines allow the exchange of propellants between the right and left RCS pods. In the rear pods, there are three isolation valves immediately below the propellant tanks, two in parallel for manifolds 3/4/5 and one for manifolds 1/2. Also in the rear RCS pod there is one isolation valve for each of the manifold groups for crossfeeding. In the forward pod, there are only two isolation valves, one for manifolds 1/2 and one for manifolds 3/4/5. Below the manifold group isolation valves, are the individual manifold isolation valves. There are five of these per pod, one for each of the manifolds. The isolation valves for the vernier manifolds are low pressure solenoid valves that are magnetically latched open and spring loaded closed. The remainder of the propellant isolation valves are ac-motor operated, and are made up of a ball lift-off flow control device and actuator assembly (motor and gear train).

2.1.2 Thruster Design and Layout

The forward RCS houses fourteen primary jets and two vernier jets. Each of the rear RCS pods contains twelve primary jets and two vernier jets. The Figure (2.1-3) shows the different jets on a rear pod. The jet placement on the forward pod is illustrated in Figure (2.1-1).

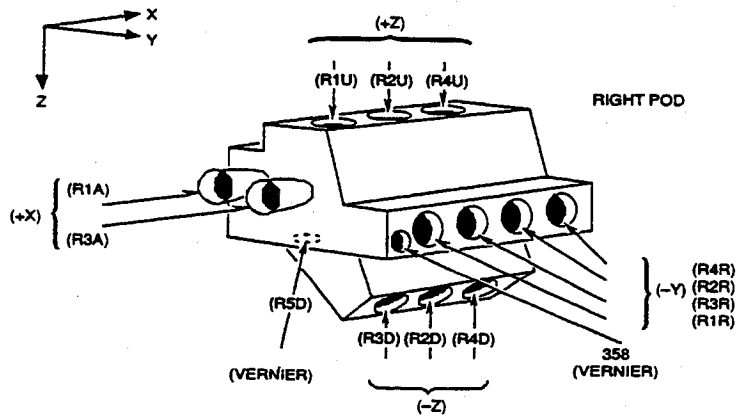


Figure 2.1-3: Rear RCS Pod

Each RCS thruster contains the following components: fuel and oxidizer valves, injector head assembly, combustion chamber, nozzle and a junction box.

When a thruster is commanded to fire, an electrical thrust-on command is sent to both the fuel and oxidizer valves. These electrical signals energize a solenoid, the hydraulic pressure opens the main valve poppets, and the propellants to flow to the injectors. In the thrusters, the propellants are expelled through heated injector assemblies where they come in contact and ignite. The injector head assembly in the primary jets consist of injector holes arranged in two concentric rings. The inner ring is fuel and the outer ring is oxidizer. The holes are canted toward each other causing impingement of the fuel and oxidizer in the combustion chamber. In the vernier jets, there are only two holes, one each for oxidizer and fuel. Like the primary jets these holes are canted toward each other causing combustion within the combustion chamber [Spacelink].

From the injectors, the propellants unite in the combustion chamber, where they combust, expand through the nozzle and produce thrust. When the thruster is commanded off, the valves are de-energized and closed by spring and pressure loads.

2.1.4 RCS RM System

Currently the only form of automatic fault detection on the RCS jets is the existing Redundancy Management (RM) system in the Shuttle flight software.

This software contains modules that perform tasks of: tracking available jets, monitoring for failed on jets, monitoring for failed off jets, monitoring for jets that are leaking, processing the status of the manifolds, and tracking a jet priority table.

The JET-FAILED-OFF-MONITOR checks for jets that have failed-off, meaning that the jet does not fire when commanded. The RM software performs this task by using the chamber pressure signal and the jet fire command. If the chamber pressure does not indicate a jet has fired and a jet fire command is present, this constitutes the initial condition for jet-off failure. This condition must exist for a number (set preflight) of consecutive cycles for the jet to be failed off. The maximum this number can be set to is six cycles. [FSSR-RM] and [I-Load] indicate that for most missions this limit is set to three cycles. The cycle time for the jet failed off processing is 80 ms for all major modes of flight. If a jet is failed off, the jet is automatically deselected and the jet selection is reconfigured.

The JET-FAILED-ON-MONITOR is similar to the failed off monitor. A jet is considered failed-on when the jet is firing, but has not been given a firing command. This algorithm uses a jet fire command and the Reaction Jet Drivers (RJD) output. The RJD process electrical signals to and from the individual thrusters. If no command is sent but the RJD indicates the jet is firing, then the initial condition is met for failed-on status. If this condition exists for more than a preloaded number of cycles, the jet is considered to be failed on. The set number of cycles is three for most flights according to [I-Load]. It can be a maximum of six. The cycle time for checking jet-on failure is 1.92 seconds during all major modes of flight. If a jet is failed-on, the jet is not automatically deselected by RM (warning lights illuminate and audible alarms sound alerting the crew, who in turn must manually deselect the failed-on jet).

The JET-LEAK-MONITOR, like the failed on and the failed off monitors, has a criteria that must be met for a given number of consecutive cycles. The criteria for a jet leak failure is that either the fuel or the oxidizer injector temperature sensors falls below a preset limit. The concept of this algorithm is that a propellant leaking, without combusting, causes evaporative cooling of the injector. The critical temperature for the primary jets are 30° F for the oxidizer and 20° F for the fuel. For the vernier jets the temperature limit is 30° F for both

fuel and oxidizer except during operations on-orbit and prior to ascent where it is 130° F. The cycle time for jet leak monitoring is 1.92 seconds. If a jet is failed leaking, audible and visual warnings are issued to the crew, in addition the leaking jet is automatically deselected and the jet selection is reconfigured accordingly.

2.1.3 RCS Sensor Data

The Space Shuttle has several sensors that are available for monitoring the RCS. The global scale sensors for attitude and rate measurement on the Shuttle include the Inertial Measurement Units and the Rate Gyros. These sensors may be used to measure the vehicles rigid body dynamic response to jet firings. Also there is a whole suite of local sensors, specific to almost each component of the RCS.

Each thruster has sensors that include a chamber pressure sensor, and two temperature sensors, one for each of the injectors (fuel and oxidizer). In addition there are temperature and pressure sensors for all the helium, fuel and oxidizer tanks. Each valve has an open or closed sensor consisting of a micro switch that indicates open or closed. Each manifold has a pressure sensor. Figure (2.1-4) illustrates these various sensors.

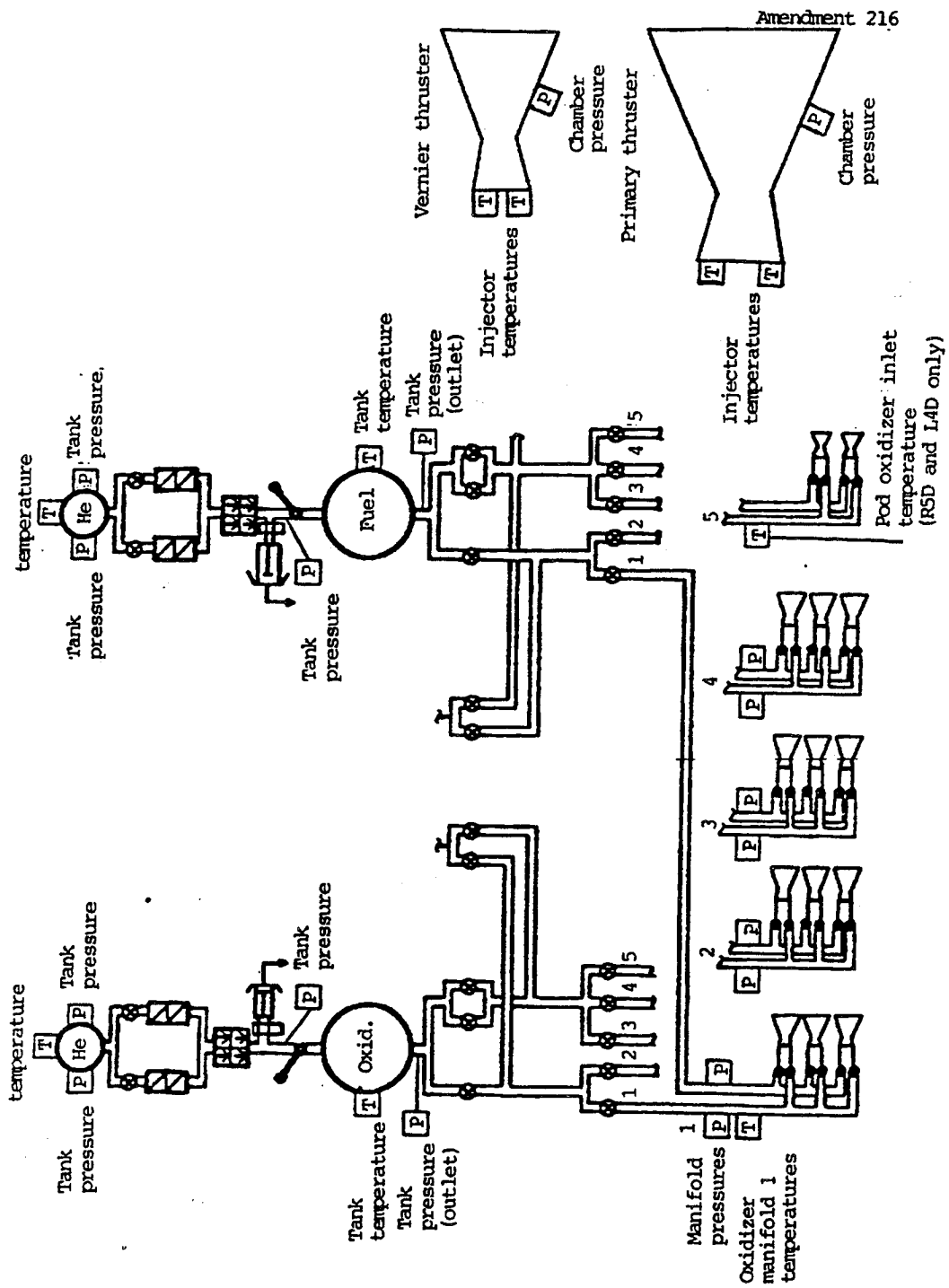


Figure 2.1-4: RCS Sensor Locations

2.1.5 Typical RCS Failures

The complex RCS has been prone to several minor problems throughout the Space Shuttle's history. Since the Shuttles began flying in 1981, there have been over one hundred in-flight anomalies of the RCS. These anomalies have included fuel and oxidizer leaks, injector heater failures, valve failures, and sensor failures. Of all the problems logged through flight STS-51, forty percent of the anomalies involved problems with the jets and about one-fourth of those involved leaking jets [Anomaly]. Other problems included valves becoming stuck open or closed, propellant feed problems like helium ingestion, and regulator anomalies. Common failures and their causes and effects are summarized in Table (2.1-1).

Helium ingestion occurs when helium enters the propellant acquisition device. The ingestion of helium occurs when the propellant demand is high because the flow effects become larger than the surface tension effects, allowing helium to enter the acquisition device. This helium usually does not cause catastrophic failure. Rather, the bubble passes through the system and is expelled through the jets. When the bubble passes through the jet, production of thrust is interrupted and the jet 'burps.' These helium bubbles usually do not cause a problem (other than interrupted thrust) for primary jets. However, for verniers the bubble may be persistent enough to cause the system Redundancy Management software to fail the jet. There does exist a very small probability that the helium bubble could lead to combustion instability and explosion of the jet. Because of this possibility, the number of jets firing from the same pod simultaneously is limited to four [SODB].

Another propellant feed problem is helium regulator failure. At times, one of the two helium regulators has failed forcing the system to depend on the secondary regulator.

Leak failures often occur at the injectors of the thrusters. Both oxidizer and fuel leaks have occurred with similar frequency. As stated above this is the most common type of RCS failure. The helium regulators are also prone to leaking.

Anomaly	Description	Cause	Effect
Thruster Leak	Propellant escaping from jet	Injector valves fail to close	<ul style="list-style-type: none"> •Small disturbance torque •Reduced temperature •Possible deselect by RM •Possible payload contamination
He Regulator Failure	Regulator does not regulate to proper pressure	Leaking seal in regulator	<ul style="list-style-type: none"> •Loss of He pressurant •Reliance on one regulator
Sensor Failure	Any of: •valve position •manifold status •tank pressure •tank temperature •injector temperature •chamber pressure incorrect	Any Sensor Failure	<ul style="list-style-type: none"> •False alarms •False deselects
Injector Heater Failure	Electrical heaters do not heat injector rings	<ul style="list-style-type: none"> •Failed heater element •Failed thermostat 	•Possible deselect as leaking
He Ingestion	He gas in propellant lines	<ul style="list-style-type: none"> •Large flow demand •Multiple jets firing simultaneously 	<ul style="list-style-type: none"> •Interrupted thrust •Possible deselect by RM

Table 2.1-1: Summary of Typical RCS Failures

Many of the recorded anomalies with the RCS can be attributed to sensor failures. For example, the sensors monitoring isolation valve positions have failed causing false "alarms." Other sensor failures reported include false temperature readings for the injectors.

Other miscellaneous RCS problems include injector heaters failing on or off, tank pressure surges and erratic chamber pressures

2.2 Space Shuttle Aerosurfaces

The Space Shuttle, with its large delta wings does not have the control surfaces of a conventional airplane. Rather, the Shuttle has five movable control

surfaces: inboard and outboard elevons, a rudder, a speedbrake, and a bodyflap. Figure (2.2-1) illustrates the location and direction of positive deflection for each of the surfaces. Table (2.2-1) presents the maximum deflection and rate of each aerosurface.

2.2.1 Elevons

The Shuttle does not have elevators and ailerons to provide pitch and roll control authority like a conventional aircraft. Instead the control of roll and pitch are combined in the elevon. Each elevon is split into an inboard and outboard section. It is possible for each of the four segments to operate independently. However, during reentry the inboard and outboard sections operate in unison, effectively reducing the four surfaces to two. The elevons have a range of -35° to $+20^\circ$ and are rate limited at a rate of $20^\circ/\text{s}$.

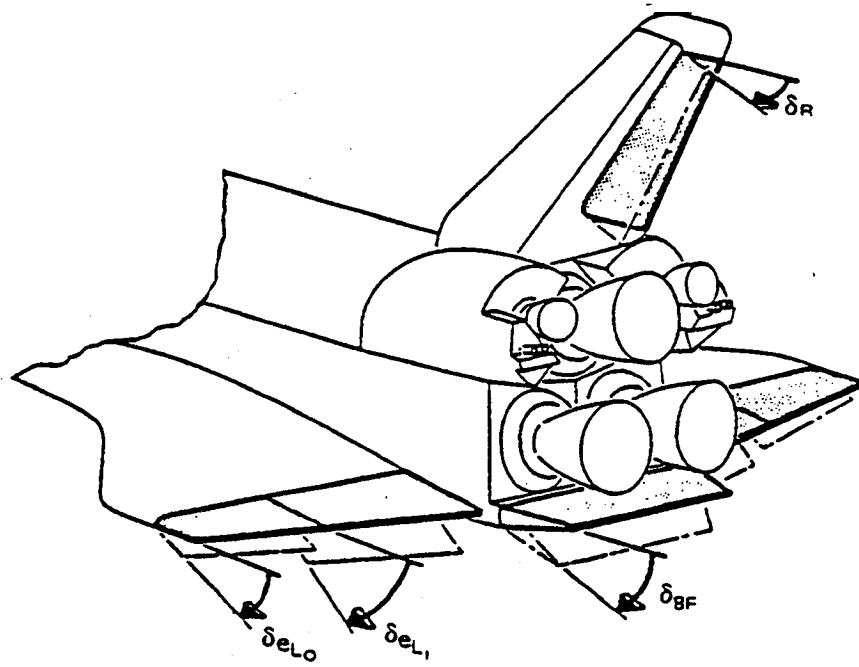


Figure 2.2-1: Location and Direction of Shuttle Aerosurface Deflections

Control Surface	Positive Deflection	Maximum Displacement (°)	Rate (°/sec)
Elevons	δ_{El}, δ_{Er}	-35 to +20	20
Rudder	δ_R	± 22.8	10
Speedbrake	δ_{SB}	0 to 87.2	5
Body Flap	δ_{BF}	-11.7 to 22.55	1.3

Table 2.2-1: Maximum Aerosurface Deflections and Rates

The elevon deflections also define two more conventional aerosurface deflections, elevator and aileron deflection. The elevator deflection is defined to be the average of the right and left elevon deflections. A positive elevator deflection results in a negative pitch moment.

$$\delta_e = \frac{1}{2}(\delta_{e_L} + \delta_{e_R}) \quad (2-2-1)$$

The aileron deflection is defined to be one half the difference of the left and right elevon deflections. Positive aileron deflection results initially in a positive roll torque.

$$\delta_a = \frac{1}{2}(\delta_{e_L} - \delta_{e_R}) \quad (2-2-2)$$

Neither, the ailerons nor the elevator can be at maximum deflection simultaneously, because the definitions are both dependent on the elevon position. This interdependence is illustrated in Figure (2.2-2).

2.2.2 Rudder

The rudder on the Shuttle is very similar to that of a conventional aircraft. It is located on the aft portion of the vertical stabilizer. The rudder has a range of $\pm 22.8^\circ$ with no speedbrake deflection and is rate limited at 10 (°/s).

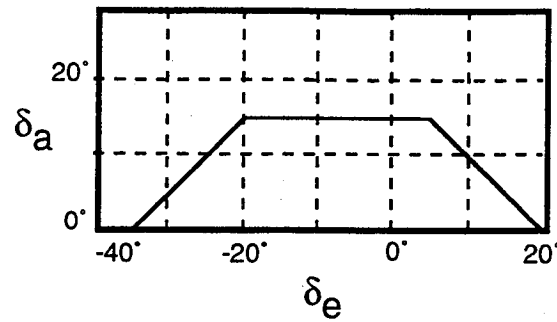


Figure 2.2-2: Maximum Simultaneous Aileron and Elevator Deflection

2.2.3 Speedbrake

The speedbrake is actually a split rudder. The rudder is composed of right and left panels that open symmetrically to create the speedbrake. The speedbrake provides lateral stability during the later part of reentry. The range of the speedbrake is 0° to 87.2° and is rate limited at 5.0 ($^\circ/\text{s}$). The maximum deflection of the speedbrake is dependent on the position of the rudder and vice-versa. If one surface is at its maximum then the maximum deflection of the other surface is reduced. The interrelationship of the two surfaces is illustrated in Figures (2.2-3) and (2.2-4).

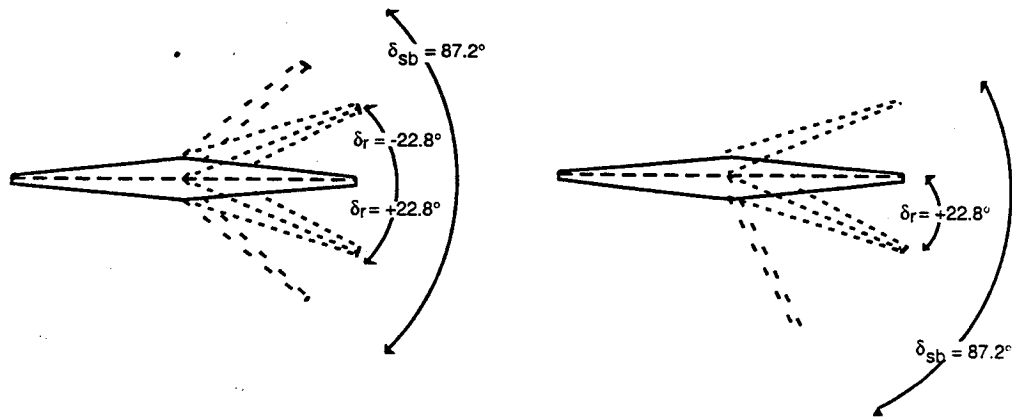


Figure 2.2-3: Speedbrake and Rudder Deflection

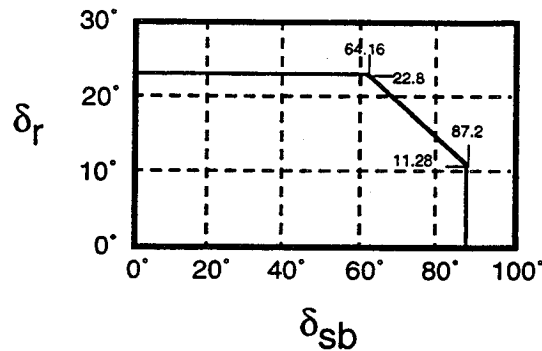


Figure 2.2-4: Maximum Simultaneous Rudder and Speedbrake Deflection

2.2.4 Bodyflap

The remaining surface is the bodyflap, a horizontal control surface that is mounted ventrally on the centerline. The bodyflap is essentially a pitch trim surface. If the vehicle center of mass is either fore or aft of its nominal location, an appropriate body flap deflection “restores” the vehicle dynamics as if the center of mass were in its nominal location. This trimming prevents saturation of the elevons. The range of the bodyflap is -11.7° to $+22.55^\circ$ and is rate limited at $1.3^\circ/\text{s}$.

3.0 Space Shuttle Reentry Vehicle Control and Dynamics

3.1 Reentry Overview

Shuttle reentry begins with the deorbit burn. For this maneuver, the Shuttle is oriented in a tail first position (the nose is facing away from the direction of travel). The OMS jets fire to slow the vehicle, allowing capture by the earth's gravity and atmosphere. The RCS jets reorient the orbiter to a nose first position. Due to thermal constraints, the orbiter flies the first part of reentry at a high angle of attack, 40° . A 40° angle of attack is maintained until the orbiter descends and slows to below Mach 10. During this period of high angle of attack, the decent rate of the orbiter is controlled by the bank angle. After passing through Mach 10, the orbiter gradually reduces its angle of attack to approximately 10° . The RCS thrusters alone are used to control the vehicle's attitude until enough dynamic pressure accumulates for the aerosurfaces to become effective. The control surfaces first become effective at Entry Interface. Entry Interface nominally occurs at 30 minutes before landing at an altitude of approximately 400,000 ft. At this time, the control surfaces are activated. Attitude control is provided by both the RCS and the aerosurfaces until sufficient dynamic pressure exists for the aerosurfaces to control the vehicle alone.

Elevons are the first surface to become effective. When onboard sensors measure a dynamic pressure of 10 psf. (at an altitude of approximately 265,000 ft), roll jets are deselected and roll control is provided solely by the elevons (aileron deflection by differential elevon). Similarly, when the dynamic pressure reaches 20 psf. pitch control is provided by the elevons and pitch thrusters are disabled for the remainder of reentry.

Yaw is the final axis to be totally controlled by the aerosurfaces. Adverse aerodynamics render the rudder ineffective during much of reentry. The poor aerodynamics are a result of the high angle of attack flown throughout reentry. At high angles of attack the Shuttle body and wings shadow the rudder. The rudder first becomes effective when the angle of attack decreases below 10° . Yaw jets are still active until an altitude of about 45,000 ft.

Figure (3.1-1) shows a nominal reentry profile. The circles represent flight conditions for linear models that were incorporated in this thesis.

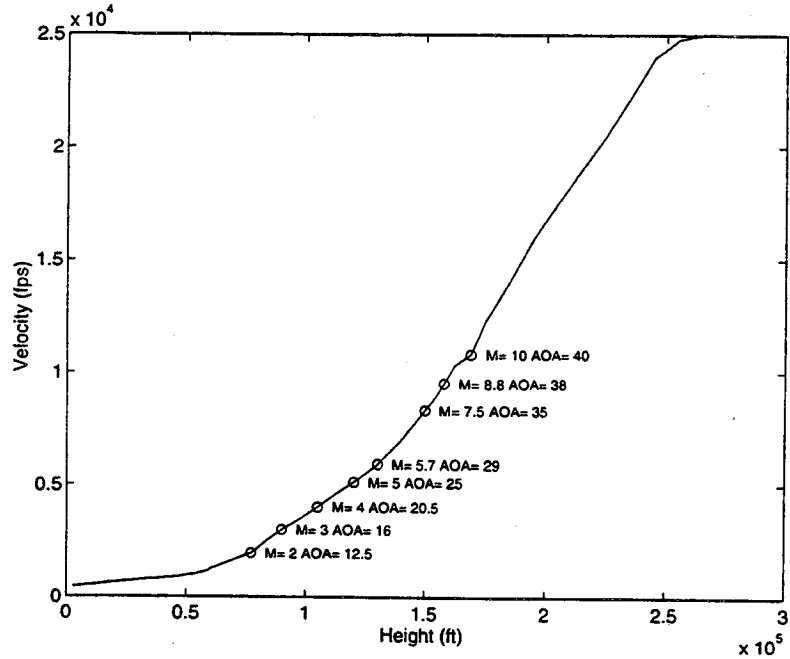


Figure 3.1-1: Shuttle Reentry Profile and Thesis Models

3.2 Entry Simulation Model

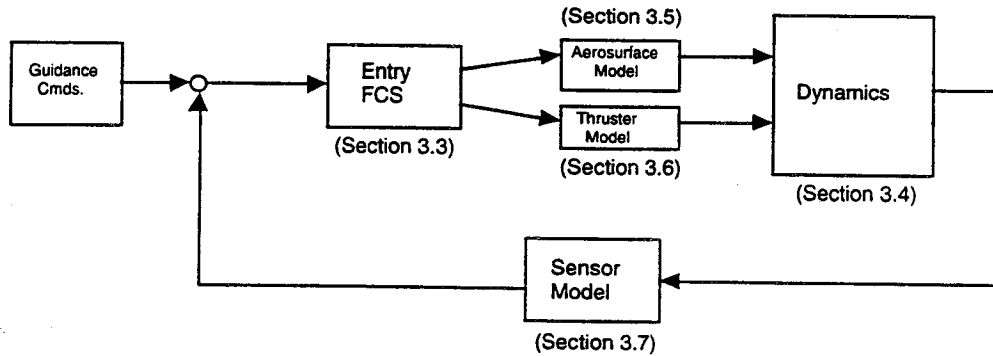


Figure 3.2-1: Block Diagram of Reentry Simulation

Figure (3.2-1) illustrates the structure of the reentry simulation developed in this study. The simulation provides a testbed for evaluating the performance of designed estimators as well as provides realistic commands to be modeled.

The guidance commands are fed into the reentry flight control algorithms. There is one control channel for each of the three axes: roll, pitch, and yaw. The

roll and yaw flight control channels are coupled. Entry flight control takes angle of attack and bank requests and commands the proper aerosurface deflections and RCS jet firings to accomplish the requested maneuver. The incorporation of the entry flight control system is discussed in greater detail in Section 3.3. The aerosurface and RCS jet models used in simulation are described in Sections 3.4 and 3.5 respectively.

A model of the rigid body rotational dynamics is described in Section 3.6. Sensor models feedback the response of the dynamics model to the issued commands. Sensors currently onboard the Shuttle as well as other stand alone packages that could be implemented in the estimator based health monitoring system are described in Section 3.7.

3.3 Entry Flight Control System

The Reentry attitude flight control system is documented in [FSSR-GNC]. The essential elements of the current re-entry flight control software are implemented in a SIMULINK model. The model of the flight control software was created to provide realistic input to the dynamics for simulation and test the thrust estimation capability of the health monitoring algorithm. An overview of the flight control system is given in Figure (3.3-1).

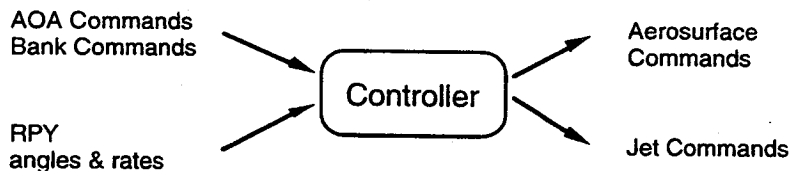


Figure 3.3-1: Overview of Entry Flight Control

The entry flight control system is primarily a rate feedback control system. The commands of angle of attack and bank angle are converted into a required rate. A combination of aerosurface deflections and RCS jet firings provide the required rate. The blending logic that determines the relative magnitude of control between jets and aerosurfaces is a function of angle of attack, current dynamic pressure and flight mode. In the control model developed for this study, the manual, control stick steering channels were not implemented.

Figures (3.3-3) (3.3-4) and (3.3-5) show the roll, pitch and yaw entry control block diagrams used in the SIMULINK model for flight control. The

names of the individual blocks match the software module names in [FSSR-GNC] where appropriate.

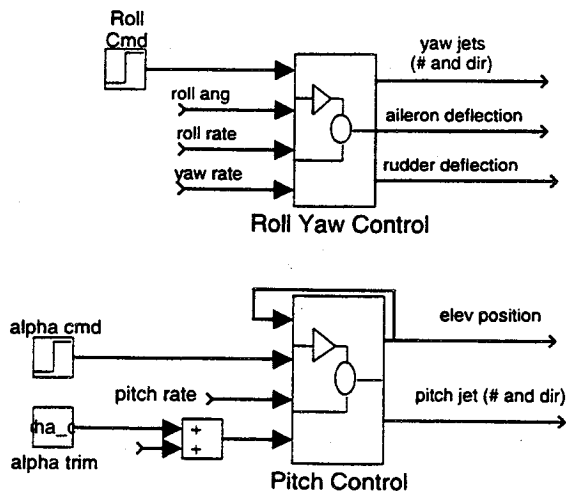


Figure 3.3-2: Block Diagram of Entry Flight Control System

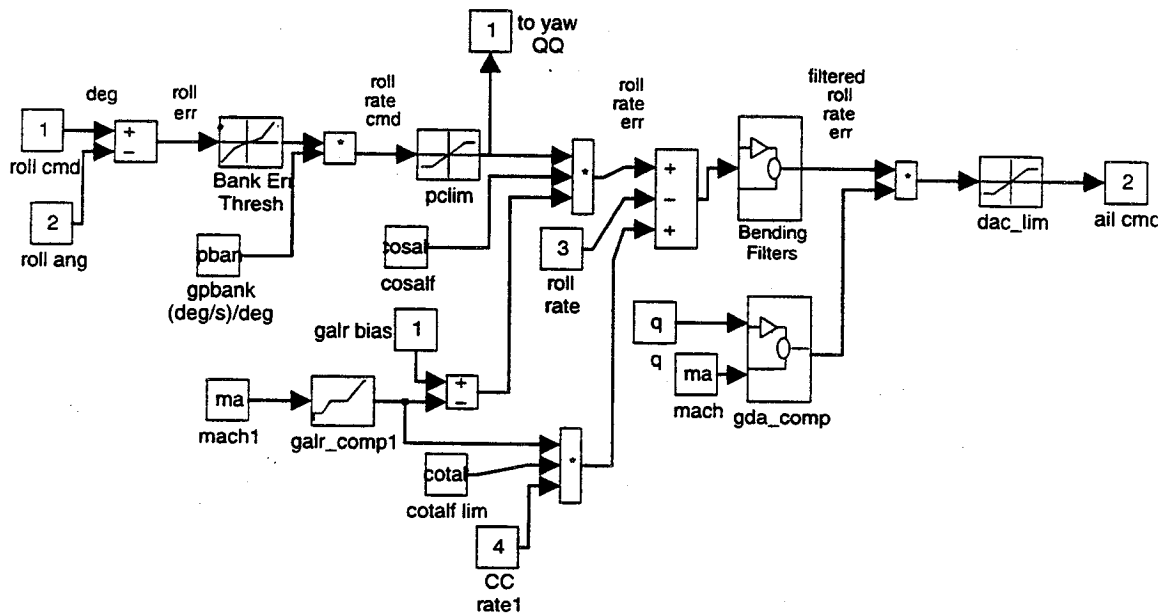


Figure 3.3-3: Model of Roll Controller used in SIMULINK Simulation

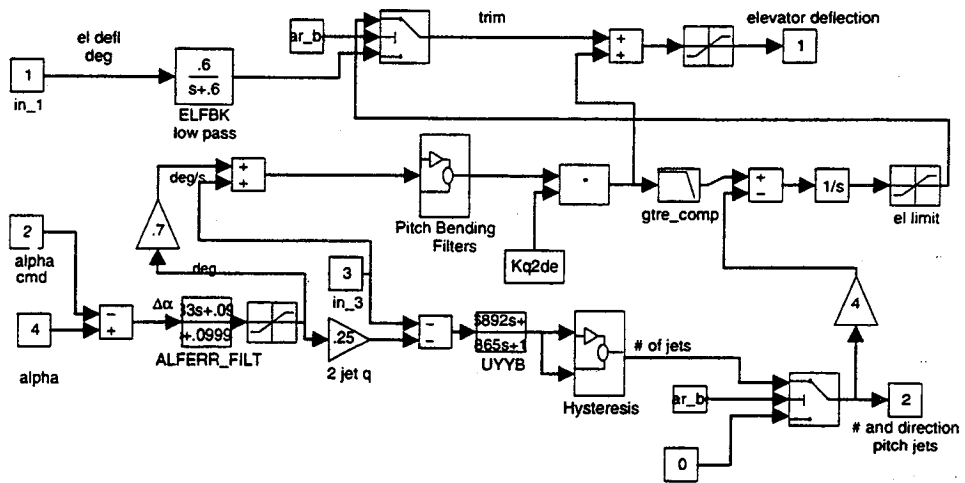


Figure 3.3-4: Model of Pitch Controller used in SIMULINK Simulation

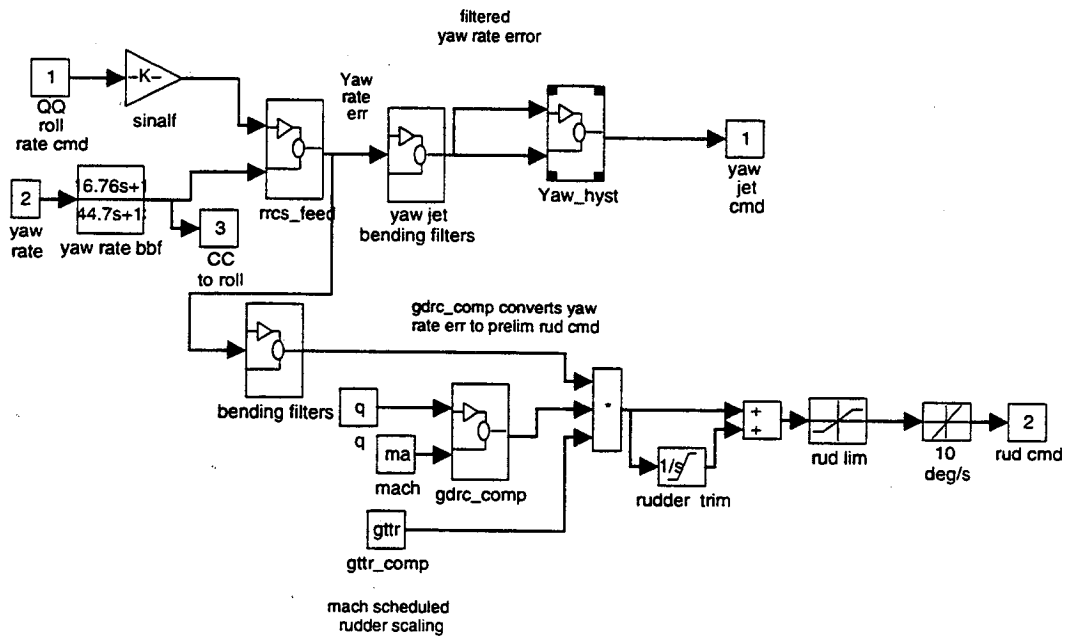


Figure 3.3-5: Model of Yaw Controller used in SIMULINK Simulation

3.4 Space Shuttle Aerodynamic Reentry Model

Since the RCS provides attitude control moments during reentry, the rotational vehicle dynamics have been mechanized to provide the estimator truth model.

The model structure of the Space Shuttle reentry dynamics used for simulation is that developed in [Zacharias] and is detailed in the sections to follow. This model is a simplified reentry model that is dependent on Mach number, angle of attack and vehicle properties. The independent parameters needed to specify the model were obtained from [OADB]. This reference lists a nominal reentry trajectory profile, Figure (3.1-1), and the associated parameters at several points in time throughout the trajectory. Appendix B tabulates the relevant model and vehicle parameters.

3.4.1 Coordinate Frames

The body axis frame is a local coordinate frame aligned with the orbiter body. The x-body axis extends through the orbiter nose and is positive in the forward direction. Rotation about the x-body axis, roll, is defined to be positive when the right wing is down. The y-body axis extends out the right wing of the orbiter. Rotation about the y-body axis, pitch, is positive when the nose is up. The z-body axis extends down, defining rotation about it, yaw, to be positive when the nose is rotated right. The body axis frame is illustrated in Figure (3.4-1).

Rotational rates about the x , y , and z body axes are defined as p , q , and r respectively.

Another coordinate frame used in the Shuttle models is the stability axis frame. This velocity frame is defined by two rotations (α and β) with respect to the body axis frame, and aligns the body x-axis with the freestream velocity. The first rotation is about the y-body axis by α . The second rotation is about the z' axis by β . These rotations are illustrated in Figure (3.4-2). The bank angle is then defined as the rotation about the freestream velocity vector. Figure (3.4-3) shows the angles and their relationship in the stability axis frame.

The angles are signed such that: a positive pitch rotation increases angle of attack (at zero sideslip), a positive yaw rotation decreases sideslip (at zero angle

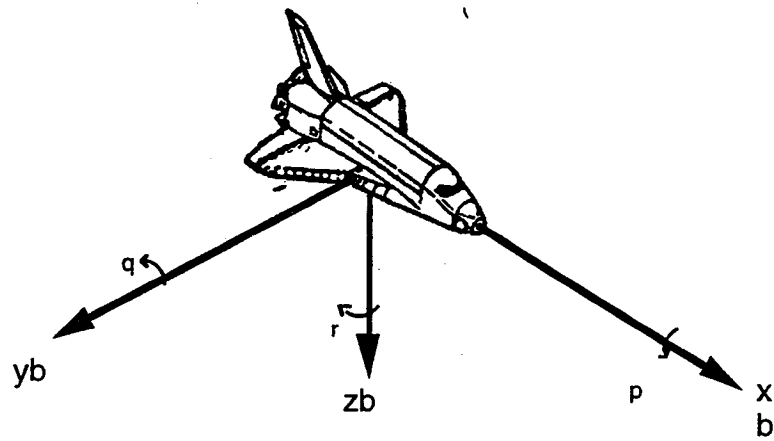


Figure 3.4-1: Body Axis Frame

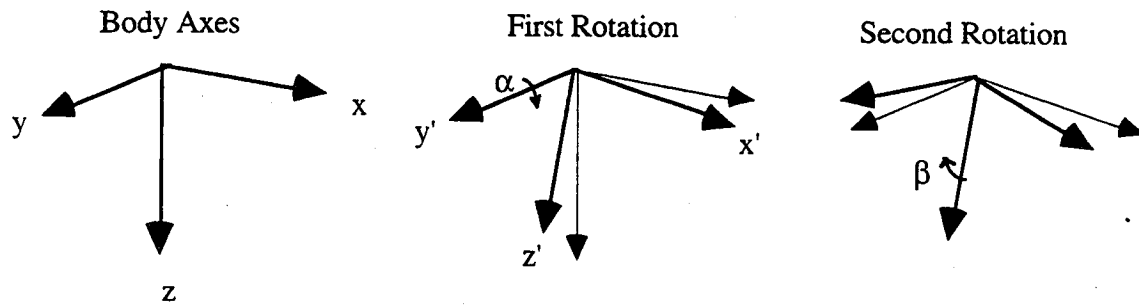


Figure 3.4-2: Rotation from Body to Stability Axis Frame

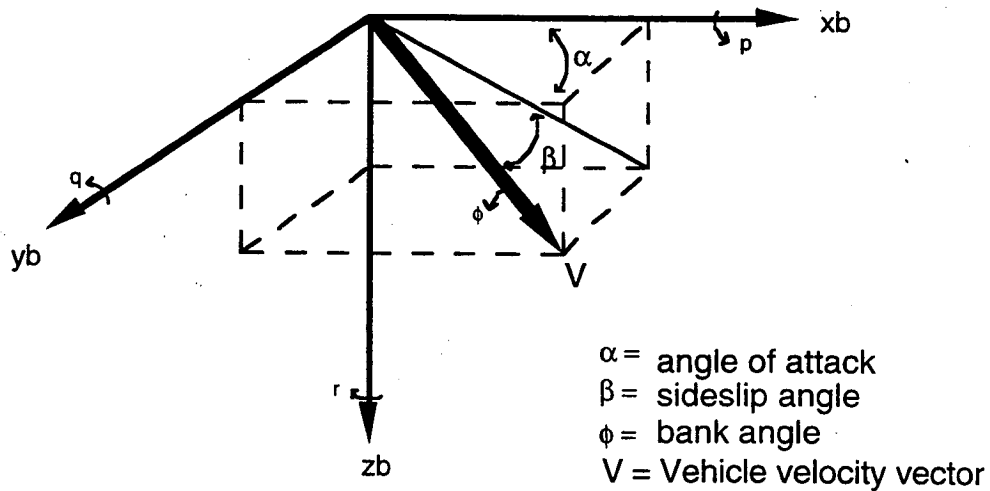


Figure 3.4-3: Stability Axis Frame

of attack), and a positive roll angle increases bank (at zero angle of attack and sideslip).

This stability axis frame is convenient for representing flight, since all velocities are referred to the freestream or airmass velocity direction. The attitude dynamics are easily described in this coordinate frame. In addition, the reentry flight control monitors sideslip angle and issues commands for angle of attack. To express stability forces in the body frame one simply performs the rotation α about the y-body axis. This relationship assumes the sideslip angle is small and that the "small angle" assumption is applied.

3.4.2 Equations of Motion

The rotational equations of motion are:

$$\tau_{\text{total}} = \mathbf{I} \dot{\omega} + \omega \times \mathbf{I} \omega \quad (3.4-1)$$

where:

τ_{total} = sum of all external torques acting on vehicle

ω = angular rates in body axes = $(p \ q \ r)$

$$\mathbf{I} = \text{Inertia Tensor} = \begin{bmatrix} I_{xx} & 0 & -I_{xz} \\ 0 & I_{yy} & 0 \\ -I_{xz} & 0 & I_{zz} \end{bmatrix} \quad (3.4-2)$$

It is assumed that the products of inertia I_{xy} and I_{yz} are zero because the x-z plane is a plane of symmetry.

$$I_{xy} = I_{yz} = 0 \quad (3.4-3)$$

Next it is assumed the only torques acting on the vehicle are those due to thruster firings and aerodynamic forces. Separating total torque into aerodynamic and jet torques about each of the three body axes gives,

$$\tau_{\text{total}} = \tau + \hat{\tau}$$

$$\tau = \begin{bmatrix} \mathbf{L} \\ \mathbf{M} \\ \mathbf{N} \end{bmatrix} \quad \hat{\tau} = \begin{bmatrix} \hat{\mathbf{L}} \\ \hat{\mathbf{M}} \\ \hat{\mathbf{N}} \end{bmatrix} \quad (3.4-4)$$

τ = aero torques
 $\hat{\tau}$ = jet torques

Expanding Equation (3.4-1) gives,

$$\begin{aligned} I_{xx}\dot{p} - I_{xz}\dot{r} + (I_{zz} - I_{yy})qr - I_{xz}pq - L &= \hat{L} \\ I_{yy}\dot{q} + (I_{xx} - I_{zz})pr - I_{xz}(p^2 - r^2) - M &= \hat{M} \\ I_{zz}\dot{r} - I_{xz}\dot{p} + (I_{yy} - I_{xx})pq - I_{xz}qr - N &= \hat{N} \end{aligned} \quad (3.4-5)$$

To linearize the above equations, an equilibrium flight condition is imposed and the equations of motion are derived for the perturbations from equilibrium. Note that at equilibrium, the net torque is zero. The derivation of the equations of motion for the perturbations is done in the following manner.

First each variable is replaced by its equilibrium value plus a perturbation. Any terms containing perturbations of second order or greater are neglected. Next, the small angle assumption is applied and the equilibrium equations are subtracted from the equations containing the equilibrium condition plus the perturbations. What remains are equations for the perturbation dynamics alone. In the resulting linear equations (3.4-6), the lower case variables correspond to their respective uppercase counterparts. A naught subscript (X_0) indicates an equilibrium value. All other lower case variables are perturbations.

$$\begin{aligned} I_{xx}\dot{p} + (I_{zz} - I_{yy})(q_0r + r_0q) - I_{xz}(\dot{r} + p_0q + q_0p) - l &= \hat{l} \\ I_{yy}\dot{q} + (I_{xx} - I_{zz})(p_0r + r_0p) + 2I_{xz}(r_0\dot{r} + p_0\dot{p}) - m &= \hat{m} \\ I_{zz}\dot{r} + (I_{yy} - I_{xx})(p_0q + q_0p) - I_{xz}(\dot{p} - q_0\dot{r} - r_0\dot{q}) - n &= \hat{n} \end{aligned} \quad (3.4-6)$$

In the above equations the torque perturbations due to jet firings (\hat{l} , \hat{m} , \hat{n}) are equal to (\hat{L} , \hat{M} , \hat{N}). This equality means that jet firings are being treated as perturbations to the system. This makes intuitive sense, since the jets are not normally needed to maintain equilibrium flight.

After linearization, the symmetric flight condition was chosen. Physically, symmetric flight implies that the Shuttle has no angular velocity, no sideslip velocity and its wings are level (zero roll angle). The significant implication for the rotational dynamics is the assumption of no angular velocity:

$$p_o = q_o = r_o = 0 \quad (3.4-7)$$

Applying this condition to the above linearized equations gives

$$\begin{aligned} I_{xx}\dot{p} - I_{xz}\dot{r} - l &= \hat{l} \\ I_{yy}\dot{q} - m &= \hat{m} \\ I_{zz}\dot{r} - I_{xz}\dot{p} - n &= \hat{n} \end{aligned} \quad (3.4-8)$$

The aerodynamic torque terms, l , m , n , are expanded into partial derivatives with respect to aerosurface deflection, vehicle attitude and vehicle rates. The system of equations is then normalized with respect to velocity and transformed to the stability axis frame.

The natural separation of the linearized lateral and longitudinal dynamics of the vehicle are exploited in simplifying the equations of motion. The longitudinal dynamics are combined into one equation. In this longitudinal equation, term by term comparisons are made and negligible terms removed. One set of terms removed involved the long period longitudinal mode, the so-called phugoid. Other terms neglected are specific to the vehicle properties and flight regime considered (Appendix B) due to the presence of the term on the left hand side of Equation 3.4-9. This term is small compared to other terms that appear throughout the equations.

$$\left(\frac{\bar{q}Sc}{V_r^2} \right) \ll 0.001 \quad (3.4-9)$$

The lateral equations of motion are combined and simplified in a manner similar to that of the longitudinal dynamics.

3.4.4 Simplified Aerodynamics Model

After all simplifications are made as discussed above, the Laplace transform is taken for implementation in SIMULINK. Three s-domain equations remain, one longitudinal and two lateral.

The longitudinal equation is:

$$(s^2 + 2\zeta_\alpha \omega_\alpha s + \omega_\alpha^2) \hat{\alpha} = K_{\delta_e} (\tau_{\delta_e} s + 1) \hat{\delta}_e + u_y \quad (3.4-10)$$

where:

$$\begin{aligned} \omega_\alpha^2 &\equiv -\left(\frac{\bar{q}Sc}{I_{yy}}\right) C_{M\alpha} \\ \zeta_\alpha &\equiv \frac{1}{2\omega_\alpha} \left(\frac{\bar{q}S}{V_T} \right) \left[\frac{C_D + C_{L\alpha}}{m} - \left(\frac{c^2}{2I_{yy}} \right) C_{Mq} \right] \\ K_{\delta_e} &\equiv \left(\frac{\bar{q}Sc}{I_{yy}} \right) C_{M\delta_e} \\ \tau_{\delta_e} &\equiv \left(\frac{I_{yy}}{mcV_T} \right) \left(\frac{C_{D\delta_e}}{C_{M\delta_e}} \sin \alpha_T - \frac{C_{L\delta_e}}{C_{M\delta_e}} \cos \alpha_T \right) \end{aligned} \quad (3.4-11)$$

The lateral sideslip dynamics are given by:

$$(s^2 + 2\zeta_\beta \omega_\beta s + \omega_\beta^2)\beta + K_\phi s \phi_s = K_{\beta_{\delta_r}} \hat{\delta}_r + K_{\beta_{\delta_a}} \hat{\delta}_a + u_x \sin(\alpha_T) - u_z \cos(\alpha_T) \quad (3.4-12)$$

where:

$$\begin{aligned} \omega_\beta^2 &\equiv \left(\frac{\bar{q}Sb}{I_{zz}} \right) C_{n_\beta} \\ \zeta_\beta &\equiv -\frac{1}{2\omega_\beta} \left(\frac{\bar{q}S}{mV_T} \right) \left[C_{y_\beta} + \left(\frac{mb^2}{2I_{zz}} \right) C_{I_\beta} \right] \\ K_\phi &\equiv \left(\frac{g}{V_T} \right) + \left(\frac{\bar{q}Sb^2}{2I_{zz}V_T} \right) C_{I_\phi} \\ K_{\beta_{\delta_r}} &\equiv -\left(\frac{\bar{q}Sb}{I_{zz}} \right) C_{n_{\delta_r}} \\ K_{\beta_{\delta_a}} &\equiv -\left(\frac{\bar{q}Sb}{I_{zz}} \right) C_{n_{\delta_a}} \end{aligned} \quad (3.4-13)$$

Lastly, the lateral bank dynamics are given by:

$$K_\beta \beta + (s + \frac{1}{\tau_\phi}) s \phi_s = K_{\phi_{\delta_r}} \hat{\delta}_r + K_{\phi_{\delta_a}} \hat{\delta}_a + u_x \cos(\alpha_T) + u_z \sin(\alpha_T) \quad (3.4-14)$$

where:

$$\begin{aligned} K_\beta &\equiv \left(\frac{\bar{q}Sb}{I_{xx}} \right) C_{l_\beta} \\ \frac{1}{\tau_\phi} &\equiv \left(\frac{g}{V_T} \right) \left[\sin \gamma_o - \left(\frac{I_{xz}}{I_{zz}} \sin \alpha_T \sin \theta_o - \frac{I_{xz}}{I_{xx}} \cos \alpha_T \cos \phi_o \right) \right] - \left(\frac{\bar{q}Sb^2}{2I_{xx}V_T} \right) C_{2_\phi} \\ K_{\phi_{\delta_r}} &\equiv \left(\frac{\bar{q}Sb}{I_{xx}} \right) C_{l_{\delta_r}} \\ K_{\phi_{\delta_a}} &\equiv \left(\frac{\bar{q}Sb}{I_{xx}} \right) C_{l_{\delta_a}} \end{aligned} \quad (3.4-15)$$

α_T = trim angle of attack (rad)
 γ = flight path angle
 \bar{q} = dynamic pressure (lb/ft^2)
 S = reference area (ft^2)
 c = reference chord (ft)
 b = wingspan (ft)
 V_T = trim velocity
 g = acceleration due to gravity
 m = orbiter mass (slugs)
 $\hat{\alpha} = \alpha - \alpha_T$ = perturbation from α_T (rad)

(3.4-16)

The control and stability derivatives encountered in equations (3.4-11) through (3.4-16) are non dimensional parameters that relate aerosurface deflections and vehicle properties to forces and torques in the body axis frame through the appropriate vehicle scaling parameters. For example, $C_M \delta_e$ relates elevator deflection to pitching moment through $(\bar{q} Sc)$

$$M_{\delta_e} = (\bar{q} Sc) C_{M \delta_e} \quad (3.4-17)$$

The control and stability derivatives are taken from multidimensional lookup tables in [Zacharias] where the derivatives are represented as functions of angle of attack and Mach number.

Because the equations were derived from an equilibrium condition, all inputs and angles are deviations from the equilibrium point. Note that the trim sideslip angle for all models is $\beta = 0^\circ$, so the perturbation is equal to the actual angle.

The above equations represent the linearized vehicle rotational dynamics for a given altitude, angle of attack, and Mach number. As these parameters change, so do the coefficients in the equations of motion. From the data in [OADB] and [Zacharias], eight models were created for flight conditions during a nominal reentry ranging from Mach 10 and 170 K ft to Mach 2 and 77 K ft. Table (3.4-1) summarizes the models developed.

Mach #	angle of attack (°)	altitude (10 ³ ft)
2	12.5	77
3	16.0	90
4	20.5	105
5	25.0	120
5.7	29.0	130
7.5	35.0	150
8.8	38.0	158
10	40.0	170

Table 3.4-1: Summary of Reentry Models

To aid in visualizing the dynamics, a block diagram of the simplified equations is provided in Figure (3.4-4).

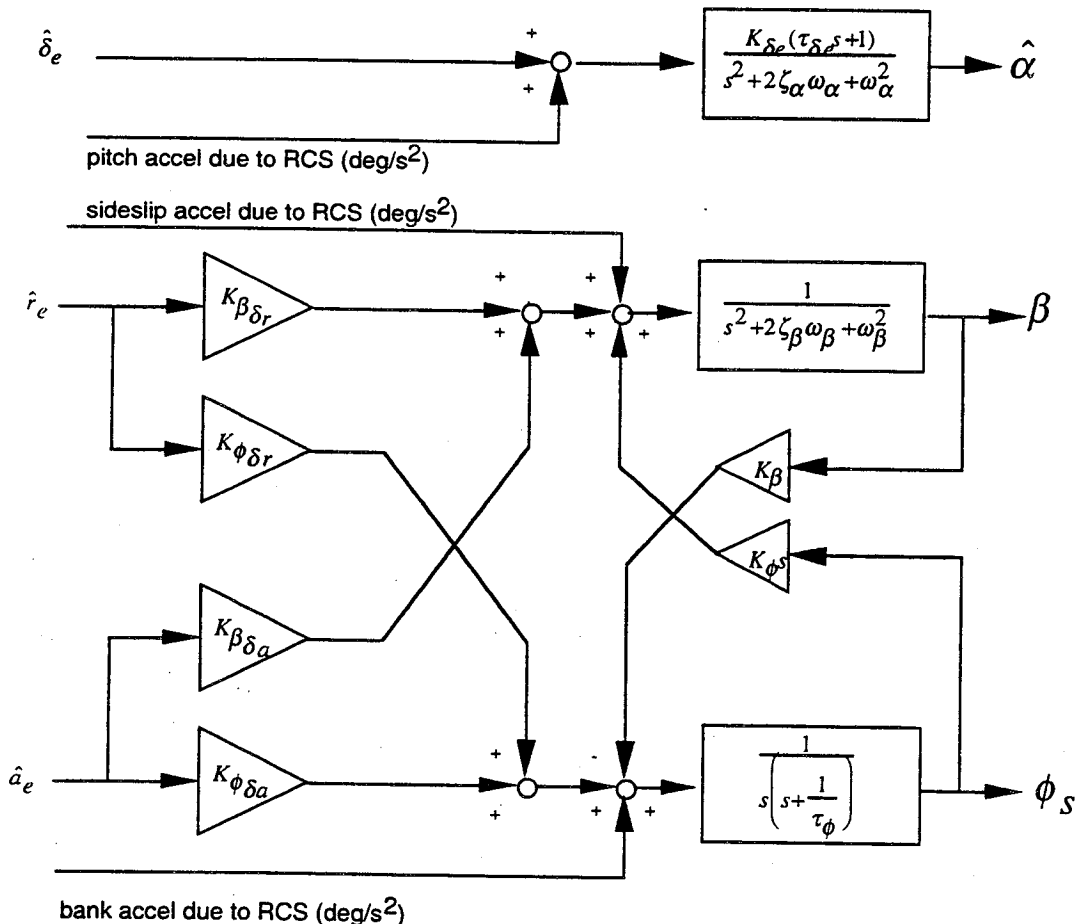


Figure 3.4-4: Block Diagram of Simplified Aerodynamic Model

3.5 Aerosurface Actuator Models

Aerosurface actuator models are developed for aileron, elevator and rudder control as required by the rotational dynamics model described in Section 3.4. These surfaces are implemented with the rate and deflection limits described in Section 2.2. No models are provided for the speedbrake and bodyflap since they are not used for active rotational control in a trim condition. Imbalances due to a shifted center of gravity location are trimmed using the bodyflap [OADB]. By using the bodyflap, the burden of correcting for an off nominal center of gravity is removed from the elevons. Once the vehicle is trimmed for a flight condition, the bodyflap does not move until a new flight condition is encountered. The bodyflap deflection is assumed to be constant here, since all models in this study represent a single trim flight condition.

The speedbrake helps to provide additional lateral stability and drag modulation. During reentry the speedbrake deflection is typically Mach scheduled [OADB]. For a given trim flight condition the speedbrake deflection does not change.

In addition to aerosurface limits described in Section 2.2 simple dynamics and high frequency noise were added to the aerosurface models in the simulation. Second order dynamics were modeled for both the elevons and the rudder. These models are taken from [Doyle 86]. The elevon dynamics have the following natural frequency and damping ratio:

$$\begin{aligned}\omega &= 14 \text{ rad/s} \\ \zeta &= 0.72\end{aligned}\tag{3.5-1}$$

Similarly the rudder dynamics are described by:

$$\begin{aligned}\omega &= 21 \text{ rad/s} \\ \zeta &= 0.75\end{aligned}\tag{3.5-2}$$

A typical elevon step response is illustrated in Figure (3.5-1).

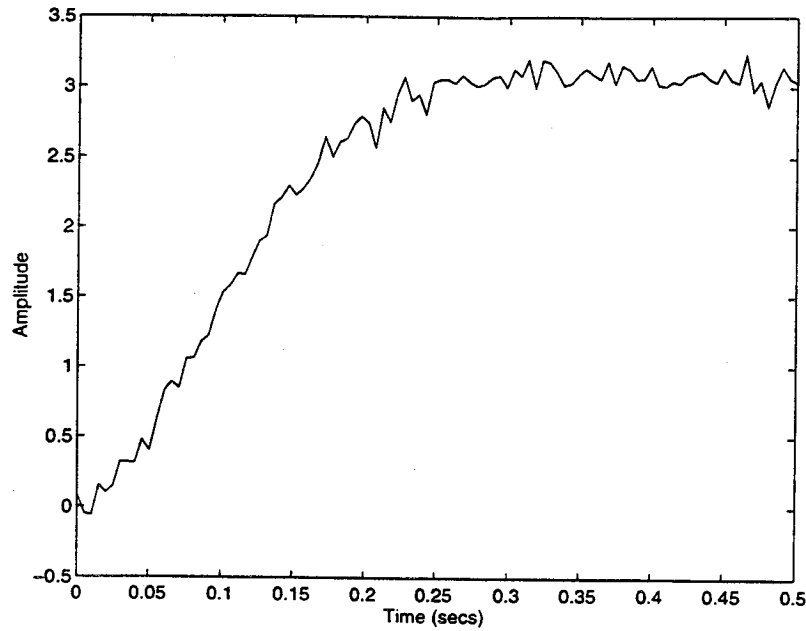


Figure 3.5-1: Modeled Elevon Step Response Including High Frequency Noise

3.6 RCS Effector Models

Four factors alter the effect of jet firings during reentry: plume interaction with the aerodynamic flow field, plume self-impingement, the increase in atmospheric pressure, and thruster valve on/off transients.

$$M_{rcs} = M_{int} + M_{imp} + K_{alt}M_{jet} + M_{trans} \quad (3.6-1)$$

3.6.1 Plume Interaction

The most significant deviation from nominal thrust during reentry is due to the plume interaction effects with the aerodynamic flow field. For the aft jets, the effect may be so large that the net resulting moment opposes the nominal moment expected from the vacuum thrust alone [OADB]. During reentry the jets are firing into the vehicle slipstream and affect the pressure field surrounding the vehicle. The net force and moment produced by a jet firing becomes a function of: jet firing direction (up, down, right, or left), angle of attack, elevon and body flap deflection, and the momentum ratio.

$$M_{int} = f\left(\frac{\phi_j}{\phi_\infty}, n_{(Jet\ Type)}, \alpha, \delta_e, \delta_{bf}\right) \quad (3.6-2)$$

The momentum ratio is defined as:

$$\frac{\phi_j}{\phi_\infty} = 0.1543 \frac{n_{(Jet\ Type)}}{q}$$

$n_{(Jet\ Type)} = \# \text{ of jets firing in same direction}$ (3.6-3)

It describes the relative magnitude of the momentum of jet flow to the momentum of the freestream.

The analytical model for the flow field interaction torque and moment was determined empirically. An orbiter model was suspended in a wind tunnel and high pressure air was forced through ports in the jet locations. The net effect of the jets firing into the flow field was determined using the following relation.

$$M_{int} = (C_{mRCS\ on} - C_{mRCS\ off}) \bar{q} Sc - M_{imp} \quad (3.6-4)$$

In Eq. (3.6-4) all aerodynamic effects of firing the jets are lumped into the jet interaction term.

The data is in the form of several multidimensional tables in [OADB]. The independent variables combine to form a non-dimensional coefficient which is then scaled by the appropriate quantities to yield torque. The lookup tables have been mechanized for use in the thesis simulation model.

$$M_{int} = \bar{q} S \begin{bmatrix} c & 0 \\ b & c \\ 0 & c \end{bmatrix} (\Delta C + \Delta C_{bf} + \Delta C_e) \quad (3.6-5)$$

The jet interaction torques are quite significant and have a large uncertainty associated with them. Note that for pitch firings (an equal number of up or down jets firing simultaneously on both sides), the interaction terms cancel since plume interaction torques for these symmetric firings are very nearly equal and opposite.

3.6.2 Impingement

Jet self-impingement moments occur when jet plumes deflect off the orbiter body or aerosurfaces. These moments are small for the forward RCS, but are significant for the rear pods, especially the down firing jets.

Jet impingement terms are not included in the reentry model. These terms are neglected because the effect is well known and their inclusion does not contribute significant additional uncertainty to the problem [FAD-26]. Furthermore, the jets most utilized are the side firing jets for yaw control which have the smallest impingement effect.

Figures (3.6-1), (3.6-2), and (3.6-3) illustrate the magnitude of the impingement and plume interaction accelerations relative to those produced by jet firings in a vacuum. The interaction and impingement terms were derived using the flight condition at Mach 10; angle of attack 40°, this flight condition gives the worst case interaction terms because it has the largest momentum ratio.

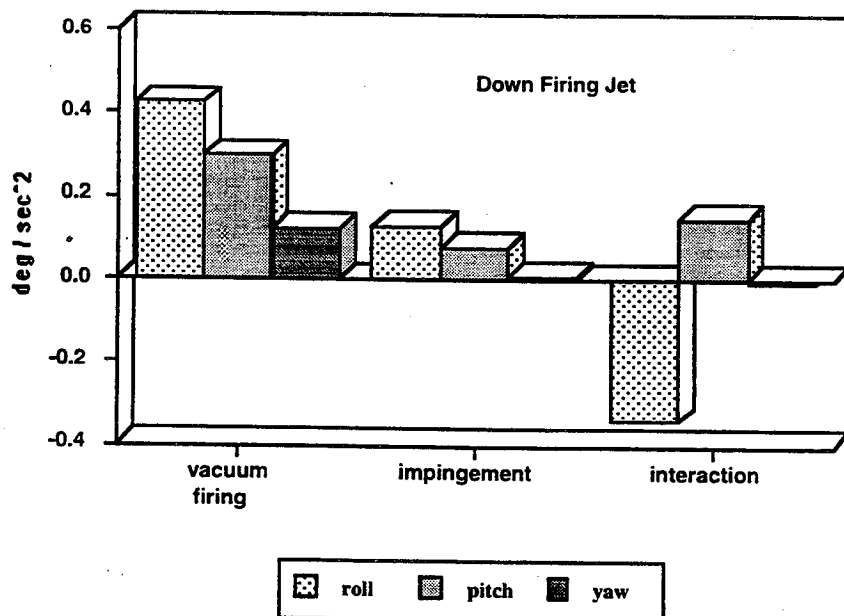


Figure 3.6-1: Angular Acceleration Comparison for Down Firing Jets

The impingement terms are most significant for the down firing jets and least significant for the side firing jets. Also note that the roll acceleration

induced by the plume interaction for the side and down firing jets produces a roll torque in the opposite direction of the vacuum jet torque.

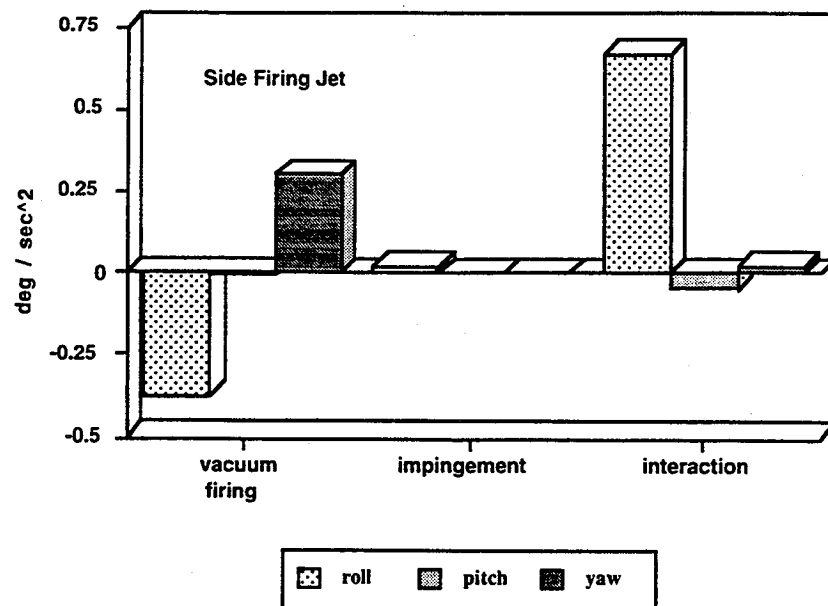


Figure 3.6-2: Angular Acceleration Comparison for Side Firing Jets

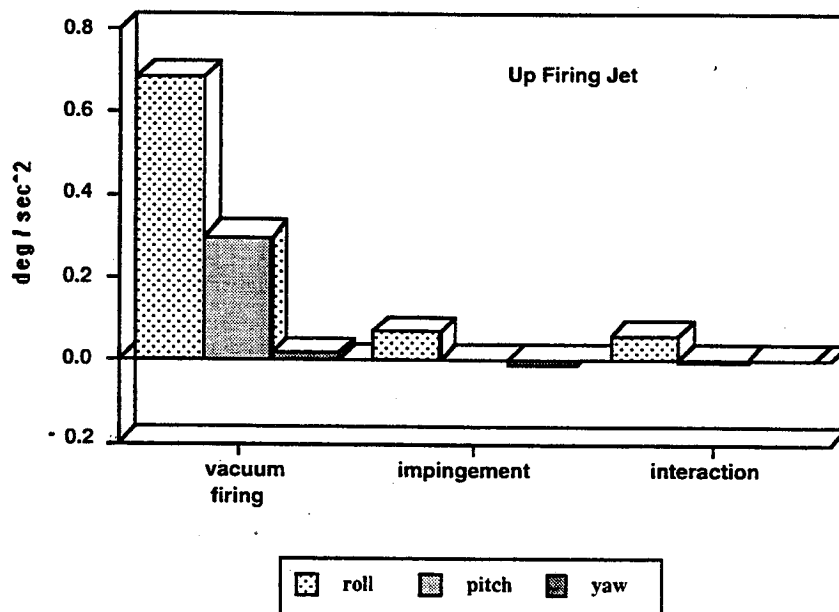


Figure 3.6-3: Angular Acceleration Comparison for Up Firing Jets

3.6.3 Increased Atmospheric Pressure

Increasing atmospheric pressure reduces the effective thrust by limiting the amount of expansion in the jet nozzles. This effect is described by Equation (3.6-2) from [Paradiso] that was fit to NASA data in [OADB].

$$K_{alt} = 1 - e^{-h/26,000} \quad (h < 30,000 \text{ ft})$$
$$K_{alt} = 0.64 \quad (\text{otherwise}) \quad (3.6-2)$$

The Figure (3.6-4) shows the above equations as a function of altitude.

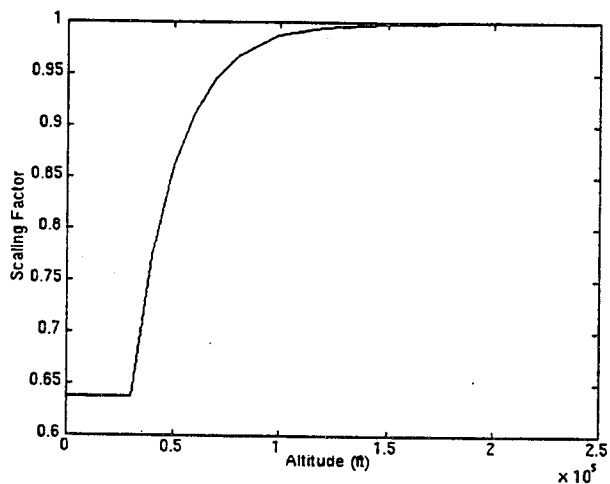


Figure 3.6-4: Altitude Scaling Factor

3.6.4 Transient Effects

Several factors contribute to delay and ramp up effects evident in the thrust time response. Significant delays are caused by the Shuttle software. Other delays arise from the time it takes for valves to open and close and the time for propellants to meet and combust. The rise time is approximately twenty milliseconds. The standard for scaling transient effects of the thrusters is chamber pressure data [OADB]. Figure (3.6-5) shows a typical chamber pressure profile.

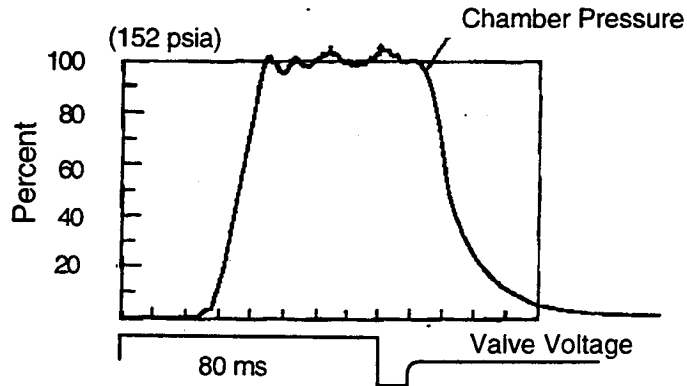


Figure 3.6-5: Primary Thruster Chamber Pressure, Typical 80 ms pulse

The shortest firing command that may be issued by the digital autopilot is 80 ms. A second order transfer function accounts for the transient portion of the thrust time response. This transfer function has the following natural frequency and damping ratio.

$$\begin{aligned}\omega &= 200 \text{ rad/s} \\ \zeta &= 0.9\end{aligned}\tag{3.6-6}$$

Figure (3.6-6) illustrates the response of the second order transfer function to a 80 ms. pulse. Note that the initial transport delay at the beginning of the chamber pressure profile is being ignored as it is well known and does not contribute additional uncertainty or dynamically affect the problem.

3.7 Sensor Models

In the closed loop simulation, the different rate gyros were modeled as quantizers with the appropriate quantum level selected based on the standard deviation of the individual sensor. The size of the quantum level is calculated based on a uniform probability distribution and is given by,

$$\text{Quantum Level} = \sqrt{12}[\sigma_{\text{sens}}] \tag{3.7-1}$$

No other nonlinearities of the rate measuring devices were included as the discretization level is the dominant factor in determining the measurement noise introduced by a particular sensor.

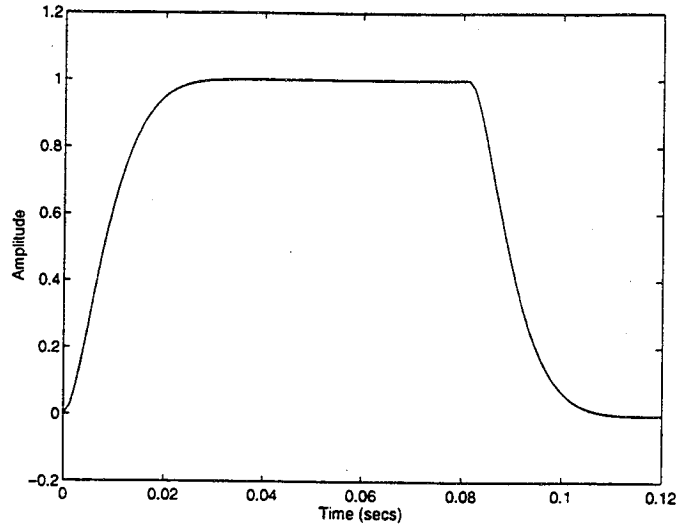


Figure 3.6-6: Time Response of Thrust Model to 80 ms Pulse

3.8 Example Maneuvers

Guidance command inputs to the simulation consist of angle of attack and bank angle commands. Specifically, two different commands are used to simulate typical maneuvers. The dynamical response of all the models in closed loop simulations to these commands is similar. For illustrative purposes each of the commands is shown at Mach 5.7 in Figures (3.8-1) and (3.8-2).

The first simulates a 40° commanded change in bank angle. A command of this nature is used in turning the Shuttle as well as for descent rate control. Early in reentry, descent rate is controlled by the bank angle since the angle of attack is driven by thermal constraints. By conducting a series of roll reversals in a fixed corridor, the Shuttle is able to control its descent rate and still maintain an appropriate ground track. Later in reentry, banks are used as in a conventional aircraft for turning. This command exploits the lateral dynamics of the Shuttle and primarily relies on aileron and yaw jets for command completion. At lower angles of attack, rudder assists in yaw control.

The other maneuver simulates a 3° decrease in angle of attack. Angle of attack is scheduled during reentry, progressively decreasing from 40° at entry interface to the landing angle of attack of 7.5° . This command is achieved primarily by using elevator control. At the flight conditions simulated in this study, RCS jets would not normally be used in the execution of this command.

However, since it is a goal of the study to monitor the performance of the jets, the control algorithms have been modified to allow the RCS jets to assist the elevator in completing the change in angle of attack. Augmented RCS pitch control at these lower altitudes and higher dynamic pressures is a possibility especially in the event of an elevon failure.

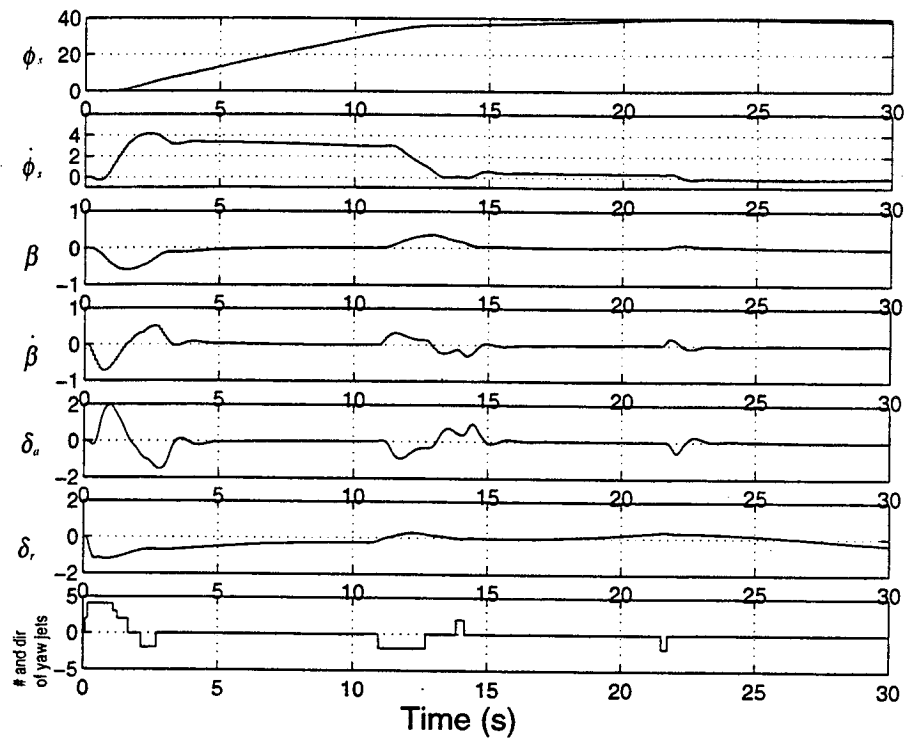


Figure 3.8-1: Response to 40° Bank Command

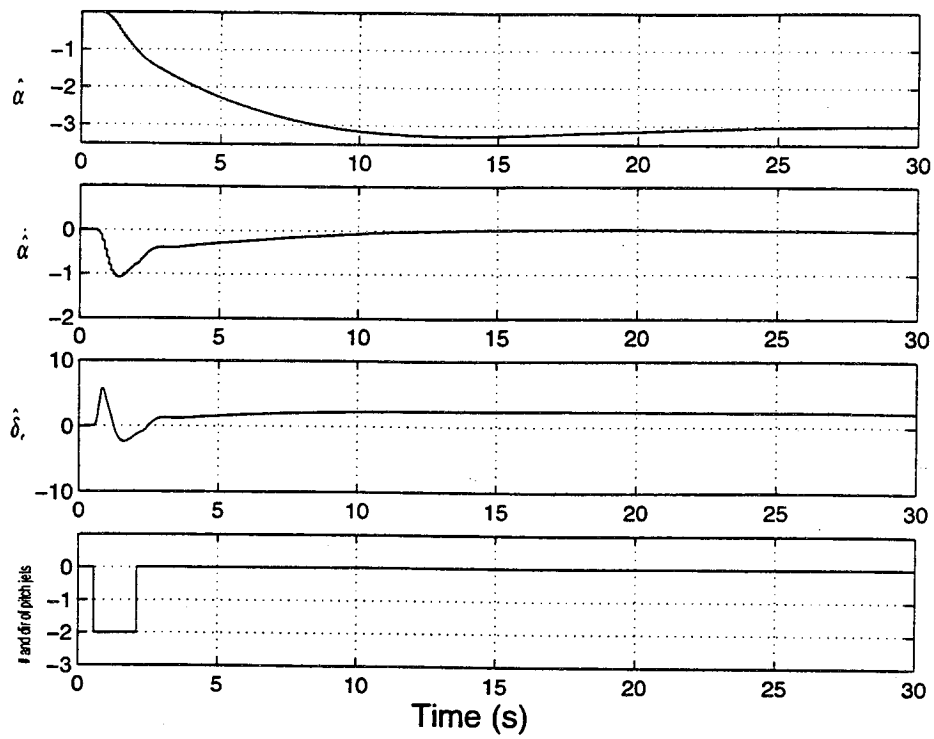


Figure 3.8-2: Response to $3^\circ \alpha$ Command

4.0 Kalman Filter Based VHM Estimator Theory and Design

The overall VHM structure from Chapter 1 is shown in Figure (4.0-1).

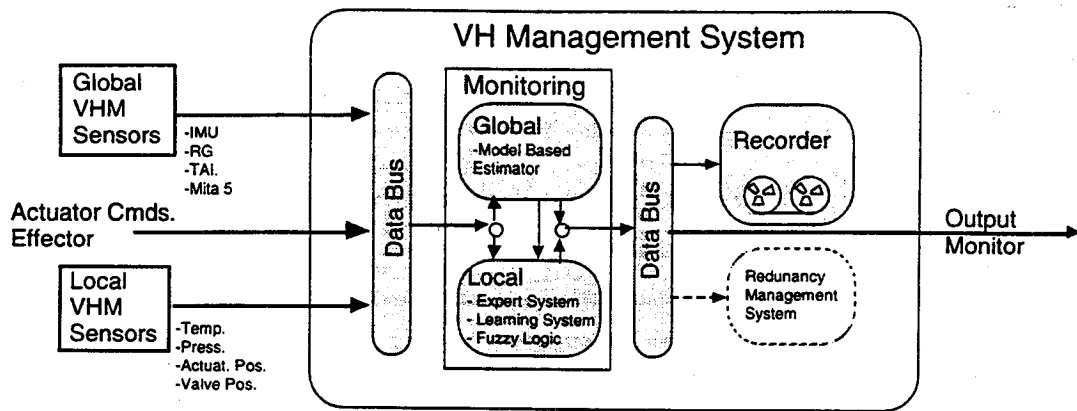


Figure 4.0-1: Overview of VHM System

The goal of VHM is to characterize the performance of a system based on a variety of measurements. The global monitor in VHM, processes information on a general, system wide level. The global monitor sends its evaluation of system condition to the local monitor and an output data bus that transports the information. From the data bus, the information may be saved for later analysis, output for real time display, or shared with other vehicle systems like redundancy management.

The accuracy of the system characterization is largely influenced by three factors: the original uncertainty, the precision of the sensor data, and the rate of measurements provided to the monitor. These three factors determine the accuracy of the estimate. As time progresses, more information is made available to the monitor through the sensor measurements, and the estimation error approaches some minimum value. For a given estimation time, there is an associated estimation error, the shorter the time the greater the error. Figure (4.0-2) qualitatively illustrates the relationship between sensor precision, measurement data rate, and estimation error.

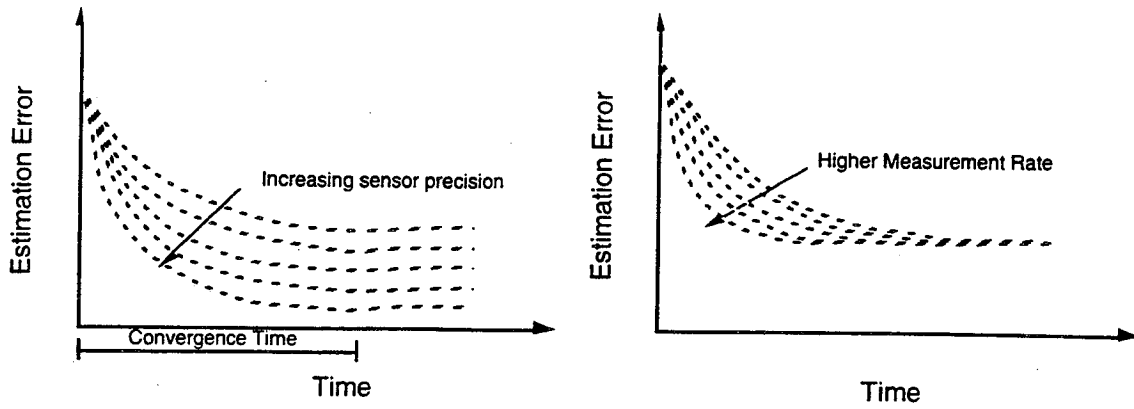


Figure 4.0-2: Qualitative Relationships of Sensor Precision, Measurement Rate and Error

Convergence time for this general discussion is defined as the estimation time required to achieve the minimum error. As seen in Figure (4.0-2), the maximum achievable estimation accuracy (minimum error) improves with the precision of the sensor. Also, the convergence time improves with both sensor quality and increased measurement rate. The drawback of having a very precise sensor operating at a fast measurement rate is the expense of high precision sensors and the associated hardware to process high rate data. For a given system and its associated uncertainties, the sensor precision and data rate drive the maximum accuracy and convergence time.

For the Shuttle RCS, the goal of the global monitor is to estimate jet thrust based on effector commands, and measurements of the vehicle's dynamic response. This estimation is to be done such that the estimation error is minimized for a maximum number of firings. The time available to estimate the force of a firing is limited by the spacing between firings. For example, if the jets only fired once every 10 seconds, then 10 seconds would be available to estimate the force of each firing. Figure (4.0-3) shows how convergence time and the average estimation error over a mission are qualitatively related. If the convergence time is longer than the spacing between firings, the error associated with those firings will be greater than the minimum achievable error.

Unfortunately, there is no practical way to predict the spacing between firings for an entire mission. The fastest a jet can fire back to back is two cycles of the flight control software or 160 ms (80 ms on, 80 ms off, then fire again). To minimize the average error over a mission, the desired convergence time should be less than the minimum spacing between firings, if possible and practical. However, satisfactory information will likely be obtained over the duration of

the mission even if the convergence time is 10 times the minimum Shuttle on-time.

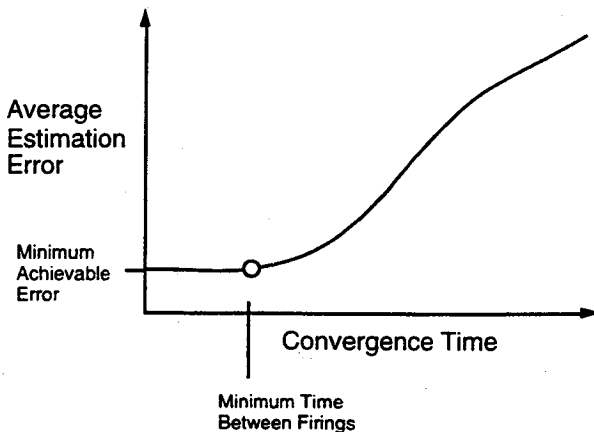


Figure 4.0-3: Relationship of Convergence Time and Mission Average Thrust Estimation Error

Taking the above tradeoffs into account, the VHM estimator for the Shuttle RCS example will be evaluated and designed with the following objectives:

- Track the thrust produced by the most recent firing of each jet
- Estimate thrust to within $\pm 10\%$ of nominal (87 lb) for a minimum impulse firing
- Record data for each firing over entire mission:
 - Jet number
 - Time of firing
 - Thrust estimate
 - Error covariance associated with estimate
- Provide thrust estimates that are robust to:
 - Unmodeled nonlinearities or model parameter uncertainty
 - Measurement noise
 - Environmental disturbances

A linear, discrete-time, time-varying Kalman filter was chosen for the initial design because it is the standard in estimation, will provide a useful benchmark, and provides reasonable computational efficiency. A discrete-time filter was chosen to monitor the RCS because of its functionality and ease of implementation. A time-varying formulation makes it possible to change filter

parameters as the state of the system changes. For example, when a jet is firing, additional process noise can be added to account for the uncertainty in the thrust, which is not present when the jet is off. The time varying formulation also allows the force estimates themselves to be states, since the transition matrix can be altered with every time step. Finally, a discrete-time representation allows the filter to be designed and tested at the rate it would be executed on a digital computer and allows examination of sampling rate effects on system performance.

The Kalman filter based estimator is the engine for providing the data to the VHM system. The filter estimates the thrust from the last firing of each of the jets. When the jet fires again, the estimate and associated error are recorded before the information for that jet firing is lost. As the flight progresses, and the jets are fired a number of times, a table will develop for each jet. The table will contain the following information: firing time, an estimate of the thrust, and the error associated with the estimate. From post flight examination of these tables, the performance history of the RCS may be developed for the flight. It is hoped that the real time recording of thrust estimates will help to illuminate the causes and effects of transient thruster problems like helium ingestion, as well as track problems that indicate a persistent degradation in performance.

In Section 4.1, background and development of the Kalman filter is given. Section 4.2 describes the representation of the Shuttle vehicle dynamics and RCS systems used for the Kalman filter design. Section 4.3 presents a Kalman filter based estimator and its envisioned integration into the overall VHM scheme.

4.1 Kalman Filter Development and Background

In this section, the recursive Kalman filter equations are derived. At the most basic level, the discrete Kalman filter is a recursive algorithm for processing measurements and their statistical parameter characteristic errors. However, for random systems with Gaussian initial conditions and process noises, the Kalman filter is the optimal estimator by most reasonable criteria of optimality including, maximum likelihood, minimum variance, and least squares. The Kalman filter produces these optimal estimates by utilizing a state space model of the system dynamics and its uncertainty properties.

First, it is assumed that the system to be estimated is a random process that can be modeled in the form,

$$\begin{aligned} x_{k+1} &= \phi_k x_k + w_k \\ E[w_k] &= 0 \\ E[w_k w_j] &= \begin{cases} Q_k & j = k \\ 0 & j \neq k \end{cases} \end{aligned} \quad (4.1-1)$$

where, x_k is the system state vector and w_k is a zero mean white sequence with covariance Q_k .

Observation of the system (measurements) occurs at discrete points in time and is a linear combination of the states corrupted by measurement noise uncorrelated with the process noise,

$$\begin{aligned} z_k &= H_k x_k + v_k \\ E[v_k] &= 0 \\ E[v_k v_j] &= \begin{cases} R_k & j = k \\ 0 & j \neq k \end{cases} \end{aligned} \quad (4.1-2)$$

where, H_k is the measurement matrix and v_k is a zero mean white sequence with covariance R_k .

It is assumed that there is some initial estimate of the state vector, \hat{x}_k . Now the state estimation error, e_k^- , is given by

$$e_k^- = x_k - \hat{x}_k^- \quad (4.1-3)$$

The "super minus" indicates values before the incorporation of a measurement. The carat, or hat symbol, denotes the estimate. This notation follows throughout the thesis.

The associated error covariance matrix is then given by,

$$P_k^- = E[e_k^- e_k^{-T}] = E[(x_k - \hat{x}_k^-)(x_k - \hat{x}_k^-)^T] \quad (4.1-4)$$

Note that for the expression in Equation (4.1-4) to be a covariance matrix, the mean of the estimation error is assumed to be zero.

Now, the structure for incorporating the noisy measurements, z_k , to improve the prior estimate is assumed to have the following linear relationship,

$$\hat{x}_k = \hat{x}_k^- + K_k (z_k - H_k \hat{x}_k^-) \quad (4.1.5)$$

where \hat{x}_k is the updated estimate and K_k is the yet to be determined Kalman gain matrix that gives the optimal estimate. Here, the criterion of optimality is the minimum mean squared error. To find this optimal gain, the expression for the covariance matrix associated with the updated estimate is developed,

$$P_k = E[e_k e_k^T] = E[(x_k - \hat{x}_k)(x_k - \hat{x}_k)^T] \quad (4.1.6)$$

Substituting Equation (4.1-2) into Equation (4.1-5) and substituting the result into Equation (4.1-6) gives,

$$P_k = E\{[(x_k - \hat{x}_k^-) - K_k (H_k x_k + v_k - H_k \hat{x}_k^-)] [(x_k - \hat{x}_k^-) - K_k (H_k x_k + v_k - H_k \hat{x}_k^-)]^T \} \quad (4.1.7)$$

Performing the expectation operation and observing that $(x_k - \hat{x}_k^-)$ is uncorrelated with the measurement error, v_k , the updated covariance matrix becomes,

$$P_k = (I - K_k H_k) P_k^- (I - K_k H_k)^T + K_k R_k K_k^T \quad (4.1.8)$$

Rewriting Equation (4.1-8) and temporarily dropping the k subscript gives,

$$P = P^- - K H P^- - P^- H^T K^T + K (H P^- H^T + R) K^T \quad (4.1.9)$$

The error covariance matrix is now in the form of a quadratic in K . To find the optimal K , the matrix derivative of the trace of P is taken with respect to K and set equal to zero. The derivative of the trace is used because the trace of P

represents the sum of the individual error covariances of the states. By minimizing this sum, the *length* of the error vector is minimized. After taking the derivative the following expression results,

$$\frac{d(\text{trace}P)}{dK} = -2(HP^-)^T + 2K(HP^-H^T + R) \quad (4.1-10)$$

Setting Equation (4.1-10) to zero and solving for K yields,

$$K_k = P_k^- H_k^T (H_k P_k^- H_k^T + R_k)^{-1} \quad (4.1-11)$$

Equation (4.1-11) gives the expression for the gain that minimizes the trace of P_k . By substituting the expression for the optimal gain, Equation (4.1-11), into Equation (4.1-9) a simpler expression for the updated P_k is,

$$P_k = (I - K_k H_k) P_k^- \quad (4.1-12)$$

After being updated with a measurement, the state estimate and its error covariance matrix are propagated to the next discrete step. To propagate the state estimate, it is multiplied by the state transition matrix. The contribution of w_k is ignored because it is zero mean and uncorrelated with all other w 's.

$$\hat{x}_{k+1}^- = \phi_k \hat{x}_k \quad (4.1-13)$$

To derive the propagation for the covariance matrix, the expression for the a priori error is formed

$$\begin{aligned} e_{k+1}^- &= x_{k+1} - \hat{x}_{k+1}^- \\ &= (\phi_k x_k + w_k) - \phi_k \hat{x}_k \\ &= \phi_k e_k + w_k \end{aligned} \quad (4.1-14)$$

Noting that w_k and e_k are uncorrelated, because w_k is the process noise for the discrete step $k+1$, the expression for the propagation of P_k to P_{k+1}^- , is given by,

$$\begin{aligned}
P_{k+1}^- &= E[e_{k+1}^- e_{k+1}^{-T}] = E[(\phi_k e_k + w_k)(\phi_k e_k + w_k)^T] \\
&= \phi_k P_k \phi_k^T + Q_k
\end{aligned} \tag{4.1-15}$$

Equations (4.1-5), (4.1-11), (4.1-12), (4.1-13) and (4.1-15) make up the Kalman filter recursive equations. Starting with an initial estimate and covariance, the equations first update the previous state estimate and its associated error covariance matrix, then propagate these to the next discrete interval where the next measurement may be incorporated. Figure (4.1-1) illustrates the use of these recursive equations.

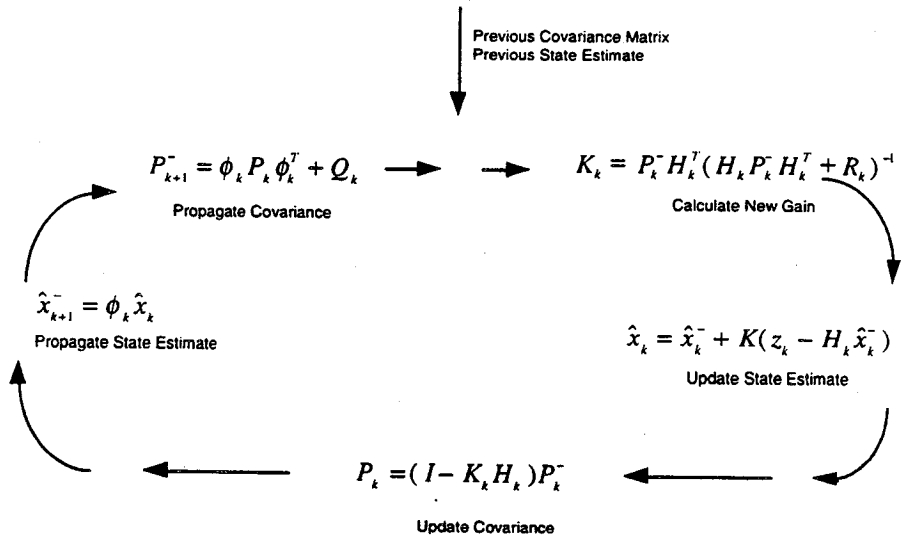


Figure 4.1-1: Kalman Filter Recursive Loop

4.2 Model Formulation for Linear Estimation

4.2.1 Filter State Space Structure

The filter was designed to estimate the force produced by each jet firing and contains a linear model of the rigid body reentry rotational dynamics described in Chapter 3. Using this dynamics model, the filter estimates the jet thrust produced by each jet firing. As deterministic inputs, the model has jet commands (which jets and time on and off) and aerosurface deflections. Jet plume interaction accelerations are fed forward into the filter. The state space representation of the vehicle dynamics assumed for the filter design is

$$\begin{aligned} x_{k+1} &= \phi_k x_k + \Lambda_k u_k + G_k w_k + \omega_{\text{plume}_k} \\ z_{k+1} &= H_k x_k + v_k \end{aligned} \quad (4.2-1)$$

where, x is the filter state vector, u is the aerosurface control input, w is the process noise, z is the measurement (angular body rates) vector, ω_{plume} is the plume interaction term, and v is the measurement noise. The process and measurement noise are assumed to be uncorrelated white noise.

The filter states include attitudes, rates, jet force for each jet individually and jet force for multiple yaw jet firings (for example only in this thesis). Equation (4.2-2) shows the filter state vector.

$$x = \begin{bmatrix} \phi \\ \alpha \\ \beta \\ \dot{\phi} \\ \dot{\alpha} \\ \dot{\beta} \\ F_1 \\ F_2 \\ \downarrow \\ F_{20} \\ F_{\text{mult}} \end{bmatrix} \quad (4.2-2)$$

The first three states are the attitudes in the stability axis frame: bank angle, angle of attack, and sideslip. Similarly, the next three states are the rates in the stability axis frame.

The next twenty states represent the force estimate of the thrust produced during the last firing of each jet, one state for each of the jets used during reentry. It is important to note, that these states do not represent the current force being applied to the vehicle, rather, they represent the thrust force of the most recent firing that occurred. After a firing is complete, the filter still estimates the force of the firing, not the external force applied to the vehicle when the jet is off. This state definition was chosen to allow more rate measurements to be incorporated into the thrust estimate for each firing. The additional measurements are especially important for providing acceptable estimates of minimum impulse firings as discussed earlier.

Multiple jets, firing together in the same direction from a common pod, produce nearly identical responses in vehicle dynamics. If the individual states corresponding to the jets firing are used to estimate force independently, the estimate is poor. The result is unsuitable because the filter is not able to distinguish how much force is being produced by each jet individually. A filter constructed in this manner has large error covariances associated with the thrust estimates of the jets that were fired simultaneously, and consequently will falsely indicate poor thrust estimates.

During reentry, multiple yaw jets from the same pod are often fired simultaneously. Consequently, the last state has been added to represent the combined thrust of these jets. When jets are fired simultaneously in the same direction, the VHM filter uses the average position of the jets firing and estimates the total force being produced. Note that multiple up and down firing jets on the same pod may also fire at the same time for pitch and roll control, but these states are not modeled for this thesis demonstration. Only one multiple jet state is incorporated to illustrate the treatment of multiple jets firing simultaneously in the same direction from the same pod.

The discrete-time filter transition matrix is organized as shown in Equation (4.2-3)

$$\Phi_{\text{all on}} = \begin{bmatrix} \Phi_{\text{dynamics}} & \Delta\omega_{\text{jet}\#1} & \dots & \Delta\omega_{\text{jet}\#20} & \Delta\omega_{\text{jet(mult)}} \\ \hline 6 \times 6 & 1 & & & 0 \\ \hline 0 & & \dots & & 0 \\ \hline & 20 \times 20 & & 1 & \\ \hline 0 & & & & 1 \times 1 \end{bmatrix} \quad (4.2-3)$$

In the upper left corner is the transition matrix for the vehicle dynamics model, a discrete time representation of the dynamics discussed by Equations (3.4-10) through (3.4-16). The block to the right of the vehicle dynamics, are the

contributions of the individual jets to the change in the rate and attitude for a given time step. Each of these columns is a vector constant that maps jet force magnitude for a particular jet into a change in vehicle state (Appendix A). This relationship is based on jet location, vehicle mass properties (Appendix B), and thrust direction.

At the start of each filter pass, the transition matrix is set assuming all jets are ON. Using the jet command, the filter places zeros in the columns of the jets that are OFF. If a jet is ON, the column is left unchanged. In the algorithm, this is accomplished by using a vector, C , of 1's and 0's. The first six elements of this vector are 1 since the vehicle attitudes and rates are always included. The next twenty-one elements are 1 for jets that are ON and 0 for those that are OFF. Equation (4.2-4) shows this mathematically,

$$\Phi_k = CC^T \Phi_{\text{all on}} + \text{diag}(\bar{C}) \quad (4.2-4)$$

where, C is the "on or off" vector, and $\text{diag}(\bar{C})$ is a diagonal matrix with the logical complement of C as the main diagonal. The addition of the $\text{diag}(\bar{C})$ term ensures that all elements on the main diagonal of the transition matrix, except the first six, are identically equal to one. If multiple yaw jets are firing, then the multiple yaw element is set to 1 and the terms corresponding to the individual yaw jets are set to 0.

4.2.2 Process Noise

The estimator will employ a simple linear model of the vehicle dynamics thereby neglecting nonlinearities and environmental disturbances. The addition of process noise accounts for some of these unmodeled terms. For the RCS problem, these unmodeled factors include: jet thrust uncertainty, aerosurface position uncertainty, and magnitude of Euler coupling accelerations. Modeling and jet plume interaction uncertainties are not included in the process noise for the Kalman filter because they are large and would severely degrade the estimate. The effect of neglecting these terms is examined in Chapter 5.

The force produced by each jet firing in the steady state varies by $\pm 3\%$, corresponding to an error of approximately 26.1 lb [SODB]. This uncertainty in jet thrust is reflected in the process noise when a jet is firing. When jets are firing,

process noise with a magnitude of 26.1 lb thrust is added to the jet state corresponding to the jets that are firing. When a given jet is off, no process noise acts on the jet state because the force produced by a jet is nominally zero.

To account for aerosurface position uncertainty, the effect of having a small unknown error in the position was determined by multiplying the input matrix, Λ , by a small deflection in each of the aerosurfaces. The aerosurface deflections were assumed to be known to within $\frac{1}{20}$.

When the equations of motion are linearized, the nonlinear gyroscopic coupling term $\omega \times I\omega$ is eliminated. To account for these terms not being in the linear filter model the maximum anticipated rates allowed by the entry flight control during reentry ($3^\circ/\text{s}$) were used to calculate the Euler accelerations. The maximum Euler coupling body accelerations for the vehicle properties described in Appendix B are shown in Figure (4.2-2).

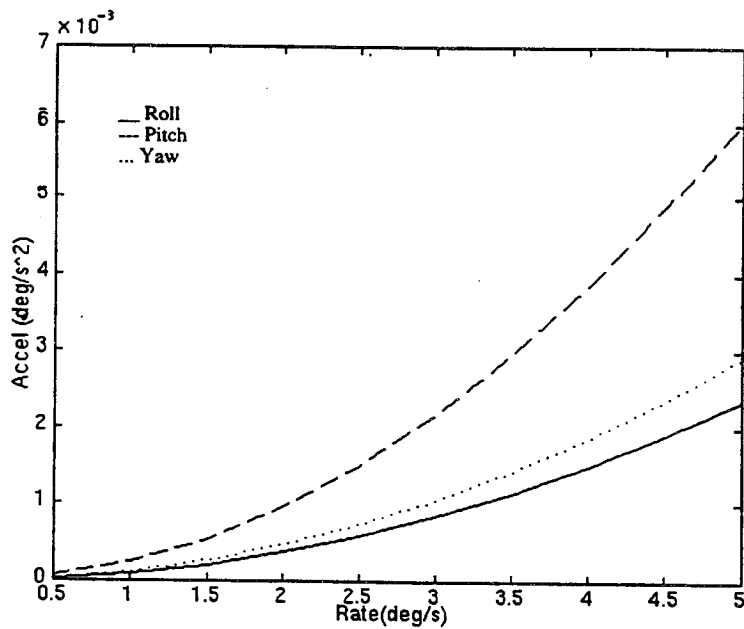


Figure 4.2-2: Angular Acceleration due to Euler Coupling

The root mean square of the aerosurface and Euler coupling torques act on the rate states. The jet uncertainty acts on any jet state that is currently firing. Equation (4.2-5) shows the structure of the matrix multiplying the process noise, G_k ,

$$G_k = \begin{bmatrix} 0 & & & & & \\ \vdots & \ddots & & & & \\ & \sigma_\phi & & & & \\ & & \sigma_\theta & & & \\ & & & \sigma_\psi & & \\ & & & & \sigma_{jet1} & \\ & & & & & \dots \\ & & & & & \sigma_{jet20} \\ & & & & & \\ & & & & 21 \times 21 & \\ & & & & & \sigma_{jet(mult)} \end{bmatrix} \quad (4.2-5)$$

where, $\sigma_{jet\#}$, represents the one sigma value of the intensity of the noise on the jet states.

4.2.3 Measurement Noise

The most significant factor in determining the measurement noise is the quantization level of the sensor. This level is the finest resolution of rate that can be measured and is driven by analog to digital conversion. In some instruments, this conversion is from a pure analog signal to a discrete representation. In this type of conversion, the smallest discrete interval is a function of the size of the computer word representing the digital measurement. In others, for example the Three Axis Instrument (TAI), the quantization comes from a pulse generator driving a motor counterbalancing the gimbal torques, here, it is the pulse rate that is the limiting factor in the quantization.

Some typical measurement noise levels for sensors that could be used to provide rate measurements for a VHM system are discussed below. The most obvious choice of sensors for a Shuttle application is those already onboard the Shuttle. These include the Rate Gyros(RG) and the Inertial Measurement Units (IMU). Two other rate gyro packages were also considered, the Navy Mita-5 and the Draper TAI. A measurement noise value was assigned to each of the gyro packages. The values in Table (4.2-1) are used for one standard deviation of measurement noise in units of $(^{\circ}/s)$ and are based on a range of $0(^{\circ}/s)$ to $10(^{\circ}/s)$ for Shuttle. These values are used to set the quantization level described in Section 3.7.

Sensor	σ (°/s)
IMU	0.00707
STS RG	0.08
TAI	0.05
TAI2	8.333e-5
Mita-5	0.005

Table 4.2-1 Rate Sensors and Measurement Noise

Note that two values are provided for the TAI, the second value listed (TAI2) includes additional electronics that provides greater precision.

4.3 Implementation of Kalman Filter for Thrust Estimation

The Kalman filter equations developed in Section 4.1 have been slightly modified to include terms pertinent to estimating the thrust produced by the thrusters. At the beginning of each time step the following are input to the algorithm: the jet command, the measurement vector and the error covariance from the previous time step.

First, the proper transition matrix is determined as outlined in Section 4.2.1, beginning with Equation (4.2-4)

$$\Phi_k = CC^T \Phi_{\text{alon}} + \text{diag}(\bar{C})$$

Then any states corresponding to jets not firing during the last time step are initialized to the nominal thrust value of 870 lb.

Next, the Kalman filter gain matrix is calculated based on the previous error covariance and measurement noise. Here, we recall Equation (4.1-11)

$$K_k = P_k^- H_k^T (H_k P_k^- H_k^T + R_k)^{-1}$$

where, R_k contains the magnitude of the sensor measurement noise,

$$R_k = \begin{bmatrix} \sigma_\phi^2 & & \\ & \sigma_\theta^2 & \\ & & \sigma_\psi^2 \end{bmatrix} \quad (4.3-1)$$

With the new Kalman Gain, a measurement is incorporated and the state estimate is updated,

$$\hat{x}_k = \hat{x}_k^- + K(z_k - H_k \hat{x}_k^-)$$

The state error covariance matrix is updated,

$$P_k = (I - K_k H_k) P_k^-$$

The error covariance matrix, P_k , initially starts at the steady-state values implied by the choice of the process and measurement noises of the system without any jets firing.

When a jet fires, additional error is inserted into the state that corresponds to the jet firing. This error is injected when the jet first fires and, in effect, resets the filter for that state allowing each firing to be treated individually. Every time an individual jet fires the force estimate of that jet is reset. The estimate is reset to prevent measurements from earlier firings from corrupting the estimate of the next firing. By resetting the state with each new firing of the jet, the filter is able to quickly estimate the force produced in the event of degraded performance. Every time an individual jet fires the force estimate of that jet is reset.

Now the state estimate vector is extrapolated to the next time step using the transition matrix, aerosurface input and feedforward plume interaction term.

$$\hat{x}_{k+1}^- = \phi_k \hat{x}_k + \Lambda_k u_k + \omega_{plume} \quad (4.3-2)$$

Lastly the error covariance matrix is extrapolated to the next time step using the state transition matrix and adding the process noise.

$$P_{k+1}^- = \phi_k P_k \phi_k^T + G Q_k G^T \quad (4.3-3)$$

Figure (4.3-1), shows the filter loop used for estimation of jet force.

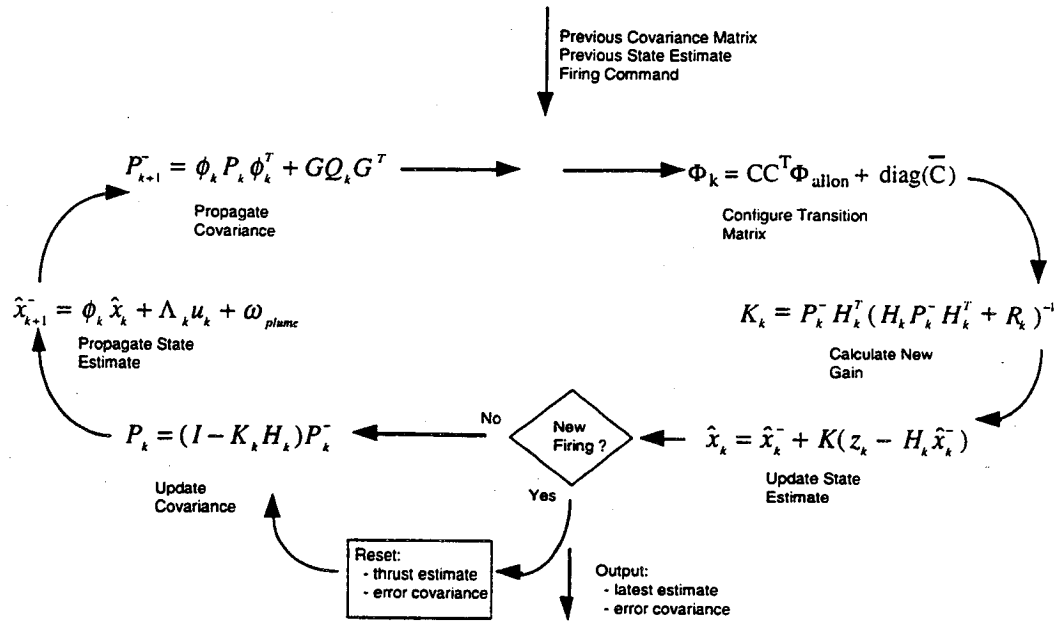


Figure 4.3-1: Kalman Filter Loop for Thrust Estimation

5.0 Kalman Filter Analysis

Chapter 5 presents an analysis of the Kalman filter designed in Chapter 4. First, open loop simulations are conducted to investigate the filter's ability to estimate jet thrust for different types of jets and different length firings. These open loop simulations use the linear model developed in Section 3.4 with white noise of the appropriate intensity for process and measurement noises. The quality of the estimate provided by different rate sensors is also examined.

Next, the filter is tested using a closed loop simulation that incorporates the entry flight control system. Incorporated into this simulation are the following modeling effects from Chapter 3: thrust transients, aerosurface dynamics, sensor models, and the nonlinear Euler coupling acceleration term. The bank maneuver from Section 3.8 is used to investigate the ability of the filter to estimate thrust by providing more realistic input commands with associated uncertainties and disturbances.

5.1 Open Loop Analysis

An error analysis is performed to determine the appropriate time step for the filter. The smaller the time step the more measurements that will be incorporated for a minimum impulse firing. With more rate measurements, more information is obtained yielding a better estimate. However, the penalty paid for a smaller time step is increased computational burden. Ideally, a time step is desired that provides an estimate of sufficient accuracy, yet is not so small that implementation of the filter becomes impractical. After establishing a time step, the effects of different sensors and firing times on the estimation error are investigated. Simulations of multiple jets firing simultaneously are also performed. The vehicle model used is Mach 7.5 with angle of attack 35°. The jet fired for the error analysis is a single, aft, side firing jet. The up and down firing jets have a slightly lower estimation error.

5.1.1 Effect of Δt

The minimum jet on-time for the Shuttle is 80 ms. The time step, Δt , of the filter will be chosen such that the resulting estimation error is less than 10% of

the nominal thrust produced (< 87 lb). Using the Kalman filter loop described in Section 4.3, the time history of the estimation error is determined for different Δt 's. Figure (5.1-1) shows the estimation error for a 80 ms firing resulting from the different time steps with the Shuttle IMU as the rate sensor.

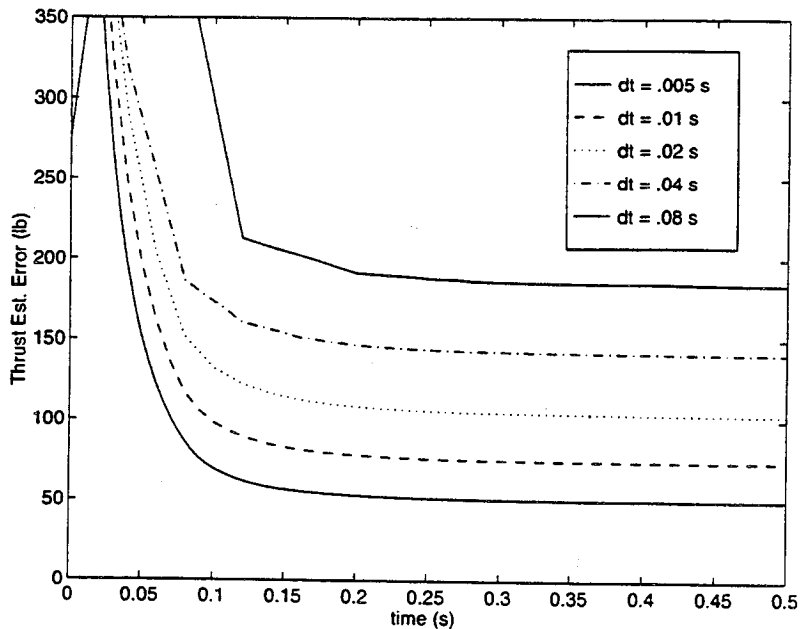


Figure 5.1-1: Estimation Error for Different Time Steps, 80 ms Firing (IMU sensor)

As shown in Figure (5.1-1) a sample time of 0.01 seconds meets the requirement of estimating the thrust to within 10 % for a minimum impulse firing. This sample time will be used throughout the remainder of the thesis.

5.1.2 Impact of Rate Sensor Precision

The noise characteristics of the rate sensor used to provide measurements for the estimator will affect the quality of the thrust estimate obtained. Sensors having smaller associated noise covariances will provide better quality estimates faster, but generally at the expense of additional hardware cost. Figure (5.1-2) shows the estimation error resulting from the different sensors for a minimum impulse firing.

Figure (5.1-2) shows that the less noisy a sensor is, the faster it reaches a lower steady state value. Only the Shuttle IMU and the TAI with interpolation (TAI2) provide the required accuracy.

Figure (5.1-3) also shows the estimation error for a step input to an aft side firing jet for different sensors. Once again the precision of the rate sensor affects the estimator bandwidth and speed of convergence.

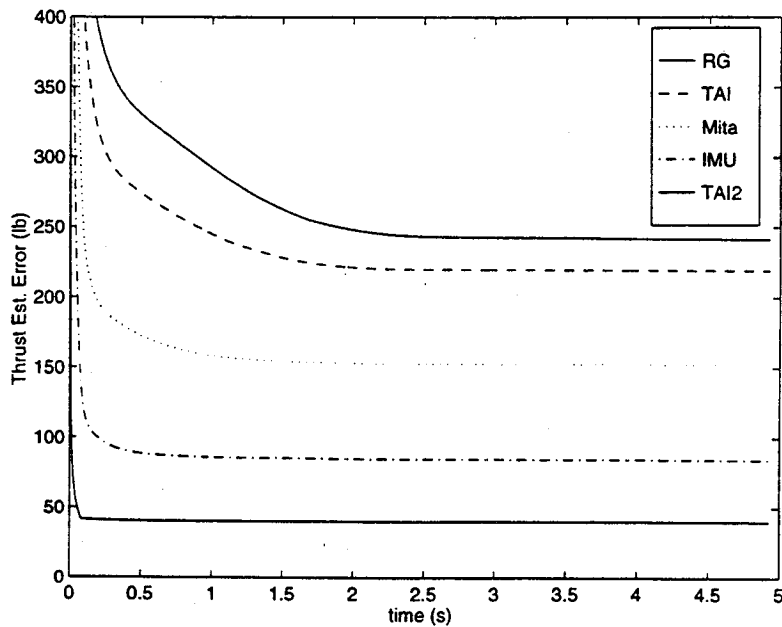


Figure 5.1-2: Estimation Error for Different Sensors for a Minimum Impulse Firing

5.1.3 Effect of Firing Length

As the time of the firing increases, the resulting steady state estimation error decreases. Figure (5.1-4) illustrates the relationship between firing time and resulting steady state error. Figure (5.1-4) was created using the IMU as the sensor. As the firing time increases, the resulting estimation error after the jet is off approaches its minimum value described in Section 5.1.2.

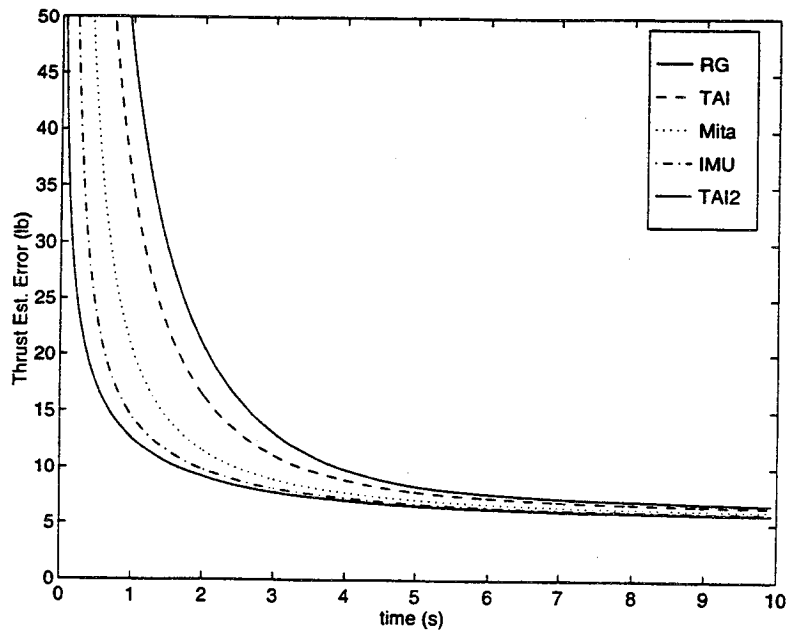


Figure 5.1-3: Steady State Thrust Estimation Error, Step Input to Side Firing Jet

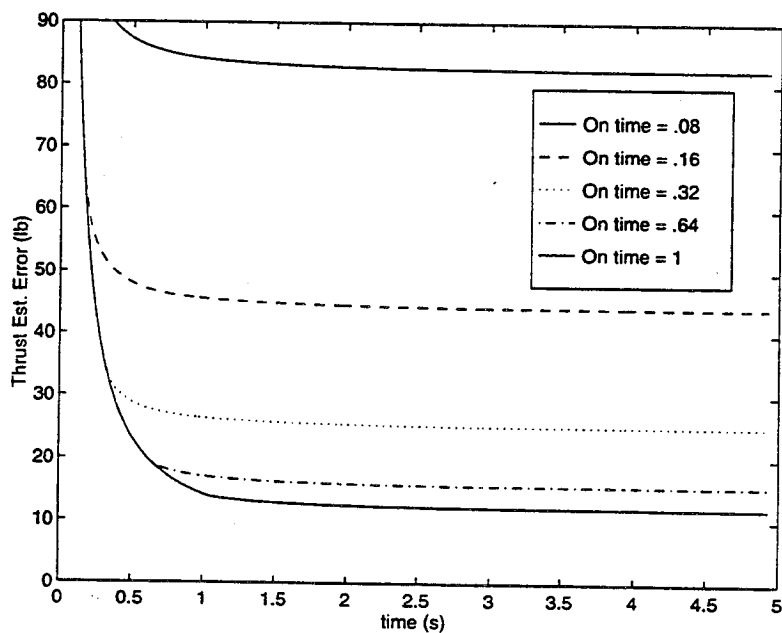


Figure 5.1-4: Effect of Firing Length on Estimation Error

5.1.4 Same Pod Multiple Jet Firings

In the figures illustrating the open loop filter performance, the top subplots show the force of the last firing (dashed), the filter estimate of the force of the last firing (solid) and the estimate plus and minus one error standard

deviation (dash-dot). The center subplots show the error (solid) which is the difference between the estimated and actual force of the last firing, and plus and minus one filter error standard deviation error. The bottom subplots illustrate the force and duration of the jet firings.

The desire to estimate the force produced by multiple jets firing simultaneously, influenced the structure of the designed filter as discussed in Chapter 4. Figure (5.1-5) shows the thrust estimate of a yaw and pitch jet firing at the same time. The filter estimates the thrust well when the jets are firing in different directions and produce different vehicle responses. However, as discussed in Section 4.4, when jets fire in similar directions and produce similar dynamic responses, the filter poorly estimates thrust. This inability to differentiate between multiple jets firing in the same direction motivated the creation of the multiple jet state. Figures (5.1-6) and (5.1-7) compare the thrust estimate of two co-directional jets firing concurrently estimated with two states and one state respectively. When two states are used to measure the thrust, the error covariance is large for each of the states indicating that the confidence in the estimate is low. When the jets are lumped together into one state, the resulting error covariance on the multiple jet state is less. By using one state, the ability to independently assess the thrust of each jet is traded for improved confidence in the estimate. This is important since the error covariance will be used to assess thrust estimate quality post-flight. Estimates with large error covariances will likely be discounted.

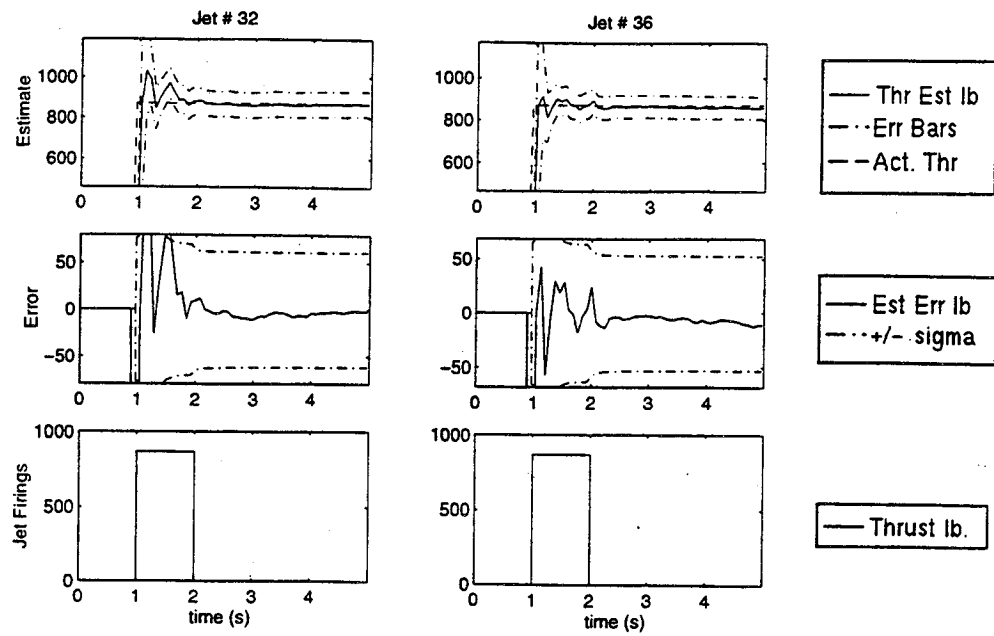


Figure 5.1-5: Estimation of Side (32) and Up (36) Jets Firing Simultaneously

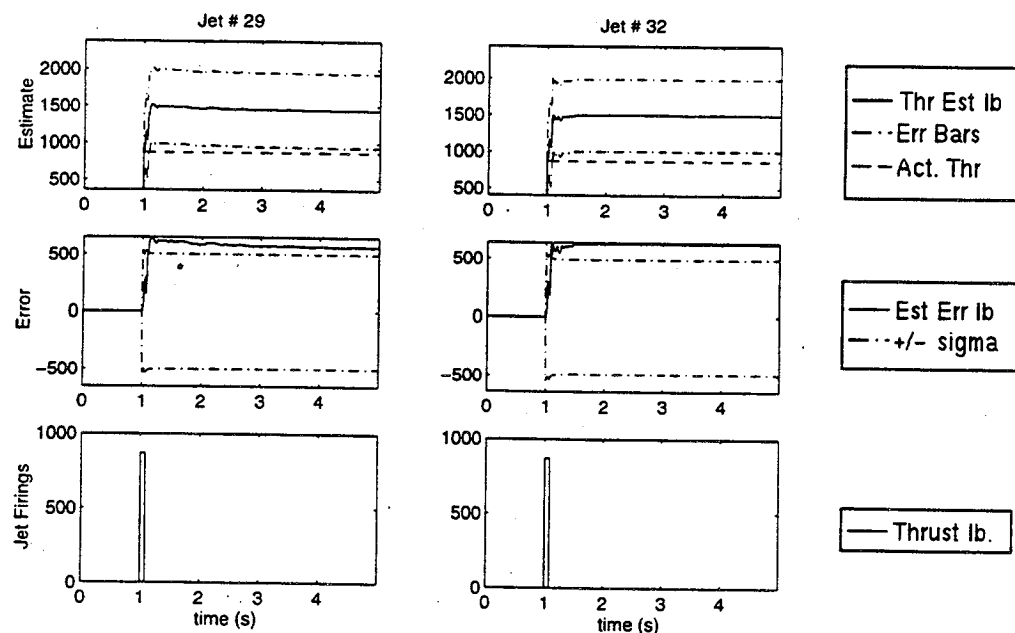


Figure 5.1-6: Estimation of Two Side Firing Jets Using Two States

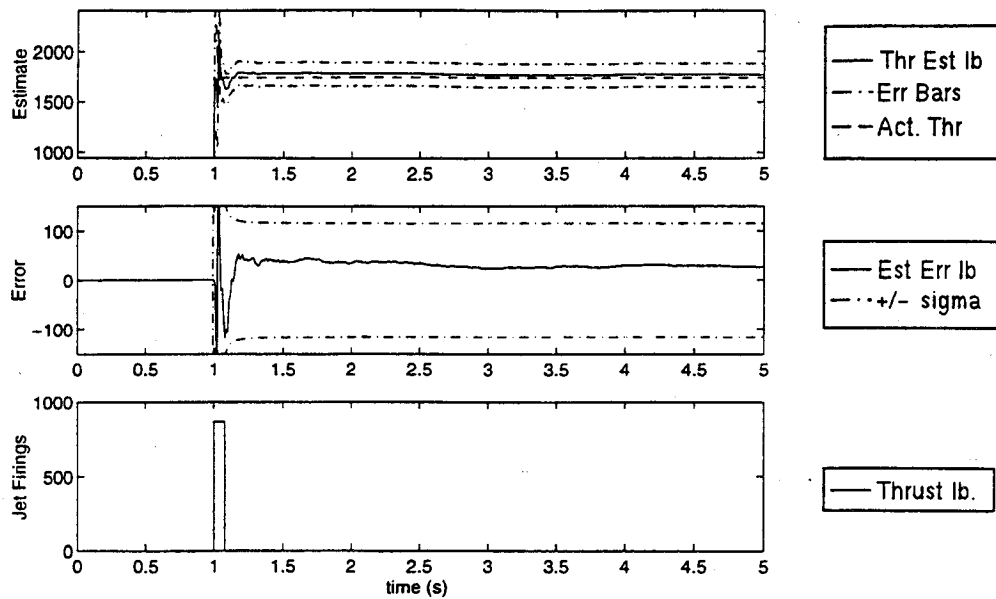


Figure 5.1-7: Estimation of Two Side Firing Jets Using One State

5.2 Closed Loop Simulation Analysis

To test the estimator under conditions that more closely approximate those encountered during Shuttle reentry, the closed loop simulation discussed in Chapter 3 is exercised for a typical maneuver. The simulation includes the reentry flight control system, models of the thrust profile, plume interaction effects, aerosurface dynamics, the vehicle dynamics, and sensor modeling.

5.2.1 Simulation Structure

Figure (5.2-1) depicts the structure of the closed loop simulation. The simulation is built modularly around the core of the linear model developed in Chapter 3. The VHM has inputs of: effector commands from the flight control system, plume interaction accelerations from the plume interaction module, and the vehicle rates from the sensor models. By processing these inputs the VHM generates estimates of jet thrust for each jet firing.

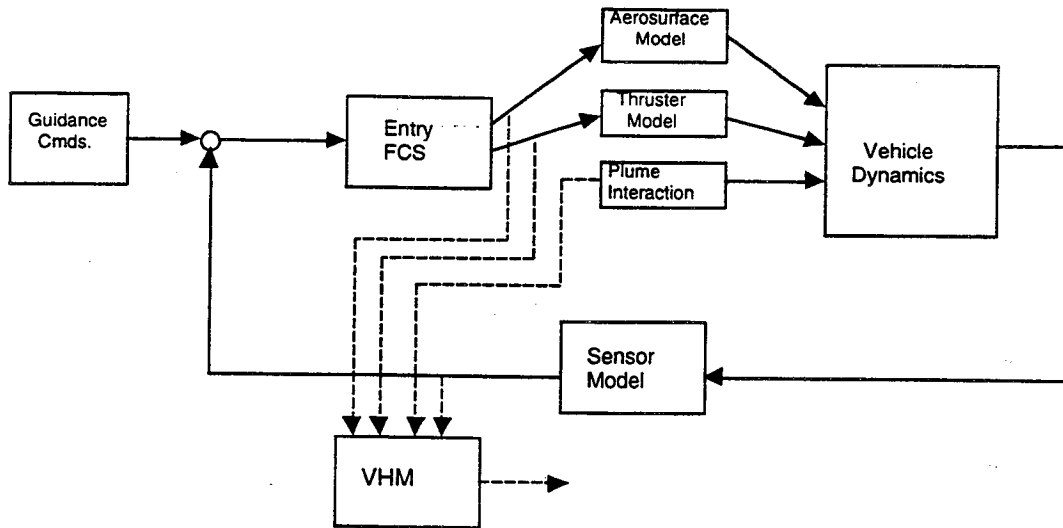


Figure 5.2-1: Block Diagram of Closed Loop Simulation

5.2.2 Kalman Filter Nominal Performance Analysis

As a reference, the filter is implemented using a “nominal” simulation. This simulation includes the quantization of rate measurements, Euler coupling, the flight control system, and the linear re-entry dynamics model. The rate sensor implemented in these simulations is the Shuttle IMU.

The example bank command, described in Section 3.8, is executed for the simulation. A series of jets fire during the maneuver as documented in Table (5.2-1). After a jet ON command, the VHM monitor records the time of firing, tracks the length of the firing, and records the last estimate and filter standard deviation (square root of error covariance) before the filter is reset by the next jet ON command. The abbreviation “RxR” corresponds to right RCS, right firing (the “x” indicates the priority jets of that group). The estimation length for a given firing is the time from the start of that firing until the beginning of the next firing. A similar table follows each simulation to quantify the data presented in the plots.

Results of the simulation are shown in Figure (5.2-2). In this plot, the top subplot illustrates the estimated and actual total force from the last firing of the yaw jets (the estimate is the filter F_{mult} state described in Section 4.2.1). The center subplot is the error between the estimated and actual force of the last firing. The bottom subplot shows the duration and combined force of all yaw jets.

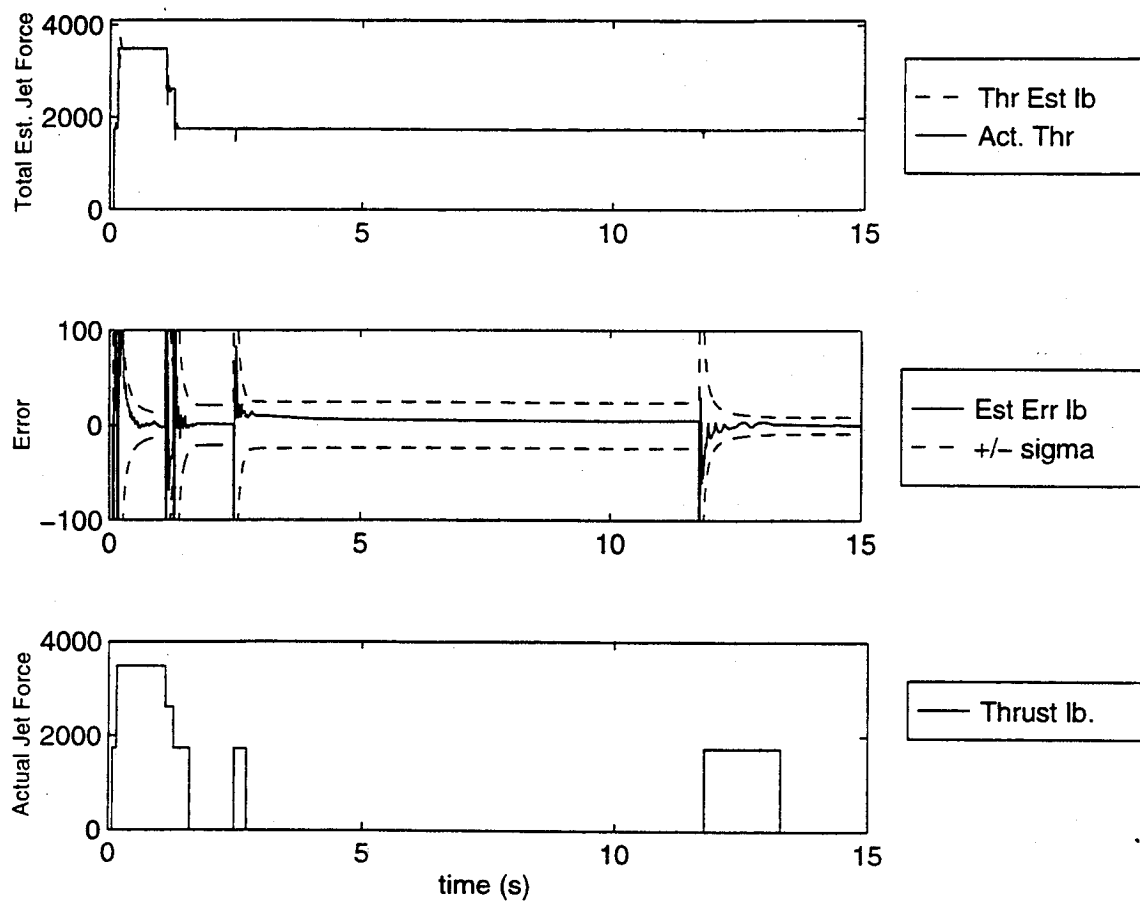


Figure 5.2-2: Kalman Filter Monitor Response For Nominal Bank Command

Firing Time (s)	Jet ID	Firing Length (s)	Estimation Length (s)	Thrust Estimate (lb)	Error (lb)	Filt. Stand. Dev. (lb)
0.08	2 LxL	0.080	0.080	1743	+3	121.5
0.16	4 LxL	0.960	0.960	3478	-2	11.8
1.12	3 LxL	0.160	0.160	2596	-14	52.9
1.28	2 LxL	0.320	1.200	1741	+1	21.1
2.48	2 RxR	0.240	9.280	1744	+4	24.0
11.76	2 RxR	1.520	3.240	1740	0	8.5

Table 5.2-1: Output Table from VHM for Nominal Simulation

To check the filter's ability to detect off nominal or degraded thruster performance, the jet thrust is reduced by 10% in the simulation for the firing that occurs between 2 and 3 seconds. The thrust was decreased by 10% because the goal of the VHM system was to identify off-nominal performance, with off-nominal defined as a greater than 10% deviation. Figure (5.2-3) and Table (5.2-2)

show that the estimator readily tracks the shift in thrust for this firing, with an error of only 6 lb.

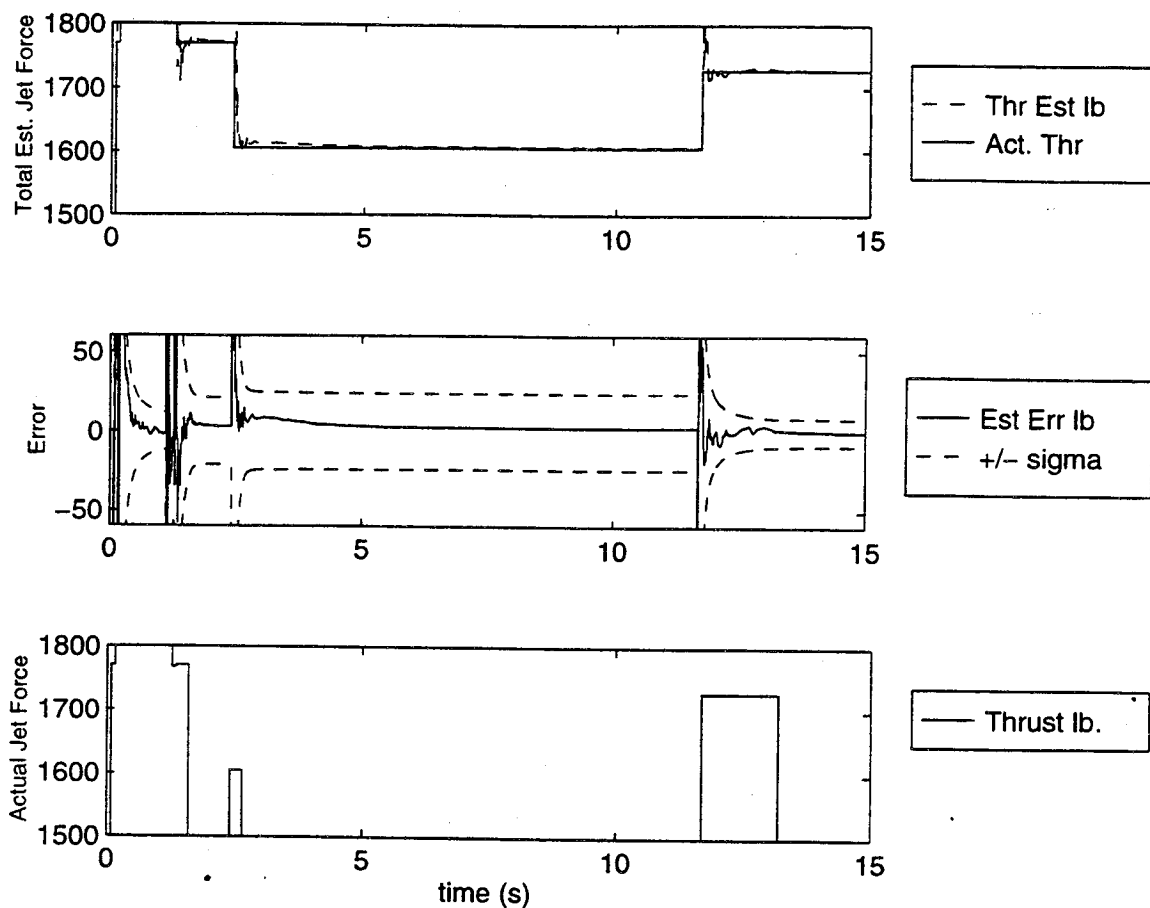


Figure 5.2-3: Response to a Degraded Jet Thrust

Firing Time (s)	Jet ID	Firing Length (s)	Estimation Length (s)	Thrust Estimate (lb)	Error (lb)	Filt. Stand. Dev. (lb)
2.48	2 RxR	0.240	9.280	1608	+6	24.0

Table 5.2-2: Output Table from VHM for Degraded Thruster Firing

When evaluating the simulation results, an important factor to consider is the size of the error relative to the filter error covariance. When the system is in operation, the estimate is expected to be within the error bounds implied by the error covariance matrix. The error bounds set by the time history of the covariance matrix are the only measure of accuracy on the estimate. Therefore, if the absolute value of estimation error is not significantly larger than the standard

deviation predicted by the filter, the design is considered acceptable. If the estimation error is significantly larger than the error bounds, the estimate is assumed to be corrupted and the filter covariance loses its significance.

5.2.3 Kalman Filter and Modeling Error

Neglected dynamics and system lags will further degrade estimator performance from that illustrated in Section 5.2.2. The VHM system must produce acceptable estimates of jet thrust and accurate associated error covariances when subjected to these additional system uncertainties if the monitoring system is to provide useful information for the reduction of life cycle costs. These additional uncertainties include the aerosurface actuator dynamics, thruster valve transients, vehicle aerodynamic modeling errors, and uncertainty in the moment induced by plume interaction. In the sections to follow, each of the unmodeled elements is added individually to examine their effect on the estimate and its error covariance.

5.2.3.1 Effect of Aerosurface Dynamics

The dynamic response of the aerosurface actuator has a significant impact on the Kalman filter's ability to estimate the force of a jet firing. Recall that the modeled aerosurface dynamics are the sum of a damped second order response with high frequency noise. The effect of the aerosurface actuator dynamics on the Kalman filter design is an additional contribution to the process noise driving term. A noise intensity of $\frac{1}{20}$ ° is added as described in Section 3.5. Figure (5.2-4) and Table (5.2-3) show the filter response with the aerosurface dynamics added to the simulation.

The estimation error is large for the first three or four seconds and for each of the firings occurring over that time span. Most of the degradation in performance is caused by the aerosurface actuator time delay in reaching the commanded deflection. One solution to this problem is to delay the aerosurface command feedforward to the Kalman filter. A delay of 0.07 seconds was chosen. The delay had to be accurate to within fifteen percent to correct for the poor estimate induced by the aerosurface dynamics. Figure (5.2-5) and Table (5.2-4) show the improvement in filter performance with the delay modeled in the filter. Without the incorporation of the filter delay, the filter expects significant accelerations immediately due to aerosurface deflections. The filter accounts for the absence of the anticipated rates by adjusting the value of the thrust estimate.

The most significant deviations from zero error occur when the ailerons are in motion and the actuator dynamics cause a lag between the commanded and actual aerosurface position. Firings having smaller estimation errors occur when aerosurface deflection rates slow, allowing the actual aerosurface deflection to "catch-up" with the commanded deflection. The timing of the jet firings with the commanded and actual aerosurface deflections are illustrated in Figure (5.2-6).

The high frequency aerosurface jitter is a negligible effect. The high frequency noise does not pose a problem to the estimation of jet thrust because its spectrum is beyond the passband of both the vehicle dynamics and filter. If the noise is within the passband, a shaping filter can be used in the filter model to reject the noise in the estimate.

When actually implemented, any estimation system will have to be thoroughly ground tested to discover the many delays in a system that could inadvertently degrade monitoring performance. These delays should be known for most vehicles since they are characterized for flight control system design and testing.

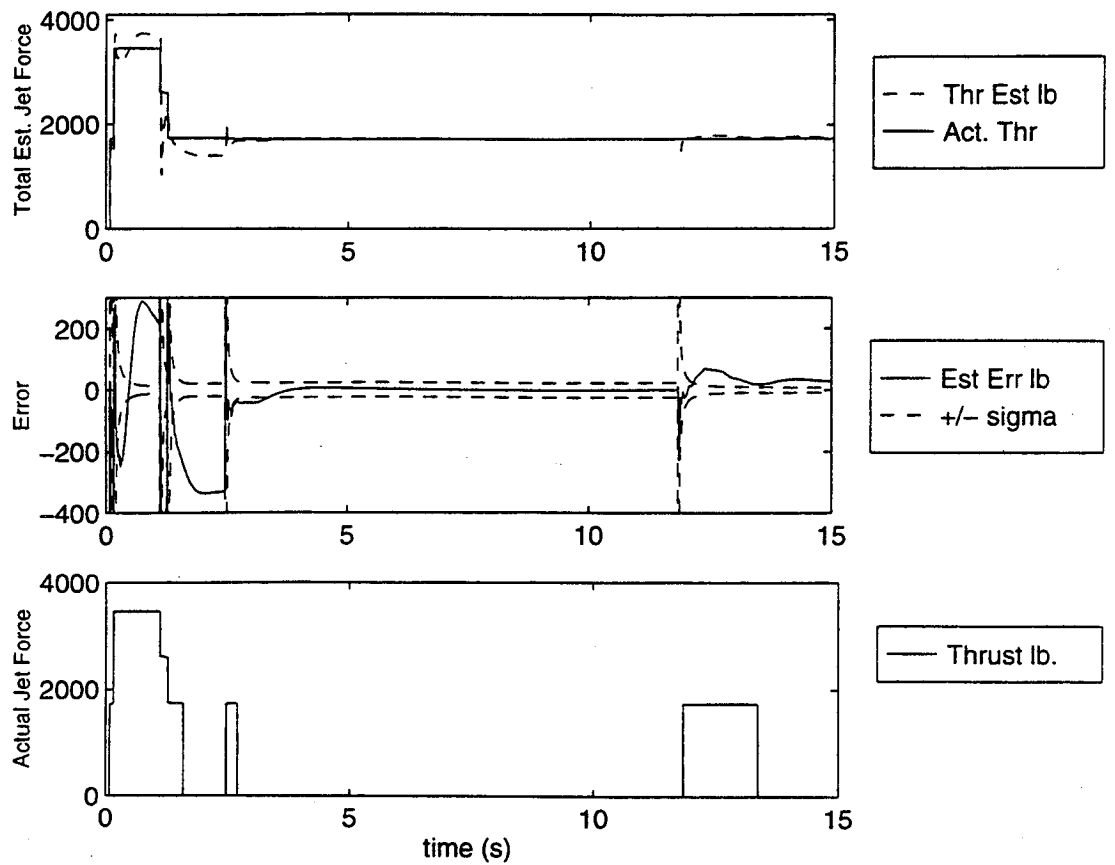


Figure 5.2-4: Effect of Aerosurface Dynamics

Firing Time (s)	Jet ID	Firing Length (s)	Estimation Length (s)	Thrust Estimate (lb)	Error (lb)	Filt. Stand. Dev. (lb)
0.08	2 LxL	0.080	0.080	1612	-128	121.5
0.16	4 LxL	0.960	0.960	3691	211	11.8
1.12	3 LxL	0.160	0.160	2262	-348	52.9
1.28	2 LxL	0.320	1.200	1400	-340	21.1
2.48	2 RxR	0.240	9.280	1783	43	24.0
11.76	2 RxR	1.520	3.240	1775	35	8.5

Table 5.2-3: Output Table from VHM for Simulation w/ Aerosurface Dynamics

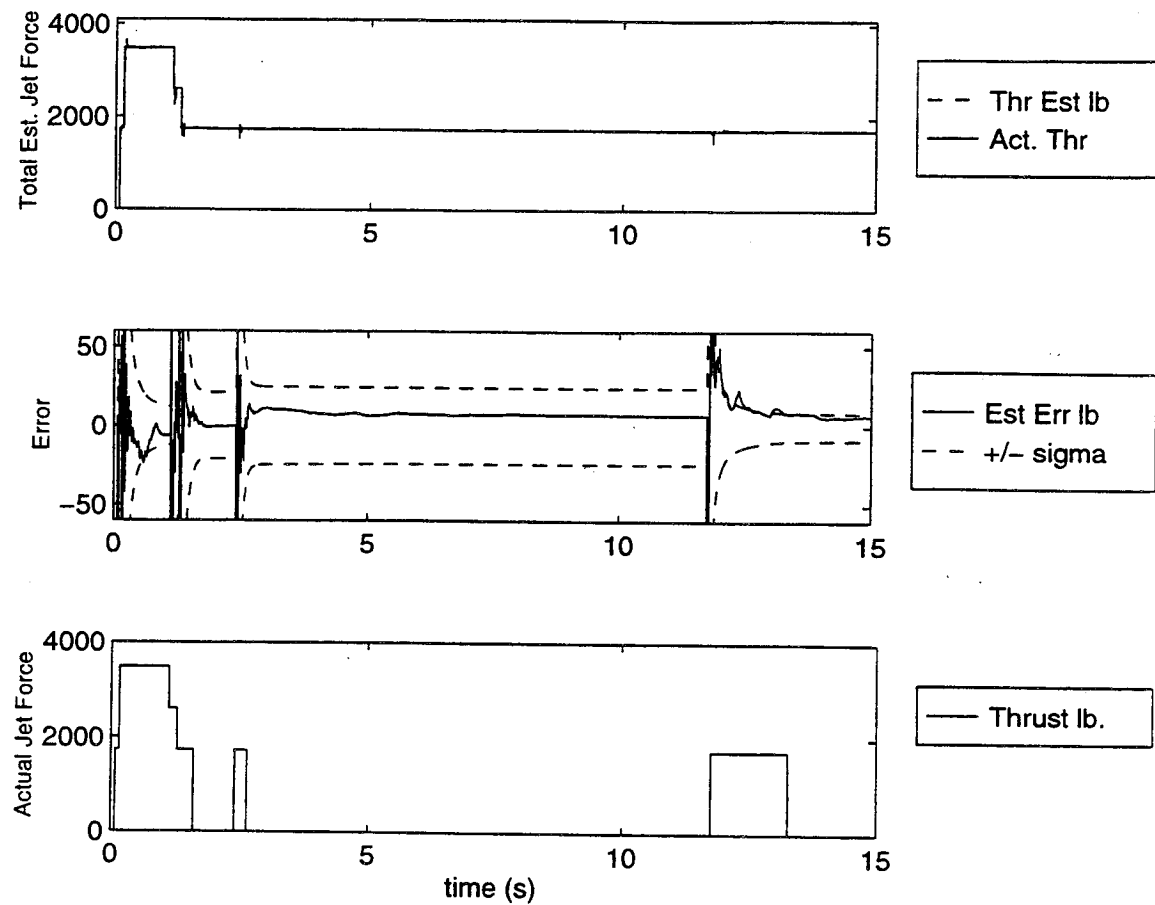


Figure 5.2-5: Effect of Aerosurface Dynamics w/ Delay Added

Firing Time (s)	Jet ID	Firing Length (s)	Estimation Length (s)	Thrust Estimate (lb)	Error (lb)	Filt. Stand. Dev. (lb)
0.08	2 LxL	0.080	0.080	1773	33	121.5
0.16	4 LxL	0.960	0.960	3474	-6	11.8
1.12	3 LxL	0.160	0.160	2590	-19	52.9
1.28	2 LxL	0.320	1.200	1740	0	21.1
2.48	2 RxR	0.240	9.280	1747	7	24.0
11.76	2 RxR	1.520	3.240	1747	6	8.5

Table 5.2-4: Output Table from VHM for Simulation w/ Delay Added

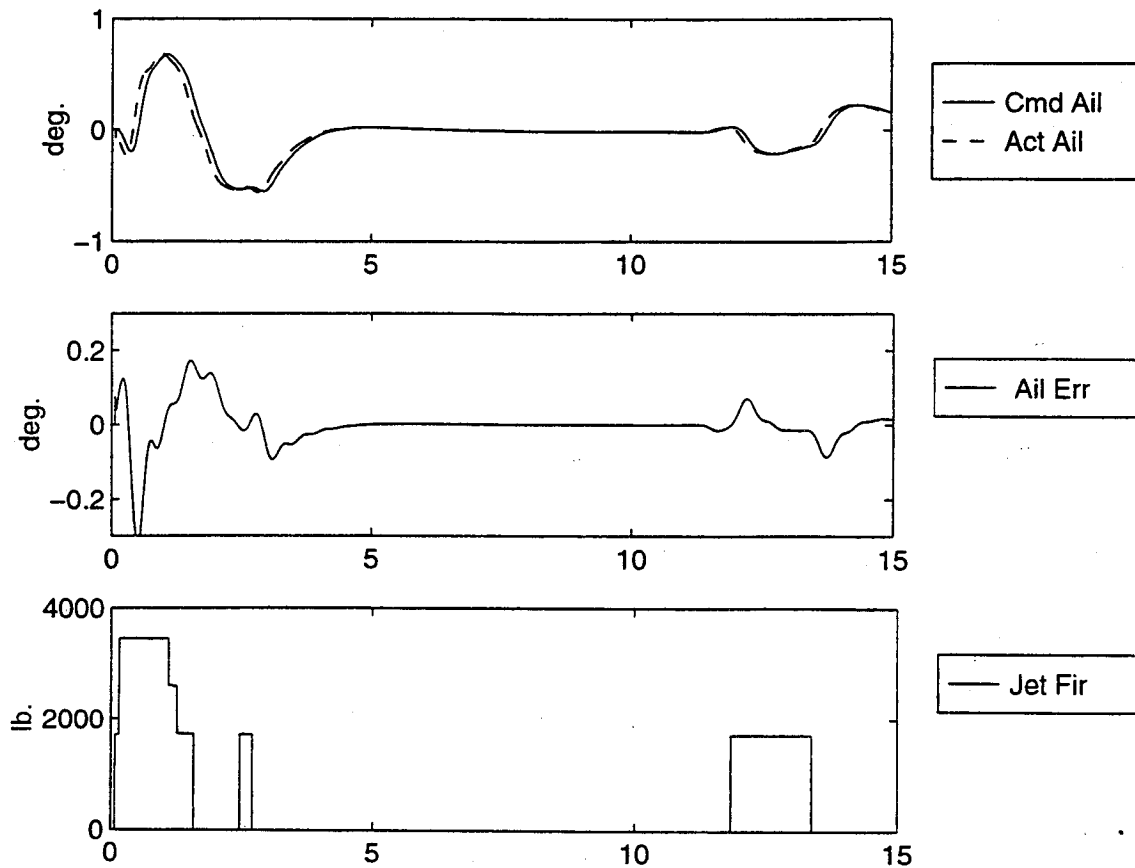


Figure 5.2-6: Timing Relationship of Aerosurface Deflection and Jet Firings

5.2.3.2 Effect of Thrust Scaling

Figure (5.2-7) and Table (5.2-5) show the effect of including the jet thrust model on the estimate of jet thrust. The jet thrust model (Section 3.6) accounts for thruster valve open/close transients and thrust modeling errors. The model has two components: a steady state error of $\pm 3\%$ and a second order lag representation of the jet thrust rise and fall profiles. To account for the degradation in the thrust estimate an appropriate delay for the jet ON command to the VHM monitor should be added as in the aerosurface actuator dynamics case.

For the example bank command, the estimate for individual “stand-alone” firings has little steady state error, but there is a significant transient that is not present in the nominal case. Initially the estimate is low, as the estimator is expecting the effect of the firing, but the thrust is still ramping up. After the jet is

commanded OFF, the estimator converges because it is expecting no thrust, but the thrust is still decaying.

For the sequential firings at the beginning of the simulation run, the ramp up and tail off effects overlap for the firings as additional jets are added or removed. This overlap cancels out the effect from one firing to the next in this sequence, until the last firing when the tail off adds more rate than expected and the estimate goes slightly high. This slight overestimate is seen in the 'Error' subplot of Figure (5.2-7) and in Table (5.2-5) for the firing at 1.28 s.

Like the aerosurface dynamics, the factor that effects the estimate in the thrust dynamics is the delay. If an appropriate delay were added to the jet command feedforward to the filter, the effects of thruster transients would be reduced.

In Table (5.2-5) some of the estimation errors are larger than the standard deviation, but in Figure (5.2-7) the estimation error is less than the standard deviation. The difference is that for the plot the error is calculated using the *actual* value produced in the simulation, so it accounts for the $\pm 3\%$ error in the thrust level. The table, representing a VHM output calculates the error based on the nominal thrust values.

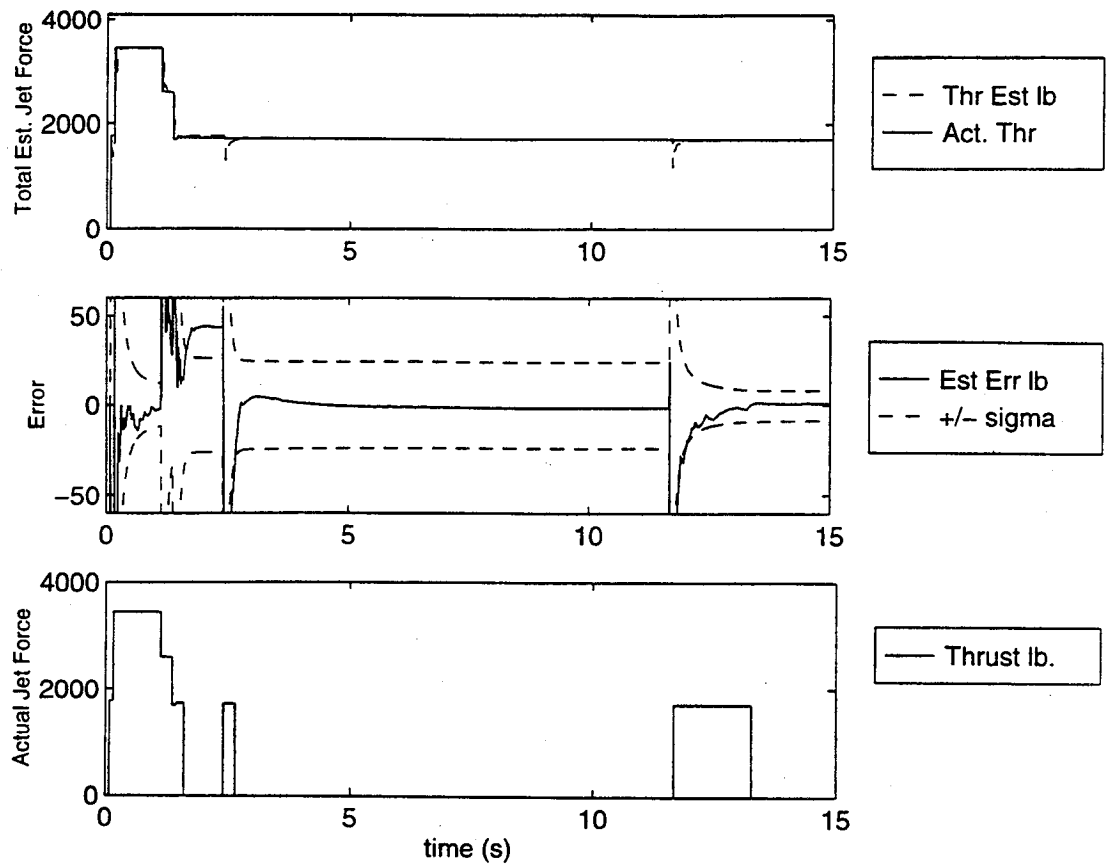


Figure 5.2-7: Effect of Thrust on Estimator Response

Firing Time (s)	Jet ID	Firing Length (s)	Estimation Length (s)	Thrust Estimate (lb)	Error (lb)	Filt. Stand. Dev. (lb)
0.08	2 LxL	0.080	0.080	1642	-98	121.5
0.16	4 LxL	0.960	0.960	3447	-33	11.8
1.12	3 LxL	0.160	0.160	2628	18	52.9
1.28	2 LxL	0.320	1.200	1782	41	21.1
2.48	2 RxR	0.240	9.280	1725	-15	24.0
11.76	2 RxR	1.520	3.240	1717	-23	8.5

Table 5.2-5: Output Table from VHM for Simulation w/ Thrust Model

5.2.3.3 Aerodynamic Uncertainties

To investigate the filter's robustness to aerodynamic modeling error, the Kalman filter was designed using a linear plant model based on one flight condition while the simulation vehicle dynamics used a linear model based on a different flight condition. The difference between any two linear models is a slight change in jet and aerosurface effectiveness and a small shift in the modal

frequencies. Although the Kalman filter is guaranteed to be stable if the plant is stable, there is no guarantee that the error performance will be satisfactory or that the filter will converge in a reasonable amount of time.

For a perturbed plant model the Kalman filter will most likely result in large errors. Figure (5.2-8) and Table (5.2-6) show this error. The filter is designed for the model at Mach 8.8 and the simulation is run using the model based on the plant at Mach 7.5. As shown by the plot, the plant model must be well known for the Kalman filter to provide acceptable estimates.

Initially ($0 < t < 3$) the filter seems to perform satisfactorily. However, the filter residuals grow rapidly due to the estimation error. The estimation error exceeds the filter error standard deviation by a factor of more than 100. In addition there are large transients in the thrust estimate induced by the modeling error. Because there is a difference in the mapping from jet force to stability axis angular accelerations between the two models, the magnitude of the error, both steady state and transient, after a firing is proportional to the length and magnitude of the firing. Clearly these results are unacceptable for use by a VHM system. To implement a Kalman filter based VHM, the models of the system would need to be very accurate. One alternative to the Kalman filter for these cases is provided in Chapter 6.

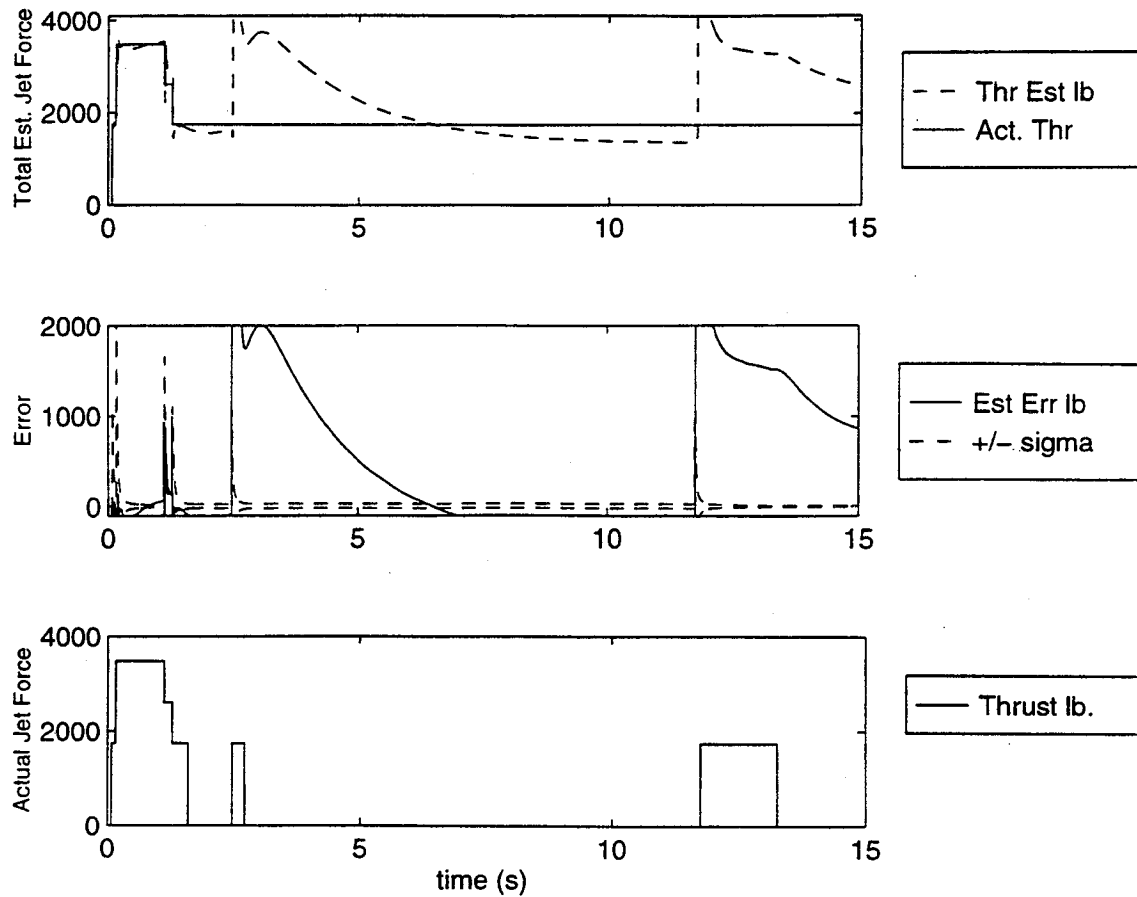


Figure 5.2-8: Effect of Incorrect Aerodynamic Model

Firing Time (s)	Jet ID	Firing Length (s)	Estimate Length (s)	Thrust Estimate (lb)	Error (lb)	Filt. Stand. Dev. (lb)
0.08	2 LxL	0.080	0.080	1657	-83	121.5
0.16	4 LxL	0.960	0.960	3540	60	11.8
1.12	3 LxL	0.160	0.160	2737	128	52.9
1.28	2 LxL	0.320	1.200	1663	-76	21.1
2.48	2 RxR	0.240	9.280	1356	-383	24.0
11.76	2 RxR	1.520	3.240	2597	857	8.5

Table 5.2-6: Output Table from VHM for Simulation w/ Incorrect Aerodynamic Model

5.2.3.4 Plume Interaction Uncertainties

The maximum error in the plume interaction moment prediction for the firing of 4 yaw jets is about 33% (calculated from [OABD]). Figure (5.2-9) and Table (5.2-7) show the scenario if the plume interaction term is over estimated by

33%. Complete ignorance of the plume interaction may cause errors on the order of 100 %. Notice that error in the plume interaction term causes an almost constant bias for the given flight condition. The plume interaction effect directly effects the net torque transmitted to the vehicle when a jet fires. For this reason, it is difficult to separate the plume interaction effects from the effects of a jet firing in the vehicle's dynamic response.

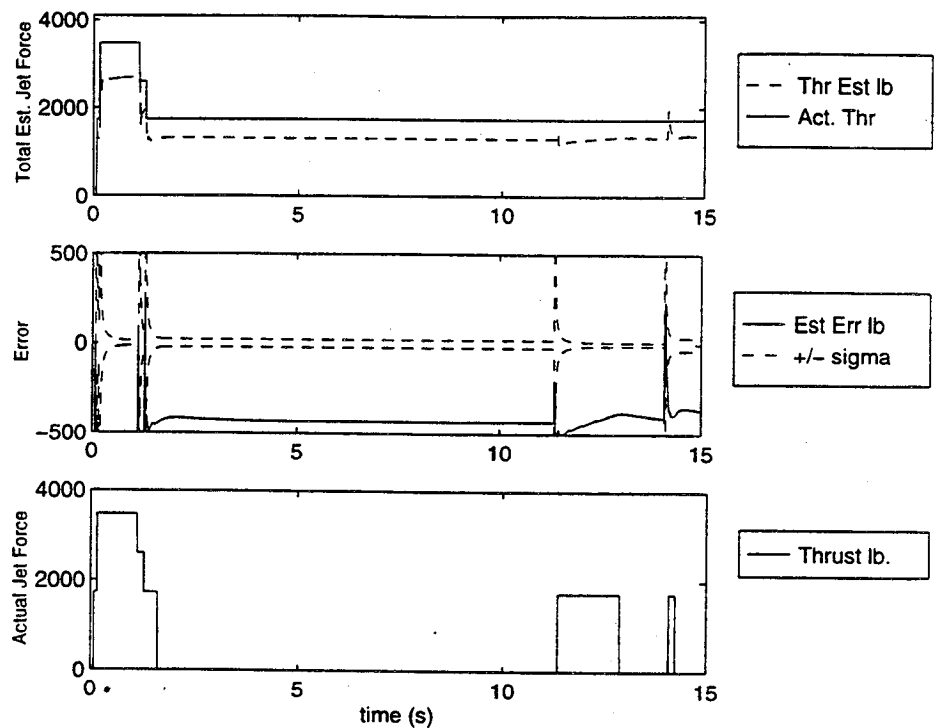


Figure 5.2-9: Effect of 33% Error in Plume Interaction Term

Firing Time (s)	Jet ID	Firing Length (s)	Estimation Length (s)	Thrust Estimate (lb)	Error (lb)	Filt. Stand. Dev. (lb)
0.08	2 LxL	0.080	0.080	1289	-451	121.5
0.16	4 LxL	0.960	0.960	2705	-775	11.8
1.12	3 LxL	0.160	0.160	1954	-656	52.9
1.28	2 LxL	0.320	1.200	1308	-431	21.1
2.48	2 RxR	0.240	9.280	1330	-409	24.0
11.76	2 RxR	1.520	3.240	1369	-371	8.5

Table 5.2-7: Output Table from VHM for Simulation w/ 33% Error in Jet Plume Interaction Term

6.0 Robust Estimator Design

As shown in the previous chapter, the Kalman filter poorly estimates thrust in the presence of modeling uncertainty. The Kalman filter takes a given nominal plant model and provides the optimal estimates for that particular plant model. With perturbed model parameters, the Kalman filter, designed for the nominal plant, provides estimates that are no longer optimal and may, in fact, be quite poor. A different type of estimator may be more robust to this plant modeling uncertainty. Yaesh and Shaked as well as Khargonekar and Nagpal derived continuous, time invariant estimators that are robust to bounded noise modeling errors, but neglect plant modeling errors [Yaesh Khargonekar]. Appleby formulated an estimator that is robust to both plant and noise modeling uncertainty. This section begins with an overview of the design methods in [Appleby], followed by the formulation of a simple thrust estimation problem. Lastly, performance comparisons are made between the Kalman filter and the robust estimator applied to the simple example.

6.1 H_2 and H_∞ Optimal Estimators

In this chapter, all of the estimators are continuous-time. As such, the estimators will use steady state gains, not the time varying gains of the last chapter. Consequently, the time response of the resulting filters is much slower, because the initial high gains introduced at the beginning of a firing in the time-varying filter are not present. Robust time-varying filters have been recently derived [Mangoubi]. Unfortunately, software to facilitate the design of these estimators is still in a development stage and is not ready for use.

6.1.1 Continuous Kalman Filter

For comparison to the robust method, a continuous Kalman filter is also designed for the example problem. The continuous-time Kalman filter may be derived from the discrete-time Kalman filter by allowing the time interval to go to zero in the limit. A Riccati equation results which describes the error dynamics.

$$\dot{P} = AP + PA^T + GQG^T - PC^T R^{-1} CP \quad (6.1-1)$$

Setting this equal to zero and solving for P , allows the Kalman gain to be found through,

$$K = PC^T R^{-1} \quad (6.1-2)$$

As in the discrete case, the continuous Kalman filter minimizes the square of the estimation error.

6.1.2 Minimax Estimator

Like the Kalman filter, the minimax estimator in [Appleby] minimizes the 2-norm of the estimation error, but does so for noise that is bounded in energy with an unknown frequency content. The estimator has the same form as the Kalman filter, thus the estimation error dynamics are given by

$$\begin{aligned} \tilde{x} &\equiv x - \hat{x} \\ \dot{\tilde{x}} &= (A - KC)\tilde{x} + [\Gamma_1 - K\Gamma_2]d \\ &= A_{\tilde{x}}\tilde{x} + \Gamma_{\tilde{x}}d \\ e &= M\tilde{x} \end{aligned} \quad (6.1-3)$$

or the following state space representation

$$P(s) = \left[\begin{array}{c|cc} A & [\Gamma_1 & 0] & 0 \\ \hline M & 0 & -I \\ C & [0 & \Gamma_2] & 0 \end{array} \right] \quad (6.1-4)$$

where, Γ_1 is the process noise and Γ_2 is the measurement noise. The process and measurement noise are assumed to be uncorrelated since $\bar{B}_1 \bar{D}_{21}^T = 0$.

The estimator gain, K , minimizes the 2-norm of the error for the worst case combination of the disturbances subject to the constraint imposed by the state dynamics,

$$\min_K \max_d \|e\|^2 \text{ given } \|d\|^2 \leq D \text{ and } \dot{\tilde{x}} = A_{\tilde{x}}\tilde{x} + \Gamma_{\tilde{x}}d \quad (6.1-5)$$

The cost function is the integral of the estimation error with the system dynamics and the bounded noise uncertainty appended with the Lagrange multipliers γ and λ , respectively. The cost function is shown in Equation (6.1-5)

$$J = \int_0^T \left[\tilde{x}^T M^T M \tilde{x} - \gamma^2 d^T d + \lambda^T (\dot{\tilde{x}} - A_{\tilde{x}} \tilde{x} - \Gamma_{\tilde{x}} d) \right] dt + \gamma^2 D \quad (6.1-6)$$

The minimizing gain, K , is found through variational calculus and given by,

$$K = P C^T R^{-1} \quad (6.1-7)$$

where, P is the steady state solution to the following Riccati equation.

$$\dot{P} = AP + PA^T + GQG^T - P \left(C^T R^{-1} C - \gamma^2 M^T M \right) P \quad (6.1-8)$$

Notice that as γ approaches infinity the Riccati equation of (6.1-8) becomes the Riccati equation for the Kalman filter, Equation (6.6-1).

6.1.3 Structure for Robust Estimation

The three block structure shown in Figure (6.1-1), is a general representation of a plant, estimator, and uncertainty used in robust estimation analysis and design. The example plant model will be rearranged into the three-block structure in the next section for implementation of the robust estimator. The Δ block lumps all the plant uncertainty into a single point in the transfer function. This plant modeling uncertainty may include unmodeled dynamics and parametric uncertainty. Examples of unmodeled dynamics include neglected sensor or actuator dynamics, or dynamics lost due to model reduction.

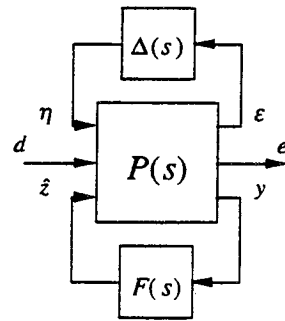


Figure 6.1-1: General Transfer Function Representation

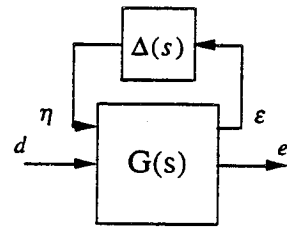


Figure 6.1-2: Closed Loop Block Diagram

Combining P and F gives the closed loop transfer function, G , shown in Figure (6.1-2). This closed loop transfer function can be broken into four blocks

$$\begin{bmatrix} \varepsilon \\ e \end{bmatrix} = \begin{bmatrix} G_{11}(s) & G_{12}(s) \\ G_{21}(s) & G_{22}(s) \end{bmatrix} \begin{bmatrix} \eta \\ d \end{bmatrix} \quad (6.1-9)$$

G_{22} is the nominal open loop transfer function. The transfer function from the disturbances, d , to the error, e , is given by

$$G_{ed}(s) = G_{22}(s) + G_{21}(s)\Delta(s) \left[I - G_{11}(s)\Delta(s) \right]^{-1} G_{12}(s) \quad (6.1-10)$$

Robust performance is measured by the maximum gain of the closed loop, $\|G_{ed}(s)\|_\infty$, given norm bounded modeling uncertainty. With normalized inputs and outputs the robust performance goal is

$$\|G_{ed}(s)\|_\infty < 1 \quad (6.1-11)$$

A sufficient condition for robust performance is that

$$\|G(s)\|_\infty < 1 \quad (6.1-12)$$

6.1.4 General Minimax Estimator Design

Unlike the minimax estimator which is robust only to norm bounded noise uncertainty, the generalized minimax estimator also accounts for perturbations in the plant model dynamics.

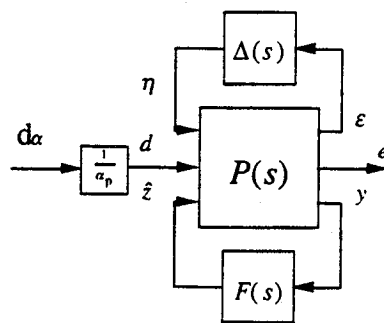


Figure 6.1-3: General Transfer Function Representation

With the perturbations added and the scaling explicitly accounted for in the model by the term $\frac{1}{\alpha_p}$, shown in Figure (6.1-3), the state space equations for the system are

$$\begin{bmatrix} \dot{x} \\ \dot{\epsilon} \\ \dot{e} \\ \dot{y} \end{bmatrix} = \begin{bmatrix} A & B_1 & \frac{1}{\alpha_p} B_2 & 0 \\ C_1 & D_{11} & \frac{1}{\alpha_p} D_{12} & 0 \\ C_2 & D_{21} & \frac{1}{\alpha_p} D_{22} & -I \\ C_3 & D_{31} & \frac{1}{\alpha_p} D_{32} & 0 \end{bmatrix} \begin{bmatrix} x \\ \eta \\ d \\ \hat{z} \end{bmatrix} \quad (6.1-13)$$

Incorporating the estimator into the plant yields the closed loop transfer function given by,

$$G(s) = \begin{bmatrix} G_{11}(s) & G_{12}(s) \\ G_{21}(s) & G_{22}(s) \end{bmatrix} = \begin{bmatrix} P_{11} & P_{12} \\ P_{21} - FP_{31} & P_{22} - FP_{32} \end{bmatrix} \quad (6.1-14)$$

As stated before, a sufficient condition for robust performance is that,

$$\|G(s)\|_{\infty} < 1 \quad (6.1-15)$$

For the previous minimax estimator without the modeling uncertainty, the closed loop transfer function was of the form,

$$G = P_{11} - FP_{21} \quad (6.1-16)$$

To design a robust estimator that includes the plant modeling uncertainty, the closed loop transfer function of Equation (6.1-14) will be placed in the form of Equation (6.1-16). The first step of this process is to combine the inputs η and d_{α} of Figure (6.1-3) into a single input. This combination puts the closed loop plant into the form

$$G(s) = \begin{bmatrix} P_{c_{-11}} \\ P_{c_{-21}} - FP_{c_{-31}} \end{bmatrix} \quad (6.1-17)$$

Rewriting $G(s)$ as

$$G(s) = \begin{bmatrix} G_1(s) \\ G_2(s) \end{bmatrix} \quad (6.1-18)$$

a sufficient condition for robust performance is now

$$\left\| \begin{bmatrix} G_1(s) \\ G_2(s) \end{bmatrix} \right\|_{\infty} < 1 \quad (6.1-19)$$

Next a spectral factorization is used to imbed $G_1(s)$ into $G_2(s)$, allowing a solution by a generalized minimax approach.

Using the condition for robust performance, applying the definition of the vector 2-norm, and rewriting, the following inequality holds,

$$G_1^-(s)G_1(s) + G_2^-(s)G_2(s) < I \quad (6.1-20)$$

this leads to a bound on $G_2(s)$

$$G_2^-(s)G_2(s) < I - G_1^-(s)G_1(s) = G_{sf}^-(s)G_{sf}(s) \quad (6.1-21)$$

where, $G_{sf}(s)$ is a spectral factor obtained through the solution of an algebraic Riccati equation as outlined in Appendix C.

Rewriting Equation (6.1-21) gives,

$$G_{sf}^{-1}(s)G_2^-(s)G_2(s)G_{sf}^{-1}(s) < I \quad (6.1-21)$$

which leads to the norm bound,

$$\|G_2(s)G_{sf}^{-1}(s)\|_{\infty} = \|P_{c_{-21}}G_{sf}^{-1}(s) - FP_{c_{-31}}G_{sf}^{-1}(s)\|_{\infty} < 1 \quad (6.1-22)$$

Equation (6.1-22) is now in the same form as Equation (6.1-14), the closed loop form solved in the previous minimax problem.

If the state space representations of $G_{sf}(s)$ is given by,

$$G_{sf}(s) = \begin{bmatrix} A_{sf} & B_{sf} \\ C_{sf} & D_{sf} \end{bmatrix} \quad (6.1-23)$$

then $G_{sf}^{-1}(s)$ has the state space representation

$$G_{sf}^{-1}(s) = \begin{bmatrix} A_{sf} - B_{sf}D_{sf}^{-1}C_{sf} & B_{sf}D_{sf}^{-1} \\ -D_{sf}^{-1}C_{sf} & D_{sf}^{-1} \end{bmatrix} \quad (6.1-24)$$

The state space representations of $\bar{P}_{11}(s)$ and $\bar{P}_{21}(s)$ are given by,

$$\bar{P}_{11}(s) = \begin{bmatrix} \bar{A} & \bar{B}_1 \\ \bar{C}_2 & \bar{D}_{11} \end{bmatrix} \quad (6.1-25)$$

and

$$\bar{P}_{21}(s) = \begin{bmatrix} \bar{A} & \bar{B}_1 \\ \bar{C}_2 & \bar{D}_{21} \end{bmatrix} \quad (6.1-26)$$

where,

$$\begin{aligned} \bar{A} &= \begin{bmatrix} A & -\left[B_1 \frac{1}{\alpha_p} B_2 \right] D_{sf}^{-1} C_{sf} \\ 0 & A_{sf} - B_{sf} D_{sf}^{-1} C_{sf} \end{bmatrix} \\ \bar{B}_1 &= \begin{bmatrix} \left[B_1 \frac{1}{\alpha_p} B_2 \right] D_{sf}^{-1} \\ B_{sf} D_{sf}^{-1} \end{bmatrix} \\ \bar{C}_1 &= \begin{bmatrix} C_2 & -\left[D_{21} \frac{1}{\alpha_p} D_{22} \right] D_{sf}^{-1} C_{sf} \end{bmatrix} \\ \bar{C}_2 &= \begin{bmatrix} C_3 & -\left[D_{31} \frac{1}{\alpha_p} D_{32} \right] D_{sf}^{-1} C_{sf} \end{bmatrix} \\ \bar{D}_{11} &= \left[D_{21} \frac{1}{\alpha_p} D_{22} \right] D_{sf}^{-1} \\ \bar{D}_{21} &= \left[D_{31} \frac{1}{\alpha_p} D_{32} \right] D_{sf}^{-1} \end{aligned} \quad (6.1-27)$$

The condition for robust performance can now be restated as,

$$\|\bar{G}(s)\|_\infty < 1 \quad (6.1-28)$$

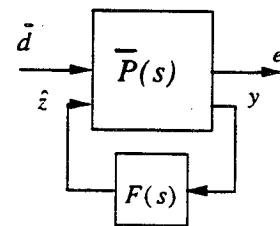


Figure 6.1-4: Modified Robust Performance Problem

$\bar{P}(s)$ is shown in Figure (6.1-4) and has the state space representation

$$\bar{P}(s) = \begin{bmatrix} \bar{A} & \bar{B}_1 & 0 \\ \bar{C}_1 & \bar{D}_{11} & -I \\ \bar{C}_2 & \bar{D}_{21} & 0 \end{bmatrix} \quad (6.1-29)$$

This representation is the same form as the previous minimax problem except for the presence of the \bar{D}_{11} term and the fact that $\bar{B}_1 \bar{D}_{21}^T$ is not zero. Next, a minimax solution is developed for this more general case.

Using the state space representation of Equation (6.1-29), the open loop dynamics of the general problem are given by,

$$\begin{aligned}\dot{x} &= \bar{A}x + \bar{B}_1 \bar{d} \\ e &= \bar{C}_1 x + \bar{D}_{11} \bar{d} - \hat{z} \\ y &= \bar{C}_2 x + \bar{D}_{21} \bar{d}\end{aligned}\tag{6.1-30}$$

The estimator has the same form as the steady state Kalman filter

$$\begin{aligned}\dot{\hat{x}} &= \bar{A}\hat{x} + K(y - \hat{y}) \\ \hat{z} &= \bar{C}_1 \hat{x} \\ \hat{y} &= \bar{C}_2 \hat{x}\end{aligned}\tag{6.1-31}$$

and has the following estimation error dynamics

$$\begin{aligned}\dot{\tilde{x}} &= (\bar{A} - K\bar{C}_2)\tilde{x} + (\bar{B}_1 - K\bar{D}_{21})\bar{d} \\ e &= \bar{C}_1 \tilde{x} + \bar{D}_{11} \bar{d}\end{aligned}\tag{6.1-32}$$

As in the minimax problem, a cost function is constructed consisting of the 2-norm of the error with terms representing the norm bounded disturbance and error dynamics added with Lagrange multipliers. The resulting minimizing gain is given by,

$$K = (\hat{P}C^T + B_1 S^{-1} D_{21}^T) V^{-1}\tag{6.1-33}$$

where

$$\begin{aligned}\hat{C} &\equiv (\bar{C}_2 + \bar{D}_{21} S^{-1} \bar{D}_{11}^T \bar{C}_1) \\ V &\equiv \bar{D}_{21} S^{-1} \bar{D}_{21}^T \\ S &\equiv (\gamma^2 I - \bar{D}_{11}^T \bar{D}_{11})\end{aligned}\tag{6.1-34}$$

and P is the symmetric positive definite solution to the Riccati equation described in the following equation

$$\begin{aligned} & \left[\bar{A} + \bar{B}_1 S^{-1} (\bar{D}_{11}^T \bar{C} - \bar{D}_{21}^T V^{-1} \hat{C}) \right] P + P \left[\bar{A} + \bar{B}_1 S^{-1} (\bar{D}_{11}^T \bar{C} - \bar{D}_{21}^T V^{-1} \hat{C}) \right]^T \\ & + \bar{B}_1 S^{-1} (S - \bar{D}_{21}^T V^{-1} \bar{D}_{21}) S^{-1} B_1^T - P \left[\hat{C}^T V^{-1} \hat{C} - \bar{C}_1^T (I + D_{11} S^{-1} \bar{D}_{11}^T) \bar{C}_1 \right] P = 0 \end{aligned} \quad (6.1-35)$$

6.2 Problem Formulation and Estimator Design

Because the robust estimator being investigated is for continuous-time, time-invariant systems at steady state, and the thrust estimation problem posed earlier is a discrete-time, time-varying formulation, a different problem must be formulated to test the robust design. This section presents a simple thrust estimation problem for one jet that is continuous and time invariant.

6.2.1 Structure

The example problem consists of the Shuttle reentry dynamics presented earlier, but with only one jet. The major difference from the earlier structure of the problem lies in the incorporation of the jet firing. Previously, when a jet was commanded ON, terms in the transition matrix mapped the jet force to the vehicle states, causing the system to be time varying. To avoid this problem, the jet command is now treated as an input. The mapping from jet force to vehicle rates and attitudes is in the input matrix. The state used for estimating jet force is no longer defined as the force of the last firing, now it is the deviation from the nominal force value.

The simplified plant dynamics are assumed to have the structure given by,

$$\begin{aligned} \dot{x} &= Ax + Bu + w \\ y &= Cx + Du + v \\ \hat{z} &= Mx \end{aligned} \quad (6.2-1)$$

where, x is the state vector, y is the measurement vector, u is the control input, \hat{z} is the quantity to be estimated, w is the process noise, and v is the measurement noise. The process and the measurement noises are the same as those described in Section 4.2.

The first six states are the attitudes and rates in the stability axis frame. The last state represents the deviation from the nominal jet thrust. The state vector is given by,

$$\mathbf{x} = \begin{bmatrix} \phi \\ \alpha \\ \beta \\ \dot{\phi} \\ \dot{\alpha} \\ \dot{\beta} \\ \Delta F \end{bmatrix} \quad (6.2-2)$$

The structure of the dynamics matrix, \mathbf{A} , is given in Equation (6.2-3). The upper left block contains the vehicle dynamics. The upper right block maps the jet force deviation to the vehicle attitudes and rates. The lower portion of the dynamics matrix is zero because the thrust deviation is assumed to be a constant state, and as such has no dynamics.

$$\mathbf{A} = \begin{bmatrix} \mathbf{A}_{\text{veh dyn}} & \Delta \omega_{\text{jet}} \\ 0 & 0 \end{bmatrix} \quad (6.2-3)$$

The inputs are the nominal jet force and the error in thrust due to system degradation in lb. The nominal jet force input is binary, 870 lb when the jet is commanded ON and 0 lb when the jet is commanded OFF. The ΔF input is used to model degraded performance. The actual jet force being modeled is the sum of the nominal and the subsystem degradation forces,

$$\mathbf{u} = \begin{bmatrix} F_{\text{nom}} \\ \Delta F \end{bmatrix} \quad (6.2-4)$$

$$F_{\text{act}} = F_{\text{nom}} + \Delta F \quad (6.2-5)$$

The measurements provided from the plant to the estimator are the angular rates and the feedthrough nominal jet force.

$$y = \begin{bmatrix} \omega \\ F_{\text{nom}} \end{bmatrix} \quad (6.2-6)$$

The quantity to be estimated, \hat{z} , is the deviation of thrust from nominal,

$$\hat{z} = \Delta F \quad (6.2-7)$$

The model described above was rearranged into the three block format for implementation of the robust estimator design procedure. Figure (6.2-1) illustrates this structure.

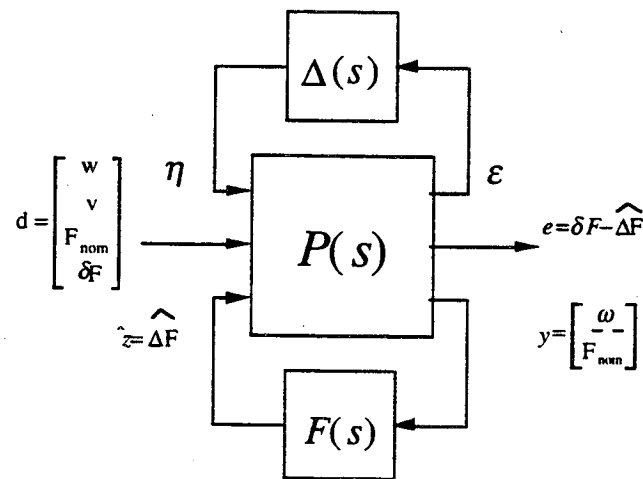


Figure 6.2-1: Inputs and Outputs of Simple RCS Model

The modeling uncertainty for the example is parametric modeling uncertainty. Specifically, the magnitude and dynamics of this uncertainty are the difference between two of the reentry vehicle models (Mach 8.8, α 35° and Mach 7.5, α 38°). This modeling uncertainty is fit to the Δ -block structure through a procedure taken from [Appleby] outlined in Appendix C.

Four design weights are varied iteratively to design the robust estimator. These parameters are: α_p , α_e , W_1 and W_2 shown in Figure (6.2-2). α_p is a weighting to scale the desired performance of the system. α_e scales the Δ block and effects the robustness of the design. In general, these two weights trade off robustness for performance. W_1 and W_2 are parameters used to weight the nominal and jet error inputs, respectively. These weights emphasize the

importance of the nominal firing relative to the other inputs. The ratio of W_1 to W_2 , reflects the relative importance placed on tracking the nominal force versus being able to track a deviation from nominal.

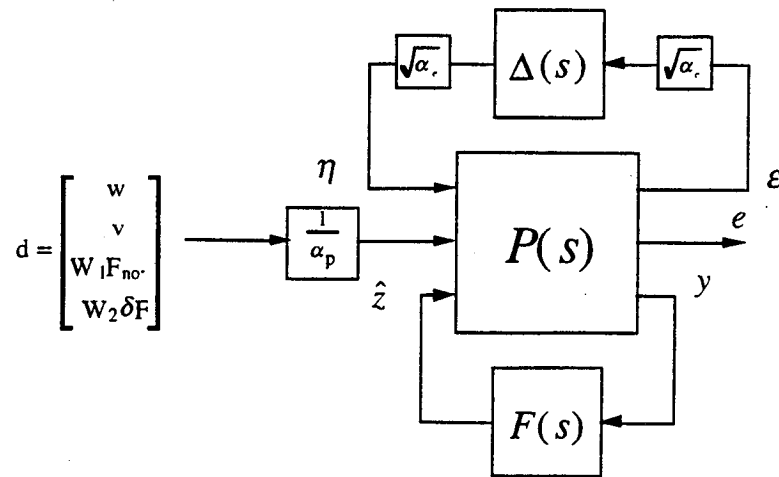


Figure 6.2-2: Weights for Robust Design

6.3 Comparison of Performance

The fundamental difference between the continuous-time Kalman filter and the generalized robust minimax estimator lies in their treatment of the plant. The Kalman filter takes a given nominal plant model and provides the optimal estimates for that particular plant model. With perturbed model parameters, the Kalman filter, designed for the nominal plant, provides estimates that are no longer optimal and may, in fact, be quite poor. Conversely, the generalized robust minimax estimator is designed for a set of plant models centered at the nominal model extending out in all directions to include the bounded perturbations implied by the Δ block. While performance for the nominal case may not match that of the Kalman filter, the performance criterion specified in the design of the filter will be met for all models implied by the nominal model and the given bounded parameter perturbations. It is for these off-nominal cases that the robust estimator is expected to outperform the Kalman filter.

Two frequency responses and one time simulation were used to evaluate the robust minimax estimator and the Kalman filter. The frequency responses are maximum singular value plots and consist of the response from the input thrust error, δF , to the estimated thrust error, $\hat{\Delta}F$, and the response from δF to the

estimation error, e . The first plot, Figure (6.3-2), from δF to $\hat{\Delta F}$ is the closed loop frequency response, illustrating the high frequency performance of the designs. The other frequency response, Figure (6.3-3), from δF to e is the sensitivity of the estimation error to an error in jet thrust. It highlights the low frequency, steady-state performance of the filter. The time simulation consists of a 5 second jet firing which has a 300 lb error from nominal. This simulation, Figure (6.3-4), illustrates the time responses of the different designs, and the effect of modeling uncertainty on estimator performance.

To compare the robust minimax estimator and the Kalman filter designs, the estimators are designed for the nominal flight condition with the bounded uncertainty including the modeling uncertainty perturbation. The designed filter is then implemented with both the nominal and perturbed models (Mach 7.5 α 35 and Mach 8.8 α 38 respectively). The difference between the nominal and perturbed models is a shift in the resonant frequency and a slight shift in gain. These differences are illustrated in Figure (6.3-1). The shift in gain is caused by the different angle of attack changing the mapping from jet force to the stability axis frame. For example, at zero angle of attack, a side firing jet has a pure sideslip effect. However, at a non zero angle of attack, a side firing jet has both a sideslip and a roll component.

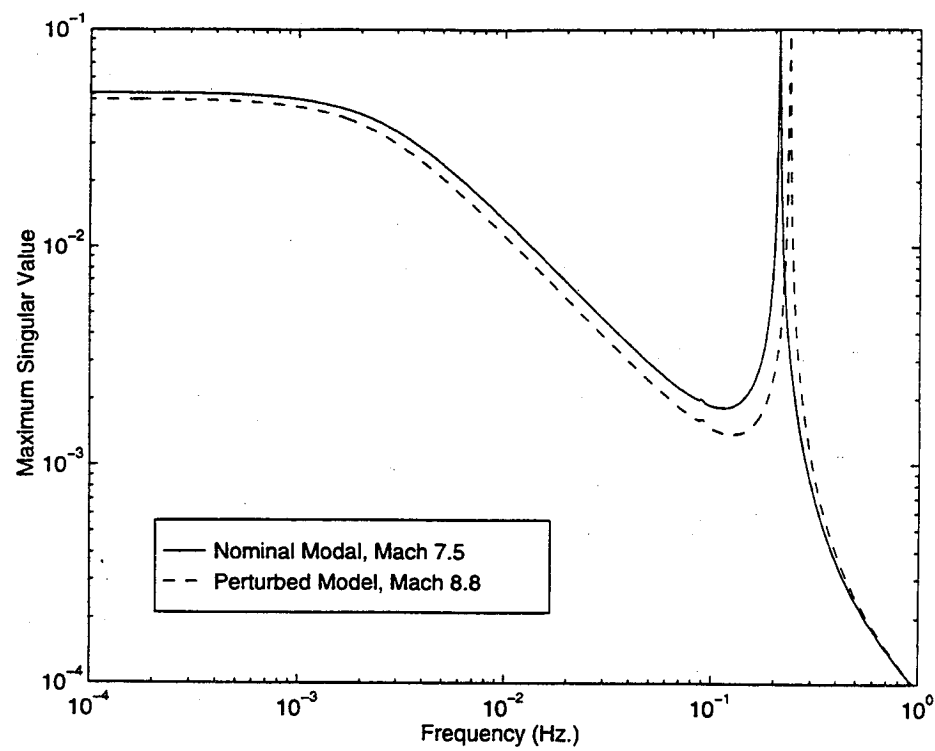


Figure 6.3-1: Singular Values of Nominal and Perturbed Models from Jet Force to Rates

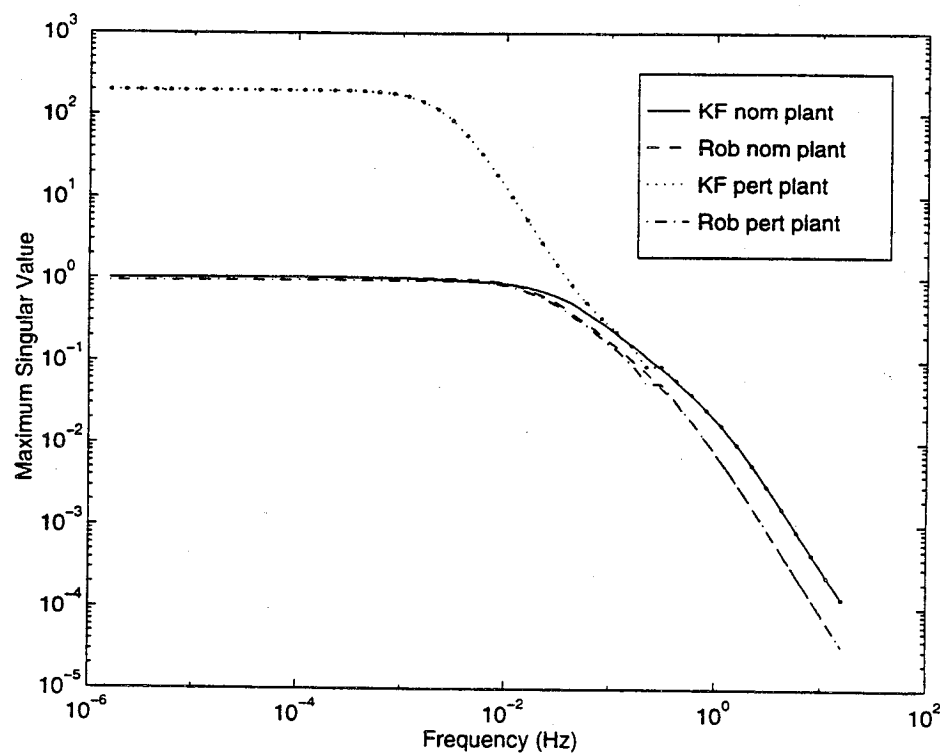


Figure 6.3-2: Frequency Responses from δF to \hat{A}^F

Figure (6.3-2) shows the “closed loop” response of the different designs. Notice that the robust estimator has only a slightly lower bandwidth than the Kalman filter. This plot shows the Kalman filter’s poor performance when used on a perturbed plant model.

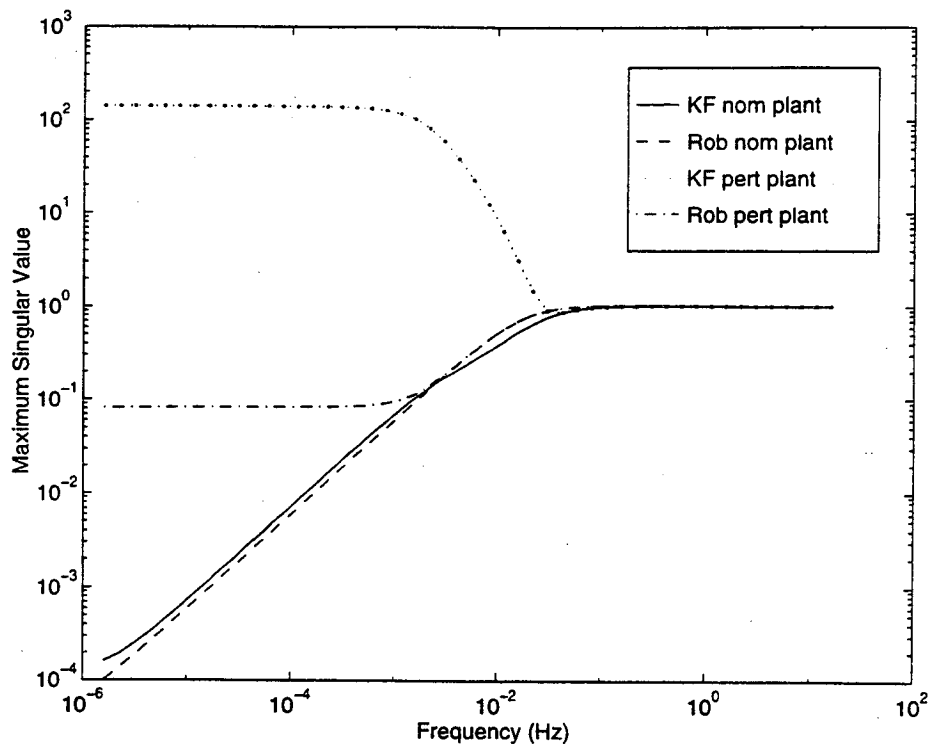


Figure 6.3-3: Frequency Responses from ΔF to e

Figure (6.3-3) shows the “sensitivity” plot of the different estimators. For the robust design, the estimation error in steady state is slightly less than 1/10 the total thrust, whereas for the Kalman filter the error is more than 100 times the thrust level. Notice that there is significant error at low frequency. This error is a result of the different angles of attack of the different models. The different angles of attack cause a difference in jet mapping to the stability coordinate frame.

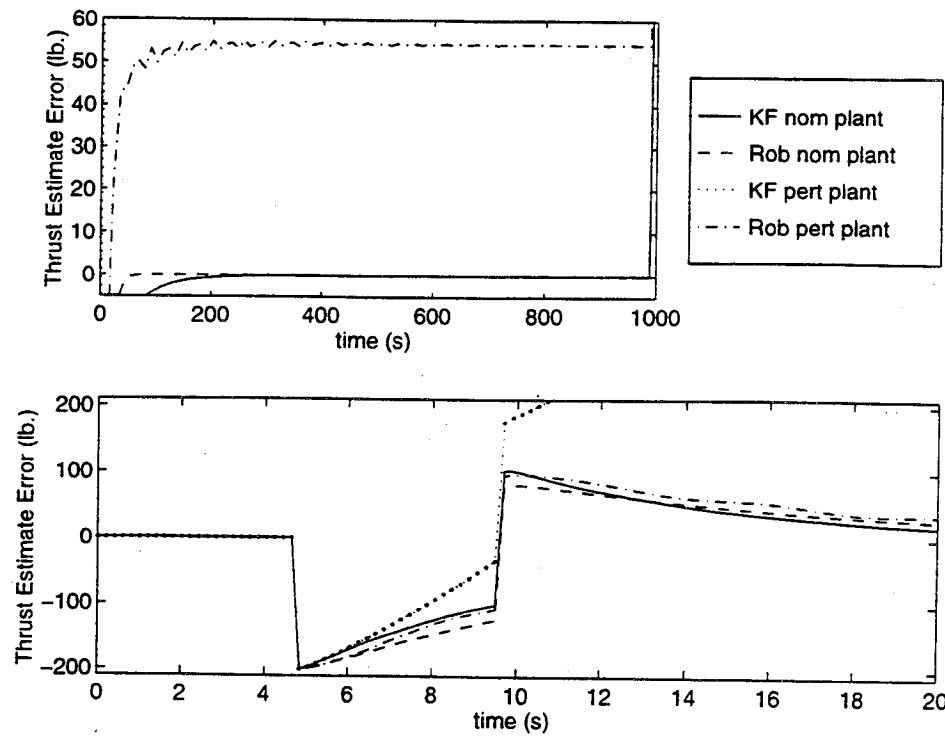


Figure 6.3-4: Time Responses of Estimation Error

The top subplot in Figure (6.3-4) shows the steady state error of the estimators. This plot shows the response to a single jet step firing command attenuated by 300 lb (the jet turns on at $t=5s$, and remains on throughout simulation). The bottom subplot in Figure (6.3-4) shows the time response to a five second jet firing attenuated by 300 lb. Notice how the Kalman filter's estimation error quickly goes off the scale. The steady state error for the Kalman filter is not divergent but is large, on the order of 10^5 .

7.0 Conclusion

Three main results can be derived from the application of VHM technology to the Space Shuttle RCS investigated in the previous chapters. First, a general framework has been developed for application of VHM to a general propulsive GN&C system. Second, in the design of this system, there are three factors that largely effect the ability of the monitoring algorithm to accurately characterize system performance (estimate jet thrust); time delays, modeling error, and jet plume interaction with the aerodynamic flowfield. Finally, Robust estimators were shown to provide one possible method of reducing the required modeling accuracy.

A general VHM system is envisioned as a two tier hierarchy that is able to categorize system performance as nominal or degraded. If performance is off-nominal, VHM system will quantify the amount of the degradation, identify its cause and assign a confidence factor to its assessment. As an example, a top level VHM monitor was designed and analyzed for the Space Shuttle Orbiter RCS. Specifically, the reentry flight phase was examined because it not only has large uncertainties associated with the aerodynamics but also encompasses the problems present in other phases of flight.

If the monitoring algorithm ignores actuator dynamics, the jet thrust estimate degrades. The primary cause of this degradation is the delay introduced by the dynamics. To correct the problem, an appropriate delay was introduced in the feedforward of effector commands to the filtering algorithm. To actually implement a VHM system, all delays that occur between effector commands and a measurable dynamic response, must be quantified. Appropriate delays in the feedforward of these commands can then be incorporated into the algorithm design.

Parametric error in the model representing the rigid body reentry dynamics introduced large errors in the Kalman filter. The errors modeled were uncertainty in Mach number and angle of attack. A possible method for reducing the sensitivity to this modeling error is the implementation of a robust estimator in the monitoring algorithm. A robust estimator was shown to be

significantly less sensitive to the parametric modeling uncertainty because it incorporates the model perturbation into the filter design.

Jet plume interaction uncertainty also presents a challenge to accurate thrust estimation. This effect arises when the jet plume alters the pressure field surrounding the vehicle, causing moments and forces that are not present in a vacuum. A model exists for predicting this effect, but is not accurate enough to guarantee good estimates of jet thrust. To precisely estimate jet thrust during reentry, a better method of predicting the jet plume interaction effect is required.

7.1 Summary of Results

Chapter 2 presented the Space Shuttle RCS and aerosurfaces. The following RCS components and characteristics were described: propellant feed system, thruster design, redundancy management, available sensors and typical failures. The Shuttle has five aerosurfaces, a pair of elevons, rudder, speedbrake, and bodyflap. The speedbrake and bodyflap are not used for active attitude control, but are used for maintaining vehicle trim.

Chapter 3 described Space Shuttle reentry and relevant models used in the simulation of reentry. After introducing the reentry sequence of events, the models of the entry simulation and flight controller were given. Next, a linear model of the reentry dynamics dependent primarily on angle of attack and Mach number presented originally in [Zacharias] was developed. Also in Chapter 3 are models for the representation of the aerosurface deflections and associated torques, the torques produced by the jets, and sensor modeling used in the thesis. Lastly, two example maneuvers are presented, generated from the developed flight controller and vehicle model.

Chapter 4 introduces general VHM design issues and presents a Kalman filter based estimator to be used as the top level of a VHM system. The assumed form of the vehicle model is given followed by a derivation of the discrete Kalman filter. An implementation of the Kalman filter for estimating the most recent jet thrust from each jets is presented.

Chapter 5 analyzed the filter designed in Chapter 4. A discrete time interval was chosen that will allow the estimation of thrust for a minimum on-time firing to within 10 percent. This Δt is 0.01 seconds for the onboard Shuttle IMU as a sensor. Estimation error covariance time histories were given for

different rate sensors, different firing lengths, and different discrete time steps. Open loop simulations of multiple jets firing from the same pod illustrate basic filter performance. Closed loop simulations making use of the flight control model with example maneuvers were used to investigate the effects of unmodeled factors on the ability to estimate jet thrust. Specifically, the effects of neglected aerosurface dynamics, neglected thrust dynamics, parametric aerodynamic uncertainties, and plume interaction with the aerodynamic flow field were investigated. The Kalman filter was shown to be sensitive to time delays, the aerodynamic modeling uncertainties, and plume interaction uncertainty.

In Chapter 6, an investigation was made into the applicability of robust filters for the VHM estimation problem. An overview was given of the minimax and the generalized minimax estimator. A robust minimax estimator was shown to be significantly less sensitive than the Kalman filter to parametric plant modeling uncertainty.

7.2 Recommendations for Future Work

After this initial look into VHM and its application to the Space Shuttle RCS, several new questions have been raised and new directions for work have become apparent.

Specifically, the plume interaction with the aerodynamic flow field presents a problem in estimating thrust. A method to separate the forces and moments produced by the effectors and the plume interaction with the aerodynamic flowfield is required. Future work should focus on robust estimation of thrust in the presence of plume flowfield interaction modeling errors. This task is made challenging because of the difficulty in distinguishing these errors from actual RCS thruster system errors.

Chapter 5 showed that Kalman filter based estimation relies on an accurate model to produce a quality thrust estimate. In Chapter 6, a robust estimator was shown to have promise as a VHM top level estimator that would alleviate some of the strict modeling requirements of the Kalman filter. However, the example problem was continuous-time, time-invariant, and contained only a single jet with its associated gains as if the jet was firing all the time. Discrete-time, finite horizon, time-varying estimators have been recently

derived by Mangoubi that are robust to modeling and plant uncertainty. The application of this estimation theory should be investigated since a time-varying discrete filter should provide better results than the Kalman filter and the linear continuous-time robust estimators.

More work is also required to develop local monitors for isolation. The design of the exact algorithm implemented for a local monitor will probably be highly system dependent. However, there are several general issues that need to be addressed in the area of data fusion and priority of information.

To verify the results of this thesis, downlisted flight data from the Shuttle or any aerospace vehicle could be obtained and the filtering performed off-line. Shuttle flights that have experienced jet problems would be preferable for this type of investigation. By filtering data from a flight with a known failure, it may be possible to show that information in the vehicle's dynamic response can identify the off-nominal jet performance.

An on-board flight experiment of a VHM system would be desirable. The onboard testing of the top level algorithm would not be difficult. All the required sensor information is present in the flight software. However, since the cycle time is, at the fastest, 12.5 Hz the algorithm would need to be implemented with a time step slower than 0.01 s or direct access to the sensors in the Shuttle would be needed to allow for measurements at a higher rate. Another possibility to get measurements at a higher data rate would be to put a self contained black box monitoring system in a Shuttle Get-Away-Special container (GAS can). The GAS can could include rate gyros to record the angular rates and mission time at a higher data rate than currently possible. The recorded rate data could then be matched with recorded effector command data and examined post-flight. In addition, all of the time delays effecting the RCS, aerosurfaces, and sensors would have to be incorporated into the design of the monitoring system.

Implementation in the current flight software for execution on the Shuttle's General Purpose Computers (GPC) would be difficult. The GPCs have neither the extra memory nor processing power required to execute the time-varying Kalman filter loop running at 100 Hz. However, new systems may have faster, more able computers and easier access to the required sensor information, allowing a greater chance for implementation of such monitoring algorithms.

Implementation of a local VHM monitor on the Shuttle would be a more arduous task because of the large amount of sensor information that would have to be accessed.

Appendix A: Relationship of Jet Thrust to Angular Acceleration

To estimate the force produced by each jet firing, the relationship between jet force and angular acceleration is incorporated into the filter. This relationship is desired since jet force is the quantity of interest and the inputs to the model are angular accelerations.

Given, torque and angular acceleration vectors, each with components in the body axis frame,

$$\dot{\omega} = \begin{bmatrix} u_x \\ u_y \\ u_z \end{bmatrix} \quad \tau = \begin{bmatrix} \tau_x \\ \tau_y \\ \tau_z \end{bmatrix} \quad (A-1)$$

They are related through the inertia tensor by the relation,

$$\tau = I\dot{\omega} \quad (A-2)$$

Rearranging,

$$\dot{\omega} = I^{-1}|\tau|\hat{\tau} \quad (A-3)$$

where, $|\tau|$ is the magnitude of the torque vector and $\hat{\tau}$ is the direction of the torque unit vector.

The torque magnitude can be expressed as the magnitude of the cross product of the position and force vectors. The position vector is from the center of gravity to the jet location. The force vector simply contains the force produced by a jet in each of the body axis directions.

$$\dot{\omega} = I^{-1}|r \times F|\hat{\tau} \quad (A-4)$$

The cross product can then be decomposed into the product of the magnitude of the force vector and the perpendicular distance to the jet. This perpendicular distance is the difference between the position vector and its projection on the force vector. Figure (A-1) shows the geometric relationship of these vectors.

$$\dot{\omega} = I^{-1} |F| \left| r - \frac{ff^T}{f^T f} r \right| \hat{\tau} \quad (A-5)$$

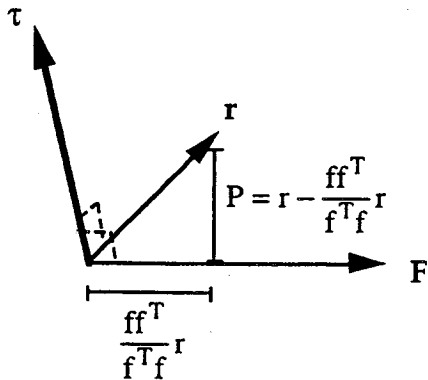


Figure A-1: Geometric Relation of Vectors

Combining I^{-1} , the perpendicular vector, P , and the torque unit vector yields a vector multiplier, K , that transforms jet thrust into the resulting angular acceleration placed on the body.

$$\dot{\omega}_{\text{jet}} = K_{\text{jet}} |F| \quad (A-6)$$

This K was computed for every jet independent of force. Now given a jet force magnitude, the resulting angular accelerations produced in each axis may be computed.

Appendix B: Reentry Model Parameters

Model #	1	2	3	4	5	6	7	8
h (ft.)	77000	90000	105000	120000	130000	150000	158000	170000
Mach	2	3	4	5	5.7	7.5	8.8	10
V_T (ft/s)	1950	3000	4000	5100	5900	8300	9500	10900
α (deg.)	12.5	16	20.5	25	29	35	38	40
q (lb/ft ²)	200	215	200	177	150	125	118	110
ϕ_j / ϕ_∞	7.72e-4	7.18e-4	7.72e-4	8.72e-4	1.03e-3	1.23e-3	1.31e-3	1.47e-3
$C_{M\delta_e}$	-0.17	-0.1	-0.11	-0.12	-0.135	-0.16	-0.22	-0.27
$C_{M\alpha}$	-0.16	-0.05	-0.05	-0.075	-0.1	-0.14	-0.15	-0.175
C_D	0.23	0.22	0.3	0.35	0.48	0.65	0.8	0.84
$C_{L\alpha}$	1.8	1.6	1.63	1.6	1.6	1.4	1.0	1.19
C_{Mq}	-1.1	-0.9	-1.1	-1.1	-1.2	-1.3	-1.5	-1.6
C_L	0.4	0.38	0.5	0.57	0.7	0.8	0.87	0.86
$C_{D\delta_e}$	0.04	0.04	0.045	0.064	0.08	0.11	0.14	0.146
$C_{L\delta_e}$	0.2	0.16	0.135	0.12	0.13	0.15	0.15	0.17
$C_{n\beta}$	0.2	0.1	0.17	0.18	0.28	0.4	0.53	0.59
$C_{y\beta}$	-1	-0.77	-0.6	-0.65	-0.65	-0.5	-0.5	-0.35
$C_{l\beta}$	-0.4	-0.06	-0.37	-0.38	-0.4	-0.55	-0.62	-0.61
$C_{l\phi}$	0.15	0.11	0.11	0.15	0.2	0.3	0.36	0.37
$C_{n\delta_r}$	-0.07	-0.05	-0.037	-0.013	-0.005	-0.005	-0.00005	0
$C_{n\delta\alpha}$	-0.07	0.09	-0.1	-0.15	-0.17	-0.2	-0.28	-0.35
$C_{l\beta}$	-0.08	-0.06	-0.06	-0.08	-0.094	-0.105	-0.115	-0.12
$C_{L\delta\alpha}$	0.05	0.035	0.035	0.037	0.04	0.04	0.04	0.05
$C_{l\delta_r}$	0.02	0.015	0.009	0.005	0.0002	0.0009	0	0
$C_{2\phi}$	-0.09	-0.07	-0.058	-0.06	-0.067	-0.07	-0.072	-0.073

Vehicle Constants

m (slugs)	I_{xx} (sl-ft ²)	I_{yy} (sl-ft ²)	I_{zz} (sl-ft ²)	I_{xz} (sl-ft ²)	S (ft ²)	c (ft)	b (ft)
5640	0.805e6	5.85e6	6.07e6	0.14e6	2690	39.6	78.06

Appendix C: Incorporating Parametric Uncertainty
and
Spectral Factorization

C.1 Incorporating Parametric Uncertainty into the Δ -block

The following method is a way of incorporating parametric uncertainty into the delta block of a three block diagram [Appleby]. The nominal and perturbed vehicle dynamics were differenced to obtain the error dynamics.

$$\begin{aligned}\Delta \dot{x} &= (A_{nom} - A_{pert})x + (B_{nom} - B_{pert})u \\ \Delta y &= (C_{nom} - C_{pert})x + (D_{nom} - D_{pert})u\end{aligned}\quad (C-1)$$

$$\begin{aligned}\Delta \dot{x} &= \Delta Ax + \Delta Bu \\ \Delta y &= \Delta Cx + \Delta Du\end{aligned}\quad (C-2)$$

The uncertainties from all of the state space matrices can be combined into one matrix, N ,

$$N = \begin{bmatrix} \Delta A & \Delta B \\ \Delta C & \Delta D \end{bmatrix} \quad (C-3)$$

Because the resulting perturbation matrix, N , is often sparse, it may be factored into a more convenient format.

$$N = \begin{bmatrix} Q \\ R \end{bmatrix} [S \quad T] \quad (C-4)$$

The plant may now be described in a matrix shorthand format,

$$\begin{bmatrix} \dot{x}_{nom} \\ \varepsilon \\ e \\ y \end{bmatrix} = \begin{bmatrix} A_{nom} & Q & B_{nom} & 0 \\ S & 0 & T & 0 \\ M & 0 & 0 & -I \\ C_{nom} & R & D_{nom} & 0 \end{bmatrix} \begin{bmatrix} x_{nom} \\ \eta \\ d \\ \hat{z} \end{bmatrix} \quad (C-5)$$

C.2 Spectral Factorization

Given a stable transfer function

$$G(s) = \begin{bmatrix} A & B \\ C & D \end{bmatrix} \quad (C-6)$$

with the norm bound

$$\|G(s)\|_\infty < \gamma \quad (C-7)$$

then there exists a spectral factor, $G_{sf}(s)$, such that

$$G_{sf}^-(s)G_{sf}(s) = \gamma^2 I - G^-(s)G(s) \quad (C-8)$$

One such $G_{sf}(s)$ is given by

$$G_{sf}(s) = \begin{bmatrix} A \\ -S^{-\frac{1}{2}}(B^T X + D^T C) \end{bmatrix} \left| \begin{bmatrix} B \\ S^{\frac{1}{2}} \end{bmatrix} \right. \quad (C-9)$$

where

$$\overset{\Delta}{S} = \gamma^2 I - I - D^T D \quad (C-10)$$

and X is the symmetric positive definite solution to the algebraic Riccati equation

$$(A + BS^{-1}D^T C)^T X + X(A + BS^{-1}D^T C) + XBS^{-1}B^T X + C^T(I + DS^{-1}D^T)C = 0$$

$$(C-11)$$

that places the eigenvalues of $(A + BS^{-1}D^T C + BS^{-1}B^T X)$ in the left half plane.

References

[Anomaly] *Shuttle Flight Data and In-Flight Anomaly List*, Revision T, PCN-1, NASA Document JSC-19413, August 1994.

[Appleby] Appleby, B., *Robust Estimator Design using the H_∞ Norm and μ Synthesis*, Ph.D. Thesis, Department of Aeronautics and Astronautics, MIT, 1990.

[Athans] Athans, M., "Multivariable Control Systems I & II," course lecture notes, MIT, 1993-94.

[Brown] Brown, R. and Hwang, P., *Introduction to Random Signals and Applied Kalman Filtering*, 2nd edition, John Wiley & Sons, Inc., New York, 1992.

[Doyle 86] Doyle, J., Lenz, K., and Packard, A., "Design Examples using μ -synthesis: Space Shuttle Lateral Axis FCS During Reentry," *Proceedings of the 25th Conference on Decision and Control*, pp. 2218-2223, December 1986.

[Doyle 87] Doyle, J., Glover, K., Khargonekar, P., and Francis, B., "State-Space Solutions to the H_2 and H_∞ Control Problems," *IEEE Transactions on Automatic Control*, Vol. 34, No. 8, pp. 242-250, 1987.

[FAD-26] *FAD-26*, on-orbit Space Shuttle plume impingement investigation, NASA Document JSC-22078, April 1986.

[FSSR-RM] *Space Shuttle Orbiter Operational Level C Functional Subsystem Software Requirements; Redundancy Management*, Rockwell International Document STS83-0010H, OI-25, June 10, 1994.

[FSSR-GNC] *Space Shuttle Orbiter Operational Level C Functional Subsystem Software Requirements; Guidance, Navigation and Control*, Rockwell International Document STS83-0007H, OI-25, June 7 1994.

[Gelb] Gelb, A., editor, *Applied Optimal Estimation*, The M.I.T. Press, Cambridge, Massachusetts, 1974.

[Hattis] Hattis, P., "A Review of the Space Shuttle Orbital Flight Control System," C. S. Draper Laboratory Publication CSDL-P-1786, October 1983.

[Hearn] Hearn, H. C., "Evaluation of Bipropellant Pressurization Concepts for Spacecraft," *Journal of Spacecraft and Rocketry*, Vol. 19, No. 4, July-August 1982.

[I-Load] *Space Shuttle Flight Software Initialization Load, STS-65 Flight Cycle, Flight Specific Requirements*, Vol. II, NASA Document JCS-19350, March 1994.

[Kalman] Kalman, R. E., "A New Approach to Linear Filtering and Prediction Problems," *Transaction of the ASME Journal of Basic Engineering*, Vol. 82D, pp. 35-45, March 1960.

[Khargonekar] Khargonekar, P. P. and Nagpal K. M., "Filtering and Smoothing in an H_{∞} Setting," *Proceedings of the IEEE Conference on Decision and Control*, pp. 415-420, December 1989.

[Mangoubi] Mangoubi, R., Robust Estimation and Failure Detection for Linear Systems, Ph.D. Thesis, Department of Aeronautics and Astronautics, MIT, January 1995.

[OADB] *Operational Aerodynamic Data Book*, Vol. 1-3, Rockwell International Document STS85-0118, September 1985.

[Paradiso] Paradiso, J. A., *Application of Linear Programming to Coordinated Management of Jets and Aerosurfaces for Aerospace Vehicle Control*, C. S. Draper Laboratory Report CSDL-R-2065, November 1988.

[Rules] *Space Shuttle Operational Flight Rules Annex, Flight STS-60*, Final, PCN-1, NASA Document NSTS-18308, January 10, 1994.

[Saxton] Saxton, H. A. and Cox, G. R., "The Space Transportation System Reaction Control System," Rockwell International, Downey, California.

[SODB] *Shuttle Operations Data Book*, Volume I, NASA Document NSTS-08934, January 1988.

[Spacelink] NASA Spacelink, online database, internet address: spacelink.msfc.nasa.gov.

[Wiener] Wiener, N., *Extrapolation, Interpolation, and Smoothing of Stationary Time Series, with Engineering Applications*, Technology Press and Wiley, 1949.

[Yaesh] Yaesh, I. and Shaked, U., "Game Theory Approach to Optimal Linear Estimation in the Minimum H_{∞} -norm Sense," *Proceedings of the IEEE Conference on Decision and Control*, pp. 421-425, December 1989.

[Zacharias] Zacharias, G. L., *A Digital Autopilot for the Space Shuttle Vehicle*, S.M. Thesis, Department of Aeronautics and Astronautics, MIT, February 1974.

